# REPORT DOCUMENTATION PAGE

Form Approved
OMB No. 0704-0188

The public reporting burden for this collection of information is estimated to average 1 hour per response, including the time for reviewing instructions, searching existing data sources, gathering and maintaining the data needed, and completing and reviewing the collection of information. Send comments regarding this burden estimate or any other aspect of this collection of information, including suggestions for reducing the burden, to the Department of Defense, Executive Service Directorate (0704-0188). Respondents should be aware that notwithstanding any other provision of law, no person shall be subject to any penalty for failing to comply with a collection of information if it does not display a currently valid OMB control number.

PLEASE DO NOT RETURN YOUR FORM TO THE ABOVE ORGANIZATION.

1. REPORT DATE *(DD-MM-YYYY)*	2. REPORT TYPE	3. DATES COVERED *(From - To)*
06-01-12	Final Report	May 2005 - May 2011

4. TITLE AND SUBTITLE
(MURI05) - MICROVASCULAR AUTONOMIC COMPOSITES (μVAC)

5a. CONTRACT NUMBER
FA9550-05-1-0346

5b. GRANT NUMBER

5c. PROGRAM ELEMENT NUMBER

6. AUTHOR(S)
Scott R. White (PI)

5d. PROJECT NUMBER

5e. TASK NUMBER

5f. WORK UNIT NUMBER

7. PERFORMING ORGANIZATION NAME(S) AND ADDRESS(ES)
University of Illinois at Urbana-Champaign
c/o Office of Sponsored Programs and Research Administration
1901 S. First Street, Suite A
Champaign, Illinois 61820-7406

8. PERFORMING ORGANIZATION REPORT NUMBER

9. SPONSORING/MONITORING AGENCY NAME(S) AND ADDRESS(ES)
AF Office of Scientific Research
875 N Randolph St, Room 3112
Arlington, VA 22203

10. SPONSOR/MONITOR'S ACRONYM(S)
AFOSR

11. SPONSOR/MONITOR'S REPORT
NAFRL-OSR-VA-TR-2013-1026

12. DISTRIBUTION/AVAILABILITY STATEMENT

Distribution A: Approved for public release

13. SUPPLEMENTARY NOTES

14. ABSTRACT
The Microvascular Autonomic Composites (μVAC) MURI Program was supported by the Air Force Office of Scientific Research (AFOSR) through a Multidisciplinary University Research Inititative (MURI) from 2005-2011. The program was led by the University of Illinois at Urbana-Champaign (UIUC) together with partner researchers at Duke University and the University of California, Los Angeles (UCLA) during the initial three years of the program. μVAC was conceived in response to a new paradigm in materials design, that of autonomy – the ability to achieve adaptation and response in an independent and automatic fashion. The central vision of μVAC was the synthetic reproduction of autonomic biological functions, obtained through the creation and integration of complex materials systems with three-dimensional microvascular network architectures. The μVAC program utilized biomimetic and bio-inspired designs and brought together the acknowledged leaders of this field of research coupled with the foremost scientists and engineers in autonomic materials.

15. SUBJECT TERMS
microvascular, self-healing, autonomic, composites, self-cooling

16. SECURITY CLASSIFICATION OF:			17. LIMITATION OF ABSTRACT	18. NUMBER OF PAGES	19a. NAME OF RESPONSIBLE PERSON
a. REPORT	b. ABSTRACT	c. THIS PAGE			
					19b. TELEPHONE NUMBER *(Include area code)*

Standard Form 298 (Rev. 8/98)
Prescribed by ANSI Std. Z39.18
Adobe Professional 7.0

FINAL REPORT

MICROVASCULAR AUTONOMIC COMPOSITES
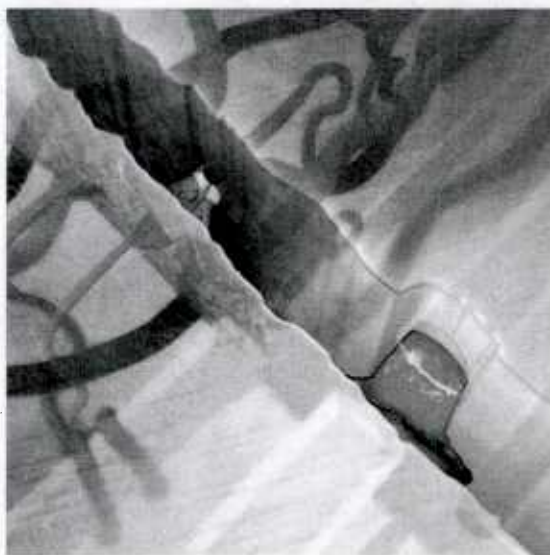
AFOSR GRANT # FA9550-05-1-0346

Scott R. White (PI)

swhite@uiuc.edu

University of Illinois at Urbana-Champaign
306 Talbot Lab, 104 S. Wright St.
Urbana, IL 61801

co-PIs: Nancy R. Sottos, Jeffrey S. Moore, Jennifer A. Lewis, Philippe H. Geubelle,
Jonathan S. Freund, Kenneth T. Christensen

Materials Sci. & Eng., Chemistry, Aerospace Eng., Mechanical Sci. & Eng.
University of Illinois at Urbana-Champaign

TABLE OF CONTENTS

2.4 Theme IV: Experimental Assessment & Analysis

3. References　　pg. 77

1. Overview

The Microvascular Autonomic Composites (μVAC) MURI Program was supported by the Air Force Office of Scientific Research (AFOSR) through a Multidisciplinary University Research Inititative (MURI) from 2005-2011. The program was led by the University of Illinois at Urbana-Champaign (UIUC) together with partner researchers at Duke University and the University of California, Los Angeles (UCLA) during the initial three years of the program. μVAC was conceived in response to a new paradigm in materials design, that of *autonomy* -- the ability to achieve adaptation and response in an independent and automatic fashion. The central vision of μVAC was the synthetic reproduction of autonomic biological functions, obtained through the creation and integration of complex materials systems with three-dimensional microvascular network architectures. The μVAC program utilized biomimetic and bio-inspired designs and brought together the acknowledged leaders of this field of research coupled with the foremost scientists and engineers in autonomic materials.

Microvascular Autonomic Composites (μVAC) Program.

The core activities of μVAC were arranged into four main research themes. In *Natural Models* biological models of vascular nnetworks were studied in order to examine their defining characteristics in meeting autonomic functionality. Inspired by these biological systems, within *Engineering Design* optimal vascular networks were designed to seamlessly integrate autonomic self-generating and self-regulating function for multifunctional load-bearing composite systems. Within *Synthetic Reproduction* these designs were synthetically reproduced by developing functional material components (e.g. healing agents) and fabrication methods to achieve high resolution vascular complexity in a cost-effective structural composite. In *Functional Testing* a full compliment of experimental and analytical techniques were utilized to demonstrate material functionality, efficiency, and environmental stability. As a result of these activities the μVAC program produced self-healing and self-cooling structural composites that respond in an autonomic fashion.
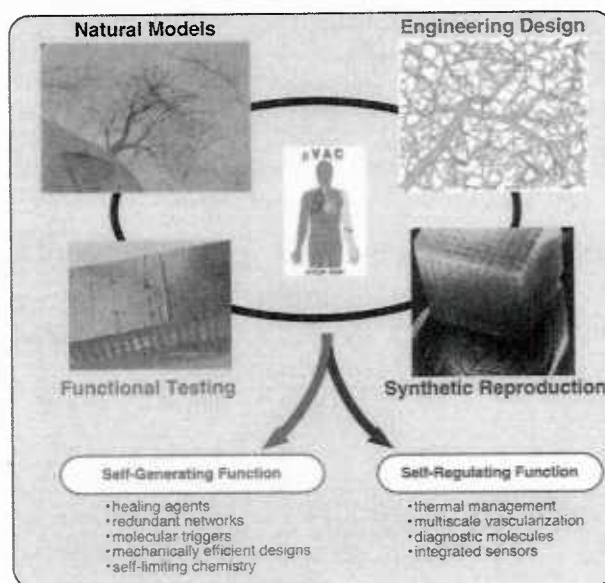
After the first three years of the MURI program the objectives were refocused on structural behavior of microvascular composites, autonomic cooling functionality, and self-healing via delivery of chemically reactive healing agents. The research activities thereafter were centered within the UIUC research team. A detailed description of thematic research results for the UIUC research team as part of the MURI program are presented in the following sections.

1.1 Archival publications resulting from the μVAC MURI program

1.　Nield DA and Bejan A, Convection in Porous Media, 3rd ed., Springer, New York, (2006).

2. Lewis JA, Direct ink writing of 3D functional materials. Advanced Functional Materials, 16(17): 2193-2204 (2006).

3. Jones AS, Rule JD, Moore JS, White SR, Sottos NR. Catalyst morphology and dissolution kinetics of self-healing polymers. Chemistry of Materials, 18(5): 1312-1317 (2006).

4. Berfield TA, Patel A, Shimmin RG, Braun PV, Lambros J, Sottos NR. Fluorescent image correlation for nanoscale deformation measurements. Small, 2(5): 631-635 (2006).

5. Caruso MM, Delafuente DA, Ho V, Moore JS, Sottos NR, White SR. Solvent-promoted self-healing materials. Macromolecules, 40:8830-8832 (2007).

6. Toohey KS, Sottos NR, Lewis JA, Moore JS, White SR. Self-healing materials with microvascular networks. Nature Materials. 6:581-585 (2007).

7. Sottos NR, White SR, Bond IP. Introduction: Self-healing polymers and composites. Journal of the Royal Society: Interface, 4:347-348 (2007).

8. Mauldin TC, Rule JD, Sottos NR, White SR, Moore JS. Self-healing kinetics and the stereoisomers of dicyclopentadiene. Journal of the Royal Society: Interface, 4: 389-393 (2007).

9. Therriault D, Lewis JA, White SR, Rheological behavior of fugitive organic inks for direct-write assembly. Applied Rheology, 17:10112 (1-8) (2007).

10. Aragon AM, Wayer JK, Geubelle PH, Goldberg DE, White SR, Design of microvascular flow networks using multi-objective genetic algorithms. Computational Methods in Engineering, 197:4399-4410 (2008).

11. Park JS, Takahashi K, Guo Z, Wang Y, Bolanos E, Hamann-Schaffner C, Murphy E, Wudl F, Hahn HT, A self-healing composite using a thermally mendable polymer. Journal of Composite Materials, 42(26): 2869-2881 (2008).

12. Lewis JA, Novel Inks for Direct-Write Assembly of 3D Periodic Structures. Materials Matters, Sigma-Aldrich, 3.1(4) (2008).

13. Youngblood J and Sottos NR. Bioinspired materials for self-cleaning and self healing. MRS Bulletin, 33:732-741 (2008). [Cover Feature]

14. Caruso MM, Blaiszik BJ, White SR, Sottos NR, Moore JS, Full recovery of fracture toughness using a non-toxic solvent-based self-healing system. Advanced Functional Materials, 18: 1898-1904 (2008). [Cover Feature]

15. Kamphaus JM, Rule JD, Moore JS, Sottos NR, White SR. A new self-healing epoxy with tungsten (VI) chloride catalyst. Journal of the Royal Society: Interface, 5: 95-103 (2008). [Cover Feature]

16. Wilson GO, Moore JS, White SR, Sottos NR, Andersson HM. Autonomic healing of epoxy vinyl esters via ring opening metathesis polymerization. Advanced Functional Materials, 18: 44-52 (2008).

17. Blaiszik B, White SR, Sottos NR. Nanocapsules for self-healing materials. Composite Science and Technology, 68:978-986 (2008).

18. Mookhoek SD, Blaiszik BJ, Fischer HR, Sottos NR, White SR, van der Zwaag S. Peripherally decorated binary microcapsules containing two liquids. Journal of Materials Chemistry, 18:5390-5394 (2008).

19. Wilson GO, Caruso MM, Reimer NT, White SR, Sottos NR, Moore JS. Survey of ruthenium metathesis catalysts for ring opening metathesis polymerization-based self-healing applications. Chemistry of Materials, 20:3288-3297 (2008).

20. Kirby E, Rule JD, Michaud VJ, Sottos NR, White SR, Manson JAE. Embedded shape memory alloy wires to enhance performance of self-healing polymers. Advanced Functional Materials, 18:2253-2260 (2008).

21.   Wilson GO, Moore JS, White SR, Sottos NR, Andersson HM. Autonomic healing of epoxy vinyl esters via ring opening metathesis polymerization. Advanced Functional Materials, 18:44-52 (2008).

22.   White SR, Caruso MM, Moore JS. Autonomic healing of polymers. MRS Bulletin, 33:766-769 (2008).

23.   Kirby EL, Michaud VJ, Manson JAE, Sottos NR, White SR. Performance of self-healing epoxy with microencapsulated healing agent and shape memory alloy wires. Polymer, 50: 5533-5538 (2009).

24.   Blaiszik B, Caruso M, McIlroy D, Moore J, White S, Sottos N. Microcapsules filled with reactive solutions for self-healing materials. Polymer. 50(4): 990-997 (2009).

25.   Caruso MM, Davis DA, Shen Q, Odom SA, Sottos NR, White SR, et al. Mechanically-induced chemical changes in polymeric materials. Chemical Reviews. 109(11): 5755-5798 (2009).

26.   Hansen CJ, Wu W, Toohey KS, Sottos NR, White SR, Lewis JA. Self-healing materials with interpenetrating microvascular networks. Advanced Materials. 21(41): 4143-4147 (2009).

27.   Natrajan V, Christensen K. Two-color laser-induced fluorescent thermometry for microfluidic systems. Measurement Science and Technology. Meas. Sci. Technol. 20(1): 015401 (2009).

28.   Natrajan V, Christensen K. Structural characteristics of transition to turbulence in microscale capillaries. Phys. Fluids, 21(3): 034104 (2009).

29.   Toohey KS, Hansen CJ, Lewis JA, White SR, Sottos NR. Delivery of two-part self-healing chemistry via microvascular networks. Advanced Functional Materials. 19(9):1399-1405 (2009). [Cover Feature]

30.   Toohey K, Sottos N, White S. Characterization of microvascular-based self-healing coatings. Experimental Mechanics, 49(5):707-717 (2009).

31.   Wilson G, Porter K, Weissman H, White S, Sottos N, Moore J. Stability of second generation grubbs' alkylidenes to primary amines: formation of novel ruthenium-amine complexes. Adv. Synth. Catal., 351(11-12):1817-1825 (2009).

32.   Cho, S.H., White, S.R., Braun, P.V., Self-healing polymer coatings, Advanced Materials, 21:645-649 (2009). [Cover Feature]

33.   Aragon AM, Geubelle PH, White SR. Multi-physics design of microvascular materials for active cooling applications. Journal of Computational Physics, 230(13):5178-5198 (2010).

34.   Hamilton AR, Sottos NR, White SR. Self-healing of internal damage in synthetic vascular materials. Advanced Materials, 22:5159-5163 (2010).

35.   White SR. (ed.) Special Issue on Self-Healing Materials, Journal of Composite Materials, 44: 2525 (2010).

36.   White SR, Geubelle PH. Self-healing materials: get ready for repair-and-go. Nature Nanotechnology, 5: 247-248 (2010).

37.   Kozola BD, Shipton LA, Natrajan, V. K., Christensen, K. T., White, S. R. Characterization of active cooling and flow distribution in microvascular polymers. Journal of Intelligent Material Systems and Structures, 21: 1147-1156 (2010).

38.   Aragon AM, Duarte AC, Geubelle PH. Generalized finite element enrichment functions for discontinuous gradient fields. International Journal for Numerical Methods in Engineering, 82(2): 242-268 (2010).

39.   Caruso MM, Blaiszik BJ, Jin H, Schelkopf, SR, Stradley DS, Sottos NR, et al. Robust, double-walled microcapsules for self-healing polymeric materials. ACS Applied Materials & Interfaces, 2(4):1195-1199 (2010).

40. Hamilton A, Sottos N, White S. Local strain concentrations in a microvascular network. Experimental Mechanics, 50(2): 255-263 (2010).

41. Wu W, Hansen CJ, Aragon AM, Geubelle PH, White SR, Lewis JA. Direct-write assembly of biomimetic microvascular networks for efficient fluid transport. Soft Matter, 6(4):739-742 (2010).

42. Blaiszik BJ, Kramer SL, Olugebefola SC, Moore JS, Sottos NR, White SR. Self-healing polymers and composites. Annual Review of Materials Research, 40: 179-211 (2010).

43. Natrajan V and Christensen K. Non-intrusive measurements of convective heat transfer in smooth- and rough-wall microchannels. Part I: laminar flow. Experiments in Fluids, 49 (5): 1021-1037 (2010).

44. Natrajan VK and Christensen, KT. The impact of surface roughness on flow through a rectangular microchannel from the laminar to turbulent regimes. Microfluid. Nanofluid., 9 (1): 95-121 (2010).

45. Olugebefola SC, Aragón AM, Hansen CH, Hamilton AR, Kozola BD, Wu W, et al. Polymer-microvascular network composites. Journal of Composite Materials. 44: 2587-2603 (2010).

46. Odom, S.A.; Caruso, M.M.; Finke, A.D.; Prokup, A.M.; Ritchey, J.A.; Leonard, J.H.; White, S.R.; Sottos, N.R.; Moore, J.S., "Restoration of Conductivity with TTF-TCNQ Charge-Transfer Salts," Advanced Functional Materials, 20, 1721-1727 (2010). [Cover Feature]

47. Wilson GO, Henderson JW, Caruso MM. Blaiszik BJ, McIntire PJ, Sottos NR, White SR, Moore JS. Evaluation of peroxide initiators for radical polymerization-based self-healing applications. J. Polym. Sci. Part A: Polym. Chem., 48:2698-2708 (2010).

48. Natrajan VK and Christensen KT Non-intrusive measurements of transitional and turbulent convective heat transfer in a rectangular microchannel. J. Micromech. Microeng., 21, 085001 (2011).

49. Esser-Kahn AP, Odom SA, Sottos NR, White SR, Moore JS. Triggered Release from Polymer Capsules, Macromolecules 44:5539–5553 (2011).

50. Esser-Kahn AP, Thakre PR, Dong H, Patrick JF, Vlasko-Vlasov VK, Sottos NR, Moore JS, White SR. Three-Dimensional Microvascular Fiber-Reinforced Composites, Adv. Mater, 23:3654-3658 (2011).

1.2 Patents resulting from the μVAC MURI program

1. M.W. Keller, N.R. Sottos, S.R. White Self-Healing Elastomer System, UIUC TF05186, U.S. Patent Application, Ser. No. 11/421,993, filed June 2, 2006; PCT Patent Application, PCT/US07/69981, filed May 30, 2007.Patent No: US 7,569,625 B2, August 4, 2009.

2. D. Therriault, J.A. Lewis, S.R. White, Microcapillary Networks, UIUC TF01092, U.S Patent Application, Ser. No. 11/558,084, filed Nov. 9, 2006. Patent 7,799,251 issued Sept. 21, 2010.

3. S.R. White, N.R. Sottos, B.J. Blaiszik, Capsules, Methods for Making Capsules, and Self-Healing Composites Including the Same, UIUC TF06182, U.S. Patent Application, Ser. No. 11/756,280, filed May 31, 2007; PCT Patent Application PCT/US08/65294, filed May 30, 2008.

4. M.M. Caruso, D.A. Delafuente, B.J. Blaiszik, J.M. Kamphaus, N.R. Sottos, S.R. White, J.S. Moore, Solvent-Promoted Self Healing Materials UIUC TF07085, U.S. Provisional Patent Application, Ser. No. 60/983,004, filed Oct. 26, 2007; PCT Patent Application, PCT/US08/81291, filed October 27, 2008. U.S. Patent Application Ser. No. 12/739,537 filed April 23, 2010.

5. K.S. Toohey, N.R. Sottos, J.A. Lewis, J.S. Moore, S.R. White, Self-Healing Materials with Microfluidic Networks, UIUC TF07101, U.S. Patent Application, Ser. No. 11/760,567, filed June 8, 2007; PCT Patent Application, PCT/US2008/66071, filed June 6, 2008.

6. S.R. White, S. Mookhoek, S. van der Zwaag, N.R. Sottos, B.J. Blaiszik, Multi-capsule System and its use for Encapsulating Active Agents, UIUC TF07090, U.S. Patent Application, Ser. No. 12/014,573, filed Jan. 15, 2008.

7. B. Beiermann, M.W. Keller, N.R. Sottos, S.R. White, Self Healing Laminate System, TF07142, U.S Patent Application, Ser. No. 61/023,698, filed Jan. 25, 2008. U.S. Patent Application, Ser. No. 12/359,631 filed Jan. 26, 2009.

8. S.R. White, N.R. Sottos, J.S. Moore, G.O. Wilson, B.J. Blaiszik, J.D. Rule, M.W. Keller, B.F. McCaughey, Multi-capsule System for Autonomic Healing, UIUC TF06183-US. Provisional U.S. Patent App, Ser. No. 61/174, 214 filed April 30, 2001. U.S. Patent App, Ser. No. 12/769, 904 filed on April 29, 2010.

9. S.R. White, N.R. Sottos, J.L. Moll, B.J. Blaiszik, Interfacial Functionalization for Self Healing Composites, UIUC TF07122, U.S. Patent Application, Ser. No. 61/090,116, filed August 19, 2008. UIUC TF07122-US Aug 18, 2009.

10. A. Esser-Kahn, H. Dong, P. Thakre, J. Patrick, N.R. Sottos, J.S. Moore, S.R. White, Microvascular Network Materials and Composites for Forming the Materials, UIUC TF10047, U.S. Provisional Patent Application 61/451,698, filed March 11, 2011.

11. M. Caruso, C. Mangun, L.G. Reifschneider, S.R. White, J.S. Moore, Injection Molding Thermoplastics containing Microcapsules for Solvent-Based Self-Healing," UIUC TF09081-PRO. U.S. Provisional Patent Application 61/453,324 filed March 16, 2011.

12. S.R. White, J.S. Moore, N.R. Sottos, B.J. Blaiszik, M.M. Caruso, C.L. Mangun, L.G. Reifschneider, Thermally Robust Microcapsules for Self-Healing Polymeric Materials, UIUC TF09085, U.S. Provisional Patent Application 61/453,324, filed March 16, 2011.

2.1 Theme I: Functional Materials Systems & Chemistries

A variety of activities were undertaken within this theme to enhance the functional performance of autonomic systems. Initially, efforts were focused on sensing and monitoring the healing reaction and development of alternative healing chemistries. During the course of the MURI program we also developed new encapsulation techniques and programmable microcapsules that release in response to environmental triggers. Each of these topics are summarized and briefly highlighted below.
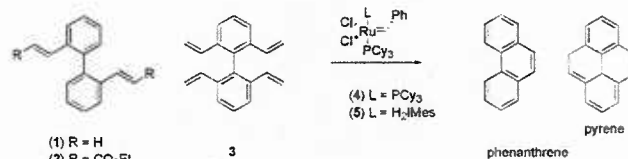
2.1.1 Sensing and monitoring healing

A concept of detecting damage and monitoring the progress of healing has been proposed based on simultaneous healing and sensing reactions. The concept is exhibited with two parallel channels and well dispersed Grubbs' catalyst particles embedded together in a polymer matrix. A constant flow of DCPD and a pro-signal
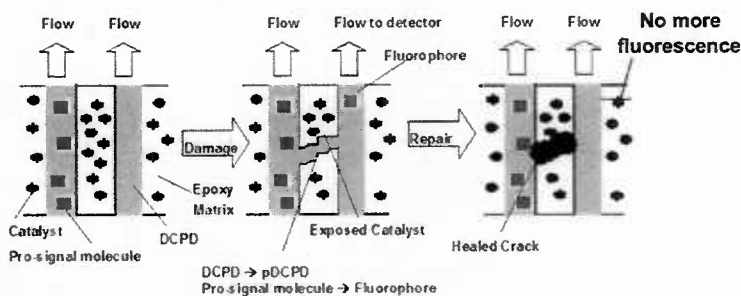
Figure 1. *Schematic of device designed for studying in-situ damage and healing mechanisms.*

molecule (PSM) in the left channel and DCPD alone in the right channel is maintained (Figure 1). When a crack crossing the two parallel channels is introduced, ring opening metathesis polymerization (ROMP) of DCPD and ring closing metathesis (RCM) of the PSM occur simultaneously in the presence of exposed catalyst. The formation of a fluorophore from the PSM by RCM results in a significant increase in fluorescence intensity. ROMP of DCPD occurs until enough poly(DCPD) has been formed to heal the crack. At this point, the PSM can no longer flow out of the left channel and no more RCM occurs and fluorescence intensity decreases significantly.

PSMs **1**, **2** and **3** were synthesized and subject to RCM conditions as shown in Figure 2. However, only the reaction with compound **1** was successful with first and second generation Grubbs'

Figure 2. *Reaction of PSMs with first and second generation Grubbs' catalyst.*

catalyst (**4** and **5**). RCM of **1** was found to be competitive with the ROMP of (DCPD) by ^{1}H NMR. Solution ^{1}H NMR studies also showed that 18 and 21% RCM of **1** occurred in the presence of DCPD with **4** and **5** respectively.
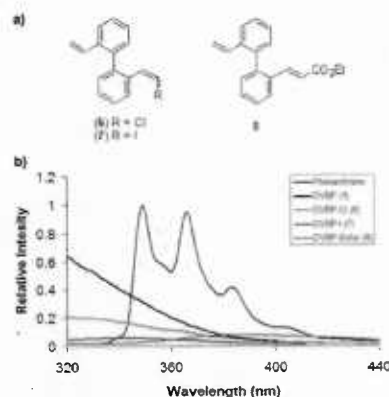
Unfortunately, since the fluorescence intensity of **1** relative to phenanthrene (RCM product) was too high, the PSM **1** would have to undergo at least a 50% conversion to phenanthrene for the signal intensity to be recorded. Therefore, PSMs with fluorescence intensities significantly lower than phenanthrene must be used. To this end, a new set of PSM s (Figure 3a) were synthesized and

their fluorescence intensities relative to phenanthrene (Figure 3b) showed a dramatic decrease by functionalization with electron withdrawing groups and "heavy atoms" (Skoog et al. 1998).

2.1.2 Improved ROMP-based healing chemistries

ROMP-based self-healing chemistry previously reported used the commercially available *endo*-stereoisomer of DCPD due to its long shelf-life, ready availability, and good mechanical properties of the resulting polymer. However, *endo*-DCPD is known to have a slower polymerization rate than the *exo*-isomer, and this would seem to limit the kinetics of damage repair. Obviously it would be desirable to have the fastest healing kinetics possible so long as the quality of the repair is not compromised. For *endo*-DCPD approximately 25 minutes are required before any detectable self-healing begins, and 10 h are required for full recovery of mechanical

Figure 3. a) new PSMs with various quenchers. b) Fluorescence spectra of phenanthrene and new PSMs. All concentrations are 10 mM in acetonitrile.

toughness (Brown et al. 2002). These rates are certainly slower at lower temperatures which, in addition to the relatively high melting point of *endo*-DCPD, limit the temperature window over which healing can occur. In contrast, *exo*-DCPD has a gel time that is approximately 150 times faster than *endo*-DCPD, and the monomer itself does not solidify until temperatures below -50° C (Smirnova et al. 1997). Thus, the faster polymerizing *exo*-DCPD may be useful for low temperature applications. Because the healing event is a complex problem that involves monomer transport, catalyst dissolution and transport, and polymerization, it remains to be determined how important the faster *exo*-DCPD reaction kinetics is to the overall rate of healing, and efficiency of healing.

In this study, *exo*-DCPD is incorporated into ROMP-based autonomic healing in an attempt to take advantage of these favorable kinetic properties. We also discovered and partially adverted problems affecting healing efficiencies that occur using fast healing agents. We measure energy to failure of healed specimens as a function of healing time and compare the kinetics of damage repair for *endo*- and *exo*-DCPD (Figure 4), and mixtures of the two isomers. Using catalyst loading levels previously reported to be effective for *endo*-DCPD, *exo*-DCPD was found to heal about 20 times faster than the *endo* isomer, but with a lower healing efficiency (Figure 5). The fracture toughness of the repaired specimens decreased when the *exo* content of blends was greater than 40% and, for pure *exo*- DCPD, when catalyst loadings were below 1%. Possible causes of the reduced healing efficiencies of the *exo*-
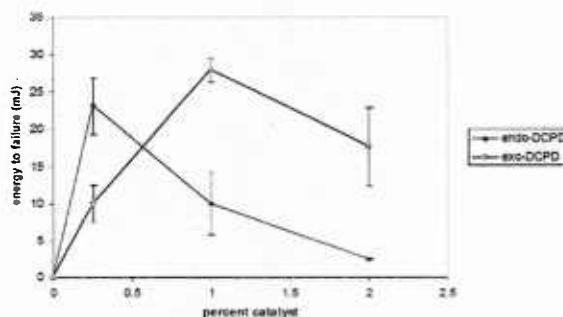

Figure 4. Effect of overall catalyst loading (10 wt % Grubb's catalyst in wax and various loadings of wax microspheres in epoxy) on energy required to fail self-activated TDCB samples with the stereoisomers of pDCPD.
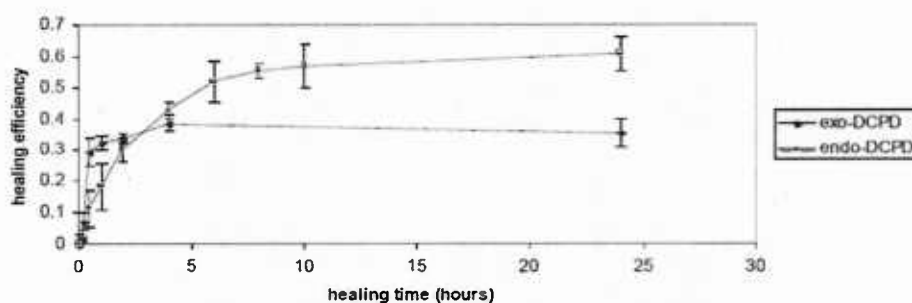
Figure 5. Progress of healing effeciency in endo-DCPD and exo-DCPD tested with self-activated protocols. A 5 wt % wax microsphere loading with 5 wt % first-generation, lyophilized Grubb's catalyst was used.

DCPD healing agent are being explored.

As a means to further exploit the faster healing kinetics of *exo*-DCPD, we briefly examined its ability to heal at low temperatures. Figure 5 shows load–displacement curves for the *exo* and *endo* isomers of DCPD cured in a cold room with a temperature range of 0-4° C. From the complete lack of healing shown in Figure 6a, we suspect that solidification of the monomer due to freezing limits *endo*-DCPD's healing capabilities. The temperature range of the cold room was below the 15 °C mp of *endo*-DCPD stabilized with 4-*tert*-butylcatechol, therefore the encapsulated healing agent solidified. *Exo*-DCPD, which freezes at temperatures below -50° C, showed no degradation in healing at this temperature range (Figure 6b).
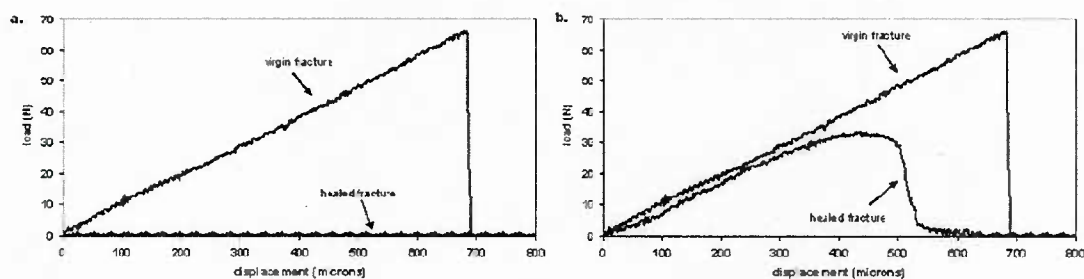

Figure 6. Load–displacement curves of healed in-situ TDCB samples of a) endo-DCPD and b) exo-DCPD. Samples containing 5 wt% loading wax microspheres with 5 wt% Grubb's catalyst at temperatures ranging from 0-4 °C [Mauldin et al. 2007].

## 2.1.3 Alternative catalysts for ROMP-based healing

Three variations of Grubbs' catalyst were chosen for evaluation. First generation Grubbs' catalyst (**1**) has been used in a wide variety of self-healing applications with excellent results (White et al. 2001, Brown et al. 2002, Brown et al. 2005b, Kessler et al. 2003, Rule et al. 2005, Rule et al. 2007), second generation Grubbs' catalyst (**2**) has been reported to exhibit improved reactivity and thermal stability (Scholl et al. 1999, Bielawski et al. 2000, Huang et al. 1999) and Hoveyda-Grubbs' catalyst (**3**) has demonstrated impressive chemical stability and recyclability (Garber et al. 2000, Wakamatsu et al. 2002, Bieniek et al. 2006). Our evaluation of these catalysts

for self-healing include a comparison of their ROMP initiation kinetics, chemical stability to epoxy curing agents, thermal stability, and ROMP of functionalized healing agents aimed at improving adhesive strength in self-healing polymers via non-covalent interactions.

(1)   **(2)**   **(3)**
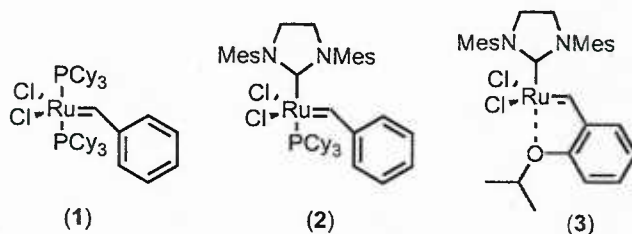
While both catalyst **2** and **3** exhibited faster initial ROMP kinetics in solution, these rates did not translate into improved healing performance due to slower initiation rates in bulk polymerization in the case of **2** and the combination of extremely fast initiation rates and poor solubility of **3** in DCPD. However, **2** showed significant improvements in chemical stability to primary amine epoxy curing agents, thermal stability, and reactivity with alternative ROMP monomers. Self-healing was quantified by fracture toughness recovery tests using samples cast in the tapered double cantilever beam (TDCB) geometry (Brown et al. 2002). Samples containing freeze-dried **2** and **3** that dissolve and react with the epoxy sample curing agent exhibited measurable healing, while no healing was observed for similar samples containing **1** (Figure 7). It appears that the presence of N-heterocyclic ligands that are not easily displaced in **2** and **3** facilitate the formation of new catalyst complexes in-situ that maintain some metathesis activity. In contrast, **1** contains only phosphine ligands which are both displaced in-situ by the primary amine curing agents present in significant excess of the catalyst, resulting in the formation of transient bis-DETA complexes that decompose.
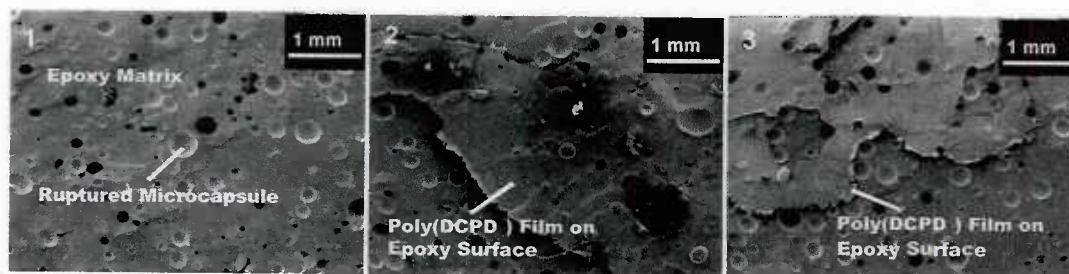
Figure 7. Scanning Electron Microscopy (SEM) images of representative fracture planes for in situ epoxy samples containing 2.5 wt% catalyst and 10 wt% microcapsules (average diameter = 250 ± 32 μm). After fracture, the samples were left to heal for a 24 h before retesting. The number labels on the images correspond to the catalyst incorporated into the matrix.

The thermal stabilities of the three catalysts were evaluated by measuring the retention of critical fracture load $(\eta_{avg(r)})$ for samples postcured at elevated temperature (125°C) versus samples postcured at 35°C. Catalyst **2** exhibited the best retention of fracture load for samples healed at room temperature and at 125°C (Table 1).

$$\eta_{avg(r)} = \frac{\mathrm{Avg}\ [P_{C\ Cured(T,125)}^{Healed}]}{\mathrm{Avg}\ [P_{C\ Cured(T,35)}^{Healed}]} \qquad (1)$$

5-norbornene-2-carboxylic acid (NCA) was evaluated as a healing agent additive for adhesion promotion in self-healing polymers. Reference tests were performed with a mixture of DCPD (75

Table 1. Summary of healing performance for epoxy samples containing 1.5 wt% catalyst, postcured at 125°C and healed at RT or 125°C. Control samples contained no catalyst showed no healing.

Catalyst	No. of Samples	Healing Temperature (°C)	Peak Fracture Load (N) of Healed Sample	Retention of Healing Capacity ($\eta_{avg.(r),}$ %)
None	3	RT	0	N/A
1	3	RT	23.1[3.5]	77
2	3	RT	22.4[6.0]	84
3	4	RT	5.3[2.1]	18
None	3	125	0	N/A
1	3	125 °C	32.8[12.1]	109
2	4	125 °C	57.6[13.3]	216
3	3	125 °C	16.7[6.0]	57

mol.%) and NCA (25 mol.%) pre-mixed with **1, 2** or **3**. No healing of reference test samples were observed for **1** and mixtures containing **3** polymerized too quickly to be used in reference tests. Reference test results for three different epoxy matrices (Table 2) healed with mixtures containing **2** are summarized in Figure 8. The addition of NCA to the healing agent mixture results in significantly improved healing performance over DCPD and the DCPD/ethylidene-2-norbornene (ENB, 25 mol.%) mixture. We attribute the adhesion promotion due to NCA observed in M_1 and M_3 to non-covalent interactions between the polymerized healing agent and the matrix since both have a higher percentage of functional groups capable of hydrogen bonding relative to M_2.

Table 2. Matrix formulations.

Matrix Designation	Resin	Additive [wt%]	Curing Agent [wt%]	H_2O Contact Angle (degrees) [a]
M_1	EPON 828	N/A	DETA [10.7]	81[1]
M_2	EPON 828	HELOXY 71 [28.5]	Ancamine K54 [9.0]	82[3]
M_3	EPON 862	N/A	EPICURE 3274 [33.3]	60[3]

[a] Standard deviation for contact angle measurements in square brackets.
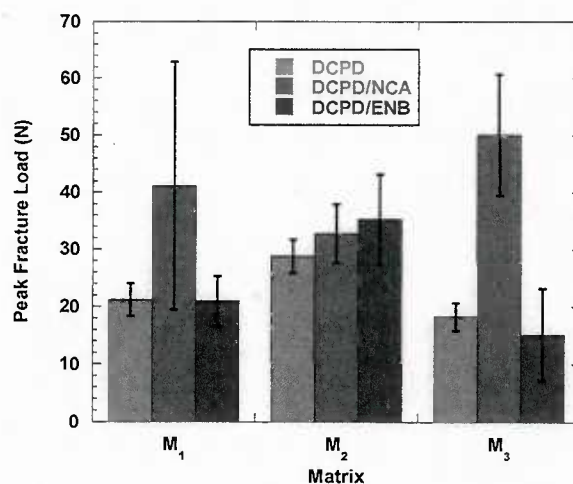
Figure 8. *Average peak fracture loads of M_1, M_2 and M_3 samples healed with DCPD, DCPD/NCA and DCPD/ENB. Each data point is an average of data for 3-4 samples and the error bars represent one standard deviation.*

2.1.4 Solvent-based healing

We have discovered that a number of common organic solvents are capable of healing epoxy materials. By incorporating these solvents into microcapsules dispersed in the epoxy resin, a material capable of autonomic healing is created. Only solvent-filled microcapsules are needed for healing; no catalyst phase is required. The degree of cure and stoichiometric amounts of epoxy and amine components of the resulting thermoset polymer are important to the degree of healing observed.
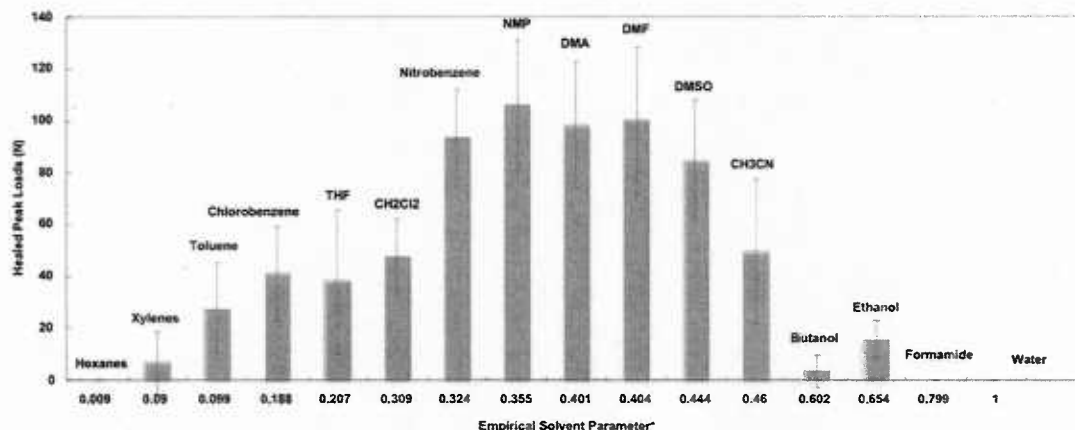
Figure 9. *Summary of reference tests for various solvents exhibiting self-healing as a function of polarity (solvent parameter adapted from Reichardt, Christian. Solvents and Solvent Effects in Organic Chemistry. New York: VCH, 1988).*

After a customary cure cycle of 24 hours at room temperature, followed by 24 hours at 35°C, the epoxy-amine matrix is only 80% cured, as evaluated by differential scanning calorimetry (DSC). Introducing solvent into this partially-cured system allows any excess epoxides to react with unreacted amines to complete the curing process at room temperature. The mid-range polarity solvents exhibit the best healing potential when manually injected into the crack plane of a TDCB specimen (Figure 9). Extending this result to a fully *in situ* system, we successfully microencapsulated chlorobenzene and dispersed the capsules in the resin matrix.

When a crack propagates through the resin, it ruptures the microcapsules, releasing solvent into the crack plane. The solvent dissolves excess epoxy and unreacted amines in the crack plane to facilitate a reaction that bonds the crack and restores structural continuity. Self-healing was observed for various capsule loadings (Figure 10) via short-groove TDCB specimens (Rule et al. 2007). Control tests using encapsulated xylenes and hollow microcapsules show minimal and no healing, respectively. This one-component self-healing approach is ideal for microvascular
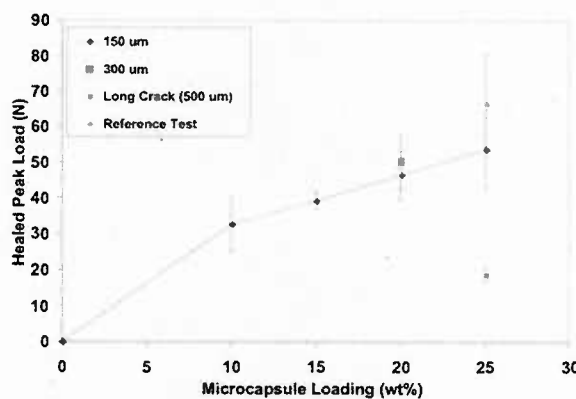
Figure 10. *In-situ healing with chlorobenzene microcapsules of various diameters.*

systems since only one type of liquid is transported throughout the matrix, eliminating potential challenges associated with mixing of two components.

Building on the initial successes using encapsulated solvents, we have shown that several non-toxic solvents are also capable of self-healing to high healing efficiency. Urea-formaldehyde (UF) microcapsules containing solvent cores of phenylacetate (PA), ethyl phenylacetate (EPA), and hexyl acetate have been prepared and characterized. Reference tests were conducted in which manually injected solvents were introduced into crack plane of tapered double cantilever beam (TDCB) long groove specimens and reported healed peak loads similar to that of chlorobenzene (Caruso et al. 2007) (Figure 11).

When a small amount (5-20 wt%) of epoxy monomer was encapsulated with chlorobenzene, healing efficiencies of ca. 100% were obtained

Figure 11. Healing performance of three solvents. The reference test point is for manually solvent (30 µL) and the in situ test was done using 200 µm average diameter UF solvent microcapsules at 15 wt.-% loading. Error bars represent standard deviation based on 5 short groove TDCB specimens.

(Caruso et al. 2008). In order to determine the effect of encapsulated epoxy on healing efficiency a series of tests were conducted in which the amount of solvent delivered to the crack plane was held constant while the amount of epoxy delivered as systematically varied. The total mass of healing agent fluid delivered to the crack plane was calculated as,

$$M_{healing} = \rho_s \phi D_c \qquad (1)$$

where ρ_s is the density of the matrix, ϕ is the mass fraction of microcapsules, and D_c is the mean diameter of the microcapsules (Rule et al. 2007). Equation (1) was modified to separate the mass of healing agent delivered (mg/cm^2) into the two components used in our capsules,

$$M_{epoxy} = \rho_s \phi D_c \varepsilon \qquad (2)$$

$$M_{solvent} = \rho_s \phi D_c (1 - \varepsilon) \qquad (3)$$

where the quantity ε represents the weight fraction of epoxy resin in the capsules. Equs. (2)-(3) collapse to Eq. (1) when $\varepsilon = 0$ (solvent capsules) or $\varepsilon = 1$ (epoxy capsules), respectively.

These equations can be used to calculate the required concentrations of capsules varying ε

Figure 12. Healing efficiencies reported for in situ short groove TDCB fracture testing with varied amounts of epoxy delivered to the crack plane with the amount of chlorobenzene delivered held constant at 3.15 mg cm^{-2}. Error bars represent the standard deviation based on 5 samples.

values in order to maintain a constant delivery of epoxy or solvent. In our experiments, a mixture of pure chlorobenzene capsules and epoxy-chlorobenzene capsules were used to prepare fracture
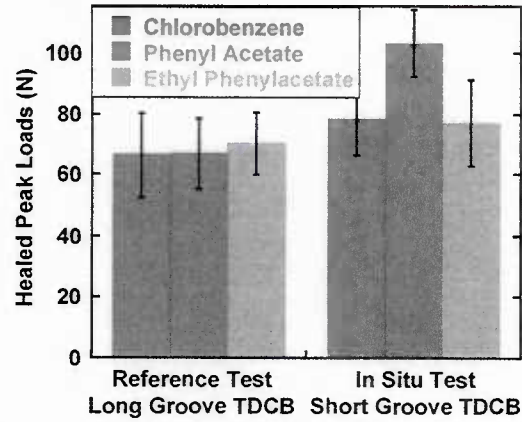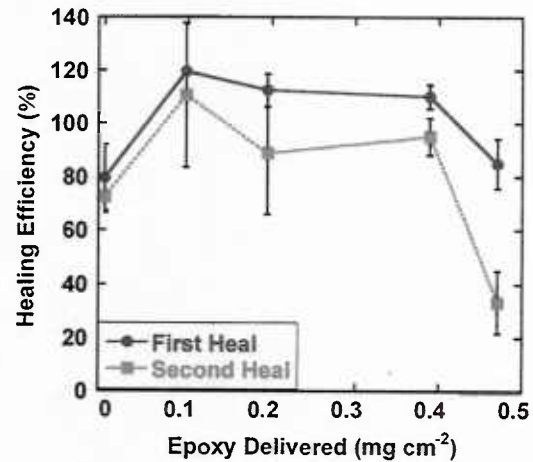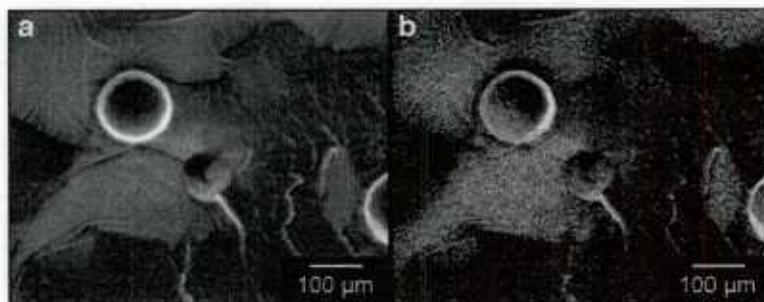
specimens and the results are shown in Figure 12. After 24 h from the initial virgin fracture, the samples were retested to fracture. We further tested the healed samples a second time and found that multiple healing cycles were obtained (due primarily to crack path deviation between the first and second fracture events). The average healing efficiencies are reported in Figure 2 for each data series.
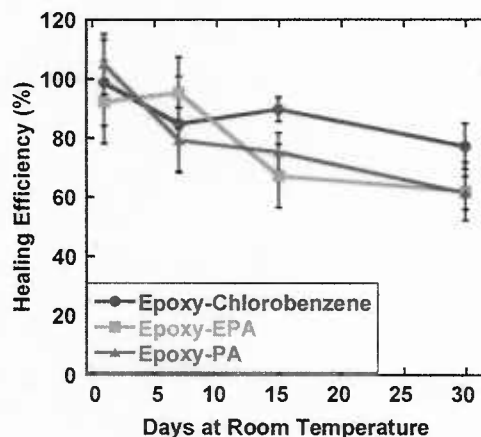
Using the technique of energy dispersive X-ray spectroscopy (EDS), the new film formed in the crack plane of specimens has been identified to result from the encapsulated epoxy curing on the surface. A brominated epoxy, EPON 1163, was encapsulated with chlorobenzene using the UF method[4] at a concentration of 0.447 $\underline{M}$ (equivalent to 13% by weight that had previously been used with EPON 828). Short

Figure 13. (a) SEM image of the fracture surface showing new film formed on the healed crack plane. (b) SEM image with an elemental map showing carbon in red and bromine in yellow.

groove TDCB fracture samples were prepared with 15 wt.-% capsules to report $\eta = 0.81 \pm 0.21$.

The fracture surfaces were analyzed by SEM to show a film (Figure 13a). Previously, this new film was indistinguishable from the matrix, but by using the brominated epoxy in microcapsules, the film clearly shows the presence of this element by EDS mapping (Figure 13b).

As a control experiment we identified hexyl acetate as a solvent that was too nonpolar to show a solvent healing effect and could be encapsulated using the UF in situ polymerization method (Brown et al. 2003). Hexyl acetate neither swelled the matrix epoxy nor demonstrated any degree of healing from reference or in situ testing. Thus, microcapsules containing 13% epoxy-hexyl acetate were prepared, incorporated into fracture specimens, and displayed a m inimal amount of healing ($\eta = 0.20$). No new material film was observed on these fracture surfaces. Microcapsules containing 80% epoxy-hexyl acetate ruptured upon crack damage, but released too much epoxy into the crack plane to provide any recovery of fracture toughness ($\eta = 0$). A thick epoxy layer (~ 50 nm) formed on the crack plane of the uncured epoxy material. These control experiments explicitly showed how both the solvent and epoxy effects contributed to 100% healing efficiencies observed.

Figure 14. Stability of epoxy-chlorobenzene and epoxy-EPA capsule systems (15 wt% loading) shown over time for samples exposed to ambient conditions before fracturing. Healing data was acquired after 24 h from fracture event and error bars represent standard deviation based on 5 short groove TDCB specimens.

With the discovery of a system that completely recovered the virgin fracture toughness, we sought to test its stability over time through aging studies. Short groove TDCB specimens were prepared with 15 wt% microcapsules of epoxy-solvent with no virgin crack and exposed to ambient conditions for varying time periods. After specified time periods, the samples were precracked and fractured. The degree of healing measured 24 h after the initial fracture event is reported in terms of healing efficiencies (Figure 14). Within experimental scatter, the healing efficiencies decrease only slightly over the time period of a month.

After evaluating solvent healing performance under monotonic loading conditions (Caruso et al. 2008; Caruso et al. 2007) we tested the performance of this healing system during fatigue. Using the previous experimental protocols used by our group and the tapered-double-cantilever-beam (TDCB) sample geometry (Brown et al. 2005a; Brown et al. 2005b; Brown et al. 2006; Jones et al. 2007), samples were subjected to a sinusoidal loading profile at 5 Hz frequency. The maximum applied load of 46.7 N corresponds to $K_I = 0.52$ MPa·m$^{1/2}$ which is 65% of the K_{IC} for neat epoxy (0.8 MPa·m$^{1/2}$) and 48% of the K_{IC} for epoxy specimens with embedded microcapsules (1.1 MPa·m$^{1/2}$). Samples were tested at $R = 0.1$, and $\Delta K = 0.472$ MPa·m$^{1/2}$.

Four different sample types were tested in our experiments. For controls, neat epoxy specimens and epoxy samples containing non-healing solvent (hexyl acetate) microcapsules were used. Self-healing samples were tested consisting of both pure EPA solvent microcapsules and epoxy-EPA microcapsules. Figure 15 shows a representative crack growth plot for a neat epoxy sample and defines the crack growth rate as the best fit line within the constant K region (Brown et al. 2005a).
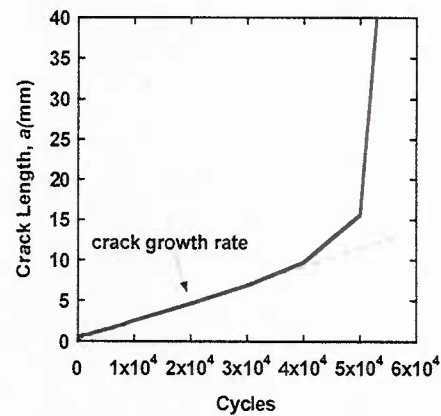

Figure 15. Crack growth for a neat epoxy TDCB specimen at a loading of $\Delta K = 0.472$ MPa·m$^{1/2}$ at 5 Hz.

A summary of results for the four types of specimens is given in Table 3. All samples were cured for 24 h at RT (22°C), followed by 24 h at 35°C, and a further 6-7 days at RT (22°C). All samples with microcapsules contained 15 wt% microcapsules in the insert of the TDCB. When compared to neat epoxy, the crack growth rate of the solvent control samples was slower, demonstrating the fatigue life extension of samples that contain microcapsules that has been previously observed (Brown et al. 2005b; Brown et al. 2006). Self-healing specimens exhibit a dramatic reduction in crack growth rate (approximately two orders of magnitude) and were removed from the load frame after two weeks of testing without failure. Self-healing during fatigue dramatically slows crack propagation and leads to a remarkable increase in lifetime.

Table 3. Summary of fatigue experiments at $\Delta K = 0.472$ MPa·m$^{1/2}$

Sample Contents	# of Samples	ΔK (MPa·m$^{1/2}$)	Total # of Cycles	Crack Growth Rate (mm/cycle)	Specimen
Neat Epoxy	4	0.472	5.1e4 ± 2.4e4	2.4e-4 ± 1.0e-4	CONTROL
Hexyl Acetate	4	0.472	3.1e5 ± 2.2e5	3.8e-5 ± 2.5e-5	Solvent Control
EPA*	6	0.472	2.5e6 ± 1.6e6	2.1e-6 ± 9.4e-7	Self-Healing
Epoxy-EPA*	4	0.472	3.4e6 ± 1.8e6	1.4e-6 ± 5.8e-7	Self-Healing
* = samples not cycled to failure					

2.1.5 Thermal stability of microcapsules

To prepare and form composite matrices in commercial materials, high temperatures are often required. The incorporation of solvent-filled capsules can be problematic if the processing temperature is near the boiling point of the solvent or the degradation point of the microcapsule shell wall. In particular, it was found that solvent-filled urea-formaldehyde (UF) capsules lose a significant amount of their core material at processing temperatures below 200°C over time. Thus, we have developed a method for the preparation of double walled, polyurethane (PU), polyurea microcapsules in a single batch process that result in more thermally robust microcapsules. The polyurea exterior coating allows the microcapsules to bond well to epoxy for efficient rupture in a self-healing material, a major problem with polyurethane single walled capsules (Cho et al. 2006).

Compared to examples from literature (Li et al. 2008), our method simplifies the synthesis of these capsules by performing both reactions simultaneously. In addition, no secondary reaction with the interior polyurethane precursor is required because the multifunctional PU prepolymer can react directly with the water at an elevated temperature to form a dense polymer. This lack of a secondary reaction component is critical when the core composition comprises a reactive material, such as an epoxy resin. The use of a standard PU cross-linker (i.e. polyamine) may cause an undesired polymerization reaction with the core epoxy composition.

This modified encapsulation method has allowed us to encapsulate a wide variety of healing agents with more robust polymeric shell walls. For example, ethyl phenylacetate (EPA) and dicyclopentadiene (DCPD) monomer have been encapsulated using this improved method at a variety of sizes. It was determined by SEM that the addition of increasing amounts of polyurethane resulted in thicker shell walls (Figure 16).

In order to predict the capsule stability at high temperatures, thermogravimetric analysis (TGA) was employed. The double wall allowed for increased thermal stability of the microcapsules, which was analyzed by quantifying mass loss during isothermal TGA experiments (Figure 17). The mass loss for the UF/PU shell wall capsules was significantly lower than that of UF capsules, demonstrating a more robust method for encapsulating lower boiling point liquids.
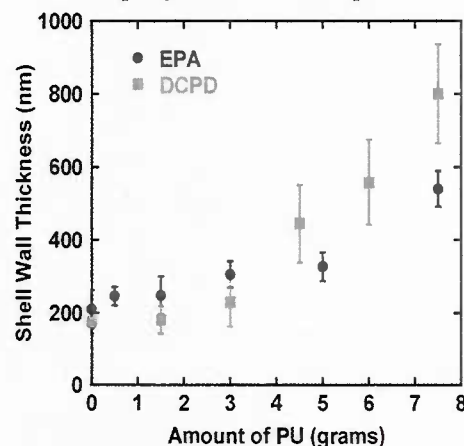

Figure 16. Shell wall thickness of microcapsules produced as a function of the amount of PU added to the encapsulated core solvent/monomer.
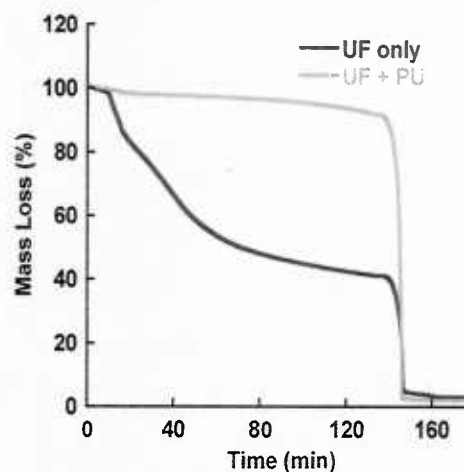

Figure 17. Representative Isothermal TGA curves (2 h at 180°C) for EPA capsules with UF shell walls and the double UF + PU shell walls.

2.1.6 Programmable microcapsules from self-immolative polymers

Autonomous repair of damaged devices remains an ongoing challenge in the field of materials science. Our approach has used the release of compartmentalized chemicals via rupture of microcapsule by crack propagation (White et al. 2001; Caruso et al. 2009). Beyond repair of structural materials, restoration of other functions such as optical and electronic properties could benefit from the triggered release of a healing fluid (Williams et al. 2007), but technology for rupturing microcapsules is currently limited by the need for direct, mechanical interaction between the capsule and the damage. In ideal self-healing systems, capsules could release healing agent in response to various physical, chemical or biological signals. We have developed a general approach to programmable microcapsules that release their core when triggered by a specific event that ruptures the shell-wall.
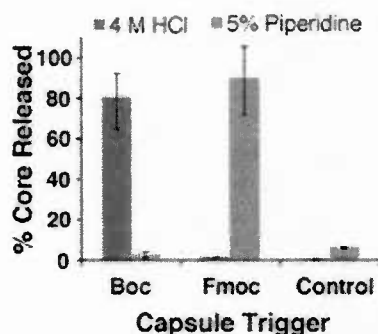

Figure 18. Percentage of core released after 48 h in triggering solution. (Blue – 4M aq. HCl w/ 10% EtOH, Red – 5% Piperidine in THF).

In order to create programmable capsules, we changed the chemistry of the shell wall constructing it from self-immolative polymer networks that undergo a head-to-tail depolymerization upon removal of a triggering end group (Sagi et al. 2008). The 'trigger' is a carbamate-based protecting group. Thus far, we have synthesized capsules that are sensitive to either HCl (containing a Boc protecting group) or piperidine (Fmoc protecting group), but many other variations can easily be imagined. Construction of the self-immolative polymer followed similar methods to Sagi et al. (Sagi et al. 2008) The trigger-loaded polymers were transformed into microcapsules by conversion into a reactive pre-polymer. Microcapsules (MC) we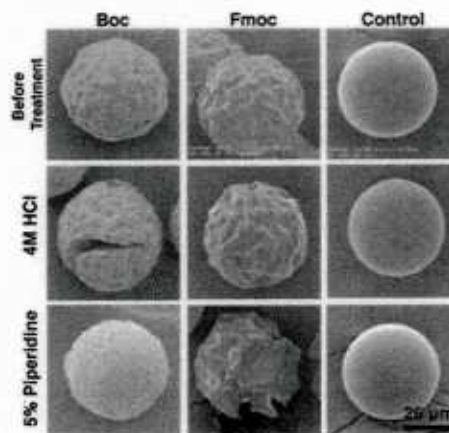re synthesized via an interfacial polymerization method (Yang et al. 2008). We synthesized two types of microcapsule, one whose shell wall consisted of polymer networks terminated with a Boc group (sensitive to acid) and one terminated with an Fmoc groups (sensitive to base). Capsules were routinely produced in the size range of 5-40 μm. The size and shell-wall morphology were determined by fluorescence, optical and scanning electron microscopy. The capsule shell-wall is fluorescent, indicating the presence of the immolative polymer. We constructed control capsules using polymer Desmodur L75, a commercially available pre-polymer composed of crosslinked 2,4-TDI, (**Control**).

We found that capsules loaded with a given trigger rupture upon exposure to conditions specific to the removal of that group (hereafter referred to as triggering conditions). **Boc** and **Fmoc** microcapsules were both exposed to 4M aq. HCl w/ 10% EtOH and 5% piperidine in THF, conditions known to trigger the Boc and Fmoc protecting groups respectively. In order to monitor the triggered release of the microcapsules' content, we measured the amount of core contents (Ethyl phenylacetate, EPA) released after 48 h by Gas Chromatography (GC) (Yang et al. 2008) after immersion in each of the different triggering solutions. The results are presented as the percentage core released compared to that released upon manually rupturing the capsules (Figure 18). Capsules released their core contents (EPA) upon exposure only to the conditions specific to the trigger removal while capsules exposed to conditions in which the trigger is unreactive showed little to no release of core contents (EPA). Additionally, control capsules without a self-immolative shell wall (**Control**) showed no release under any triggering conditions.

We examined the capsules shell morphology to confirm that rupturing of the shell-wall was the mechanism of release. Following exposure to the triggering conditions (Figure 19), SEM was used to visualize changes in shell-wall morphology. Microcapsules exposed to their matching triggering conditions appear cracked and in some instances deflated whereas capsules exposed to the non-matching triggering conditions appear unaffected. The morphology of the control capsules was unaffected by both triggering conditions (Figure 2). Combining these observations with the core release data, we conclude that triggering conditions caused a chemically specific rupture of the polymer shell wall coincident with release of core contents.

Figure 19. Changes in shell-wall morphology. Capsule shell walls are shown before and after 48 h exposure to triggering solutions.

There are potentially over 100 protecting groups that are synthetically amenable to our method (Wuts et al. 2006) and still others that could be triggered enzymatically (Pathak et al. 1998). We envision that this will allow the rapid prototyping of capsules that can be made to release their contents upon activation of various chemical, physical or biological stimuli. These types of "on-demand" chemical systems could find use in areas as diverse as drug-delivery to self-healing Li-ion batteries that are safer and longer lasting.

2.2 Theme II: Network Fabrication & Integration

Within this theme research activties were focused on the creation of microvascular networks in polymeric structures in both planar and 3D forms, as well as the characterization of their structure and flow behavior. A significant effort was focused on the Direct Ink Writing (DIW) technique for planar or 2.5D structures. Two new 3D fabrication techniques were also developed for Omni-Directional Printing (ODP) and Vaporization of Sacrificial Components (VaSC). Each of these topics are summarized below.

2.2.1 Direct-Ink Writing of Microvascular Networks

Computationally Guided, Microvascular Network Design

We created microfluidic networks dictated by computational designs in order to validate computational predictions. The first step in this combined experimental and simulation approach was to produce a baseline 2D network that contains orthogonal connections between all vertices (see Figure 20). This network (channel diameter of 100 µm) was produced by DIW of a fugitive organic ink

(a)   (b)

Figure 20. (a) CAD file and (b) optical image of baseline 2D microvascular network.

(Therriault et al. 2003) in the pattern shown in Figure 20(a). Fluid flow tracking and pressure measurement were carried out on a number of variations of networks to provide experimental data for computational validation. Optimal networks designed by genetic algorithms (Theme III) were then produced by DIW for experimental testing.
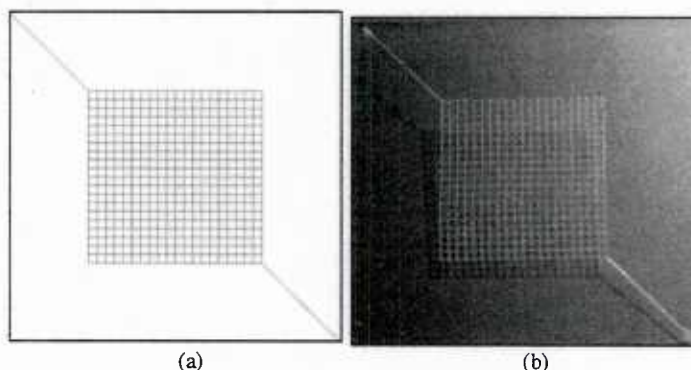
DIW of bio-inspired networks

The hierarchical microvascular architectures found in leafs enable high axial conductance with small radial diffusion and minimal loss of water potential, resulting in a relatively homogeneous fluid distribution (Zwieniecki 2002). Using multi-nozzle extrusion, dynamic speed, and pressure variation, the hierarchical order of an ivy leaf vascular structure is recreated by direct writing (see Figure 21). Vertical printing is used to achieve the "leaky conduit" properties of leaf vascularization and to facilitate ink removal. Fluorescent imaging revealed that the dye primarily flows into the low-order, larger microchannels before filling the higher order channels, mimicking the fast axial flow and slow radial diffusion that occurs naturally in leaf venation. The network hydraulic resistivity is characterized using the high pressure method (HPM) (Sack 2002) and compared to uniform periodic lattices and branched structures that obey Murray's Law. Results show that the hydraulic resistivity of the leaf structure is significantly lower than lattice and branched structures under similar domain coverage and channel volume constraints. Branched structures that obey Murray's law have a marginally lower resistivity than the periodic counterparts.

We have designed bifurcating microvascular networks with hierarchical channel diameters that obey Murray's law to demonstrate the integration of physiologically inspired network optimization into self healing and cooling structures fabricated by direct-write assembly. Variations in key writing parameters, including the applied pressure and speed, were examined to optimize network fabrication. A new fugitive ink consisting of a microcrystalline blended with heavy mineral oil was developed to print a range of filament diameters under applied pressures ranging from 0-700 psi.
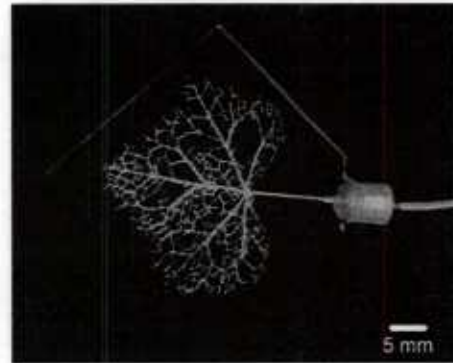
Figure 21. A fluorescent image of a hierarchical microvascular network assembled by DIW, which mimics leaf venation.

Unlike prior wax-based fugitive inks, this new ink exhibits much a lower shear yield making it more suitable for direct-write assembly. The branched structures are characterized by measuring the hydraulic conductance using a high-pressure flow meter. When structures possessed variations in channel diameter that did not comply with Murray's law, they showed a decrease in conductance under constant vascular volume conditions, suggesting lower fluid delivering efficiency. Figure 22 summarizes the results from a 4-generation bifurcating micro-vascular network, where both the normalized and actual hydraulic conductance is plotted as a function of microchannel architecture. The architecture is defined by the ratio of the sum of microchannel radii cubed of daughter branches divided by the sum of the microchannel radii cubed of the parent branch, where only the ratio of unity corresponds to microvascular networks that obey Murray's law. Two key trends emerge – first, the maximum hydraulic conductance is observed when Murray's law is obeyed, and second, there is excellent agreement between the measured and predicted values (Guebelle group) of the normalized hydraulic conductance for 4-generation networks of varying design.
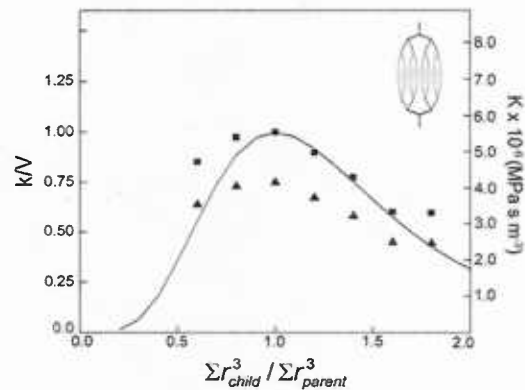

Figure 22. Four-generation microvasular networks in which their normalized (■) and actual (▲) hydraulic conductance is plotted as a function of network architecture. The analytical solution for the normalized data is denoted by solid line.

2.2.2 Omni-directional printing (ODP) of microvascular networks

We have extended our direct-ink writing capabilities to create 3D biomimetic microvascular networks using omnidirectional printing (ODP). Previously, 3D structures created with direct-ink writing have relied on self-supporting fugitive ink scaffolds, thus limiting the type of architectures available. Now, we print a wax-based fugitive ink into a reservoir containing a supporting medium that consists of an organogel. Post-deposition, the gel reservoir is chemically cross-linked via photo-polymerization to permanently cure the matrix. The fugitive ink is then removed thereby yielding the desired 3D microvascular network.
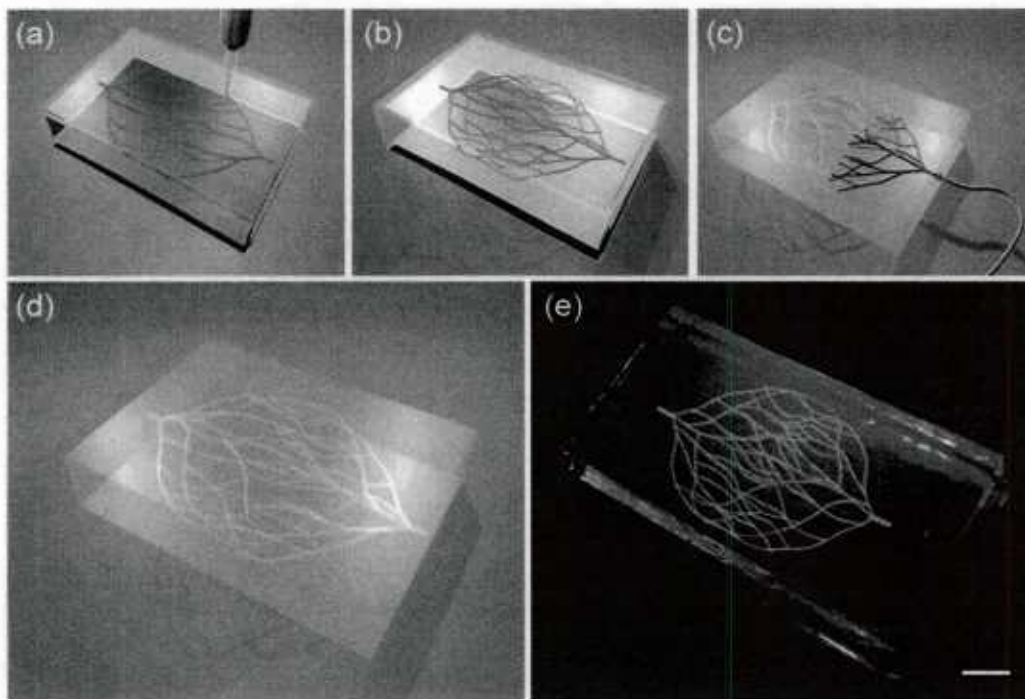
Figure 23. Omnidirectional printing of 3D microvascular networks in a photocurable hydrogel matrix. a) Deposition of a fugitive ink into a physical gel matrix allows the patterning of 3D interwoven filaments. b) Chemical cross-linking of the matrix via photopolymerization solidifies the matrix. c,d) The ink is liquefied upon cooling and removed under light vacuum exposing the microvascular channels. e) Fluorescence image of a Pluronic F127-diacrylate matrix containing red dyed ink. (scale bar = 10 mm).

We have developed two matrix chemistries suitable for ODP: one based on a hydrogel matrix and the other based on a photocurable epoxy matrix. We fabricated 3D biomimetic microvascular networks composed of 4-generation branching channels whose diameters range from 200-400 μm using both matrices (see Figure 23). The physical properties of the hydrogel matrix are similar to its unfunctionalized form, making it an ideal support medium for ODP. UV irradiation for several minutes is sufficient to fully crosslink a 50 mm thick block. By contrast, the opacity of the cured epoxy matrix limits its thickness to 10 mm. We are therefore exploring new pathways to forming transparent structural matrices.

We have created 3D microvascular networks with biomimetic architectures that obey Murray's law via ODP. To create 3D networks, a fugitive ink composed of 23% Pluronic F127 in water is printed into a photopolymerizable matrix composed of 25% Pluronic F127 diacrylate (Figure 23a). After the desired fugitive-ink filled microchannels are omnidirectionlly printed, the matrix is crosslinked with UV irradiation (Figure 23b). The fugitive ink is then removed from the structure leaving behind the desired 3D microvascular network embedded in a hydrogel matrix (Figure 23c,d). A fluorescent image of a printed and cured architecture is shown in Figure 23e (scale bar = 10 mm).

The microchannel diameters can be tuned by printing through a single nozzle and adjusting the extrusion pressure "on the fly" (Figure 24a). Using this approach, it is possible to vary the
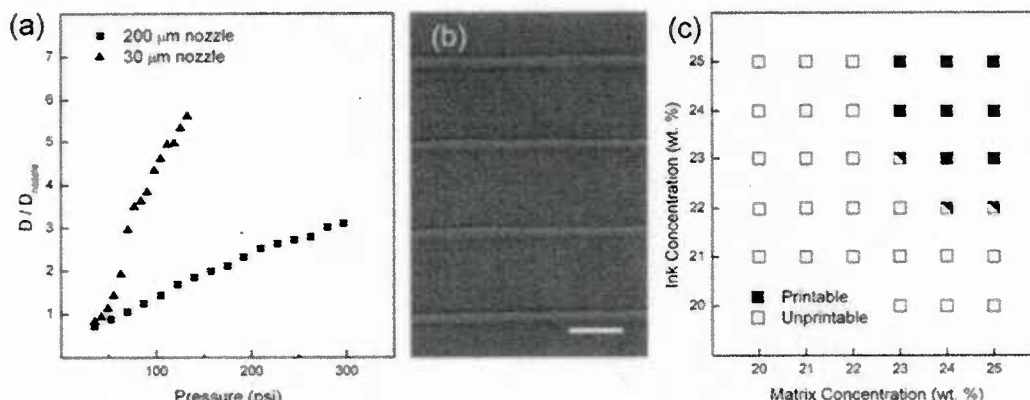
Figure 24. Printing parameter characterization. (a) Normalized channel diameter as a function of applied pressure during direct ink writing at 6 mm s⁻¹ using a (■) 200 µm stainless steel nozzle and a (▲) 30 µm tapered glass capillary. (b) Optical image of printed 18 µm channels (scale bar = 100 µm). (c) Printability map for ink and matrix combinations as a function of concentration.

microchannel size up to 3x higher than a 200 µm nozzle, and up to 6x for a 30 µm nozzle. The finest feature size that can be reliably achieved is 18 µm using a 10 µm tapered glass capillary (Figure 24b).

Developing an ink/matrix combination that enables omnidirectional printing requires careful control over both of their rheological properties. Figure 24c details the concentrations of ink and matrix that result in successful fabrication for the above system.

2.2.3 Interpenetrating microvascular networks

To extend the number healing cycles observed for microvacular-based self-healing composites we designed and fabricated interpenetrating microvascular networks that enable more robust healing as well as new healing chemistries to be explored. Two fugitive inks, wax- and pluronic-based, have been developed for DIW of interpenetrating microvascular networks, each of which can be evacuated from the network via a modest temperature change. We have specifically designed these inks such that the wax ink liquefies upon heating to ~ 60°C, whereas the pluronic ink liquefies upon cooling to ~ 4°C. A representative interpenetrating microvascular network embedded in epoxy is shown in Figure 25. The interpenetrating microchannels, which will
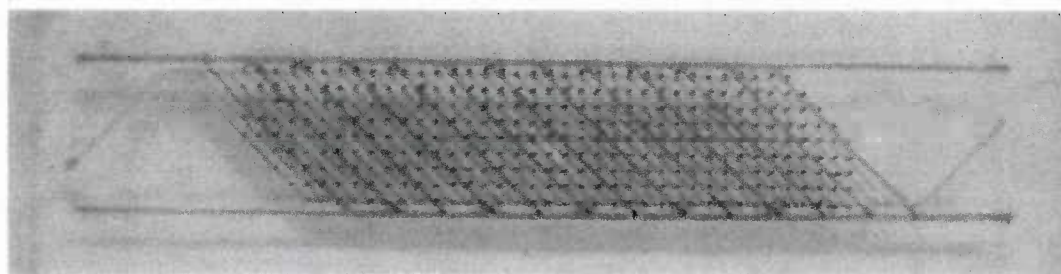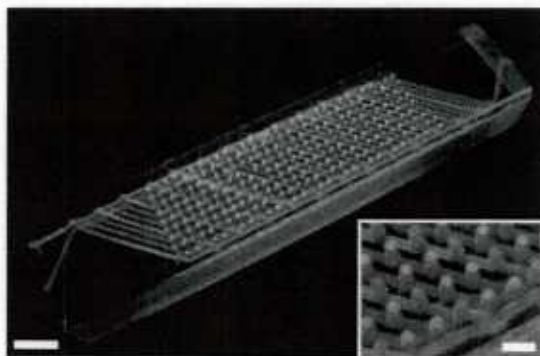

Figure 25. Interpenetrating microvascular network assembled by DIW, where both a wax ink (blue) and pluronic ink (red) are co-deposited.

ultimately contain the resin and hardener, are constructed by direct writing of the wax ink. To keep these two constituents separated until they reach the crack plane, each network is isolated by depositing a sacrificial layer composed of pluronic ink. After the matrix is fully cured, the pluronic ink is removed and the subsequent void space is then filled with an epoxy resin. Upon removal of the wax ink, the specimen contains two interpenetrating microvascular networks, each of which can be filled with different healing agents.

We have created the next generation of self healing materials with interpenetrating microvascular networks (IPN), which demonstrate repeated crack healing using a two-part epoxy system (Toohey 2008; Hansen 2009). Figure 26 shows an IPN structure patterned by direct-write assembly and infiltrated with a two-part epoxy, in which the resin (in blue) and hardener (in red) are contained within two independent microvascular networks.

We have investigated how healing agents flow and mix within crack(s) that develop in this coating/IPN microvascular substrate. We directly image fluid flow and mixing within the crack plane using fluorescent microscopy. Upon crack formation, model healing agents that consist of glycerol/water mixtures labeled with different fluorescent dyes, shown as red and green fluids in Figure 27, are wicked into the crack plane via capillary forces. When the two fluids mix, they produce a yellow color. Through image analysis, we can quantify the extent of fluid mixing for varying network designs (i.e., microchannel size and spacing), fluid viscosity, and, ultimately, reactivity.

We have also investigated accelerating microvascular healing by enhancing polymerization kinetics at elevated temperature (Kirkby et al. 2008). To achieve this goal, we introduced a third microvascular network dedicated to thermal modulation of the self-healing kinetics via a controlled-temperature fluid. This new microvascular network design brings local temperature control to the regions with the interpenetrating microvascular network, yet will not fracture during mechanical damage as it is embedded at a sufficient depth in the matrix material (see Figure 28). The fabricated interpenetrating three-network design, shown in Figure 28b, houses both the resin (blue) and hardener (red) in separate networks that are interwoven amongst the thermal-modulation network (green).

Figure 26. Interpenetrating micro-vascular network embedded within a polymer matrix (scale bar = 5 mm). Inset: Higher magnification view of vertical features (scale bar = 2 mm).
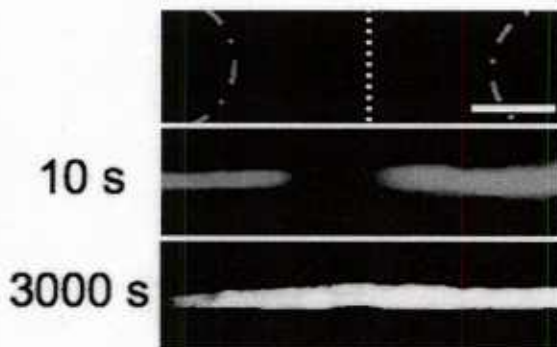
Figure 27. Model resin (red) and hardener (green) in the crack plane. Dotted line denotes the centerline between the two conduits. The separate fluids (10 s) mix after 1 hr. Scale bar 250 µm.
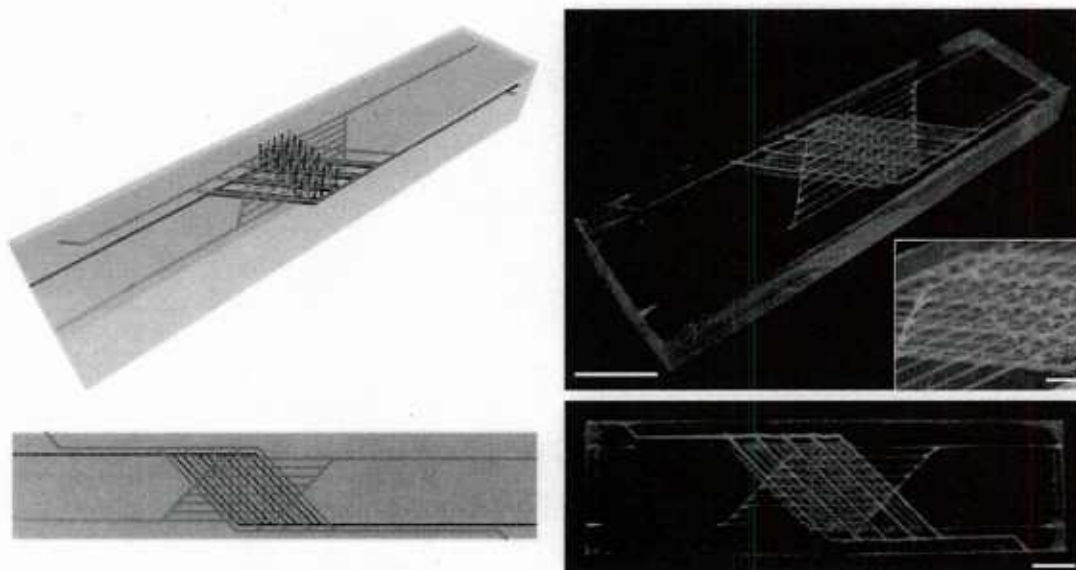
Figure 28. (a) Schematic illustrations (side and top views) of three-network design for integrated thermal modulation of polymerization kinetics. (b) Fabricated three-network design, where the epoxy resin (in blue) and hardener (in red) are interdigitated with the temperature modulation network (in green). Scale bars = 5 mm (Inset scale bar = 2 mm).

The polymerization kinetics of this healing system are highly sensitive to modest increases in temperature. The initial degree of polymerization can be accelerated by a factor of 20X when the epoxy reaction temperature is increased from 30°C to 70°C (see Figure 29a). Comparison of the elastic modulus for the original healing system at 30°C to elevated temperatures shows a similar decrease in reaction time, as shown in Figure 29b. The reacting epoxy system is elevated in 20°C increments and measured via dynamic mechanical analysis (DMA), with the final data normalized by the fully cured 30°C elastic modulus to account for the temperature-induced elastic modulus

(a)   (b)
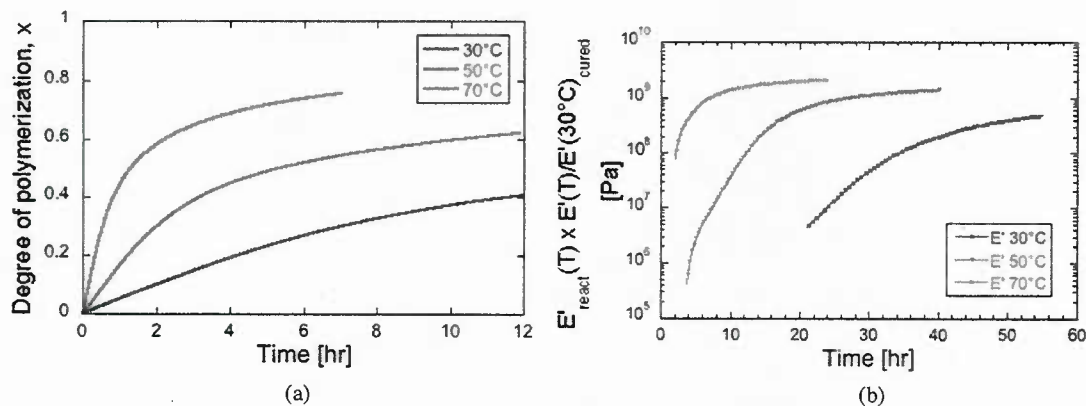
Figure 29. (a) Degree of polymerization of a stoichiometric mixture of the Epon 8132:Epikure 3046 healing system at reaction temperatures from 30°C to 70°C. The initial healing reaction kinetics accelerate by a factor of 20X over this temperature range. (b) Elastic component, E', of the viscoelastic modulus measured by dynamic mechanical analysis. E' data for 30°C at 48 hrs are matched by 70°C in only 3.5 hrs. Data are scaled by the fully cured E' to account for temperature effects.

decreases. This data demonstrates rapid acceleration in healing kinetics to achieve the same elastic modulus as for the original 30°C oven-cured system. Specifically, the elastic modulus measured at 30°C for the 48 hour healing cycle is matched at 70°C in only 3.5 hours, a theoretical reduction of healing time by a factor of 12.

These temperatures are achieved via embedding a third microvascular network. To validate local temperature increases, the thermal profiles are interrogated via infrared camera imaging. Water is circulated through the microvascular network at a constant temperature (30°C, 50°C, 70°C) and flow rate (5 mL/min). As shown in Figure 30a-c, the fluid locally elevates the
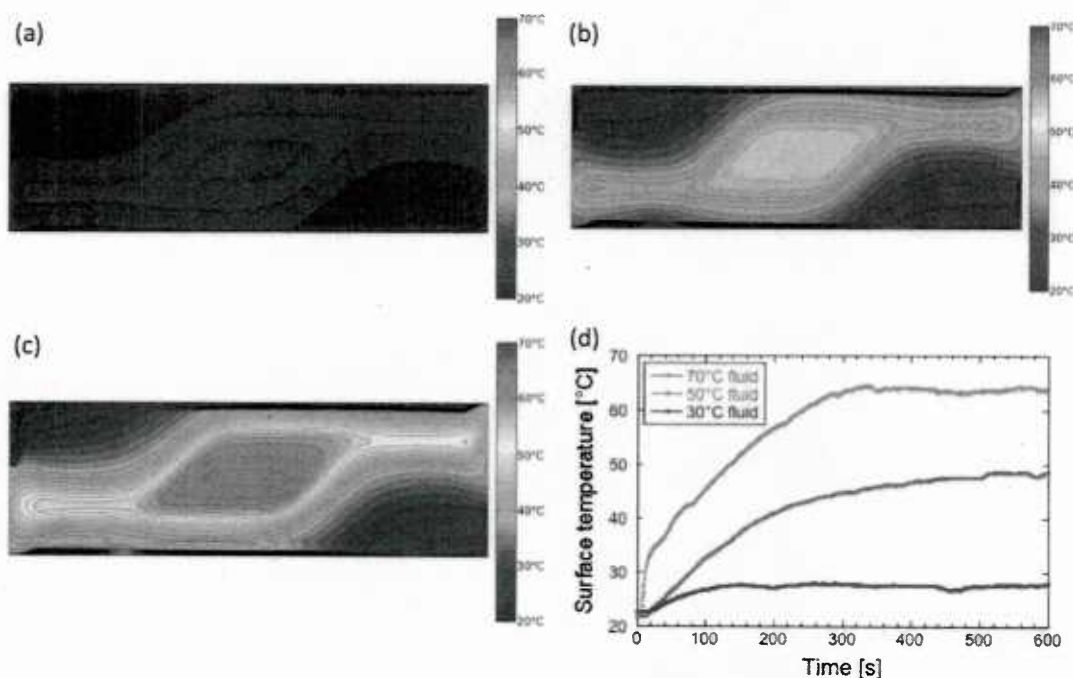
Figure 30. (a-c) Temperature distribution of the specimens viewed by infrared camera for circulating water temperatures of (a) 30°C, (b) 50°C, and (c) 70°C after 10 min. Surface area is 50 mm by 14 mm. (d) Specimen surface temperature over 10 minutes. Specimen surface temperature stabilizes in ~5 min.

temperature in the region of the microvascular network. The temperature increase is stable and easily controlled via the circulating fluid temperature.

Recently, the 3-network IPN structures have been tested in a 4-point bending geometry and then healed at 50°C via circulating heated water. Preliminary results indicate that the modest temperature increase has a dramatic influence on healing time, whereby healing is witnessed after heating times as short at 4 hours (~5 hours overall, when mechanical testing and cooling times are added); this experimental result is an order of magnitude reduction in required healing time. A heating time of 3 hours is insufficient to demonstrate healing; this is expected, due to a minimum gelation time of ~3.2 hours. However, a ~4 hour heating time for 3-network IPN specimens is sufficient to nearly match the average healing load for the previous 2-network IPN specimen in the original work. After additional heating time via circulating fluid, the 11 hour heating time demonstrates healing exceeding the maximum healing load recorded in previous IPN work (Hansen et al. 2009).

2.2.4 Vaporization of sacrificial components (VaSC) for 3D microvascular networks

Microvascular systems are essential to a broad range of technological applications, including biotechnology, microelectronics, sensors, chemical reactors, and autonomic materials. Inspiration for microvascular networks is drawn from nature, the mother of composite materials, applying microvascular technology to create skin, cartilages, tendons, bones and teeth. Cellulose fiber based composites, occurring in plants, provide the inspiration for networks that are intertwined with structural elements. We have developed a method for the creation of 3D woven composite materials containing microvascular networks via interweaving of sacrificial fibers. The polymeric fibers are removed by heating the cured composite above the cure temperature, catalyzing depolymerization of the fiber into a gaseous monomer. These fibers are woven directly into glass or carbon fiber composites and after their evacuation, a network of interconnected, micro-channels embedded within a fiber-reinforced structural composite is created. Composites formed with sacrificial fibers should facilitate thermal management in multi-layered systems, enable more sophisticated self-healing materials such as self-healing fiber-composites, and provide a test-bed for new self-healing chemistries.

Poly(lactic acid) (PLA) is a thermoplastic, commercially available as fibers, that spontaneously depolymerizes into gaseous lactide monomers at temperatures above 280 °C (Fan et al. 2004). The depolymerization temperature is lowered by the addition of a variety of metal catalysts (Figure 31). We infused commercial fibers with a tin oxalate (SnOx) catalyst building upon a procedure that allows the incorporation of exogenous chemicals into PLA polymer chains via a combination of trifluoroethanol (TFE) and water (Quirk et al. 2000). Catalyst treated fibers had a faster weight loss by static thermal gravimetric analysis (TGA) indicative of faster depolymerization and evaporation of the monomer. We have found a practical evacuation temperature for catalyst treated fibers in epoxy matrices to be 210 °C. Under these conditions, channels as long as 500 cm have been evacuated.
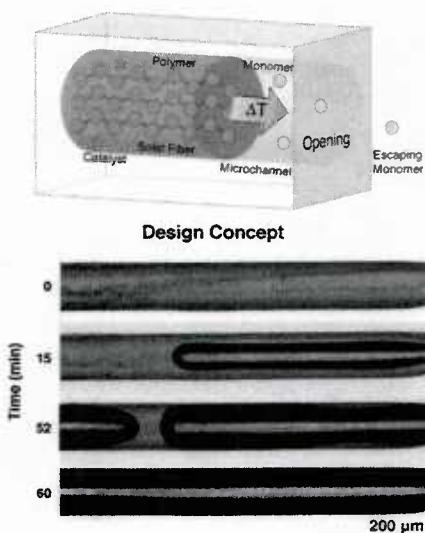

Figure 31. Schematic detailing the mechanism of channel creation. Optical microscopy images showing the process of fiber evacuation from a channel.

There are several requirements for constructing microvascular networks inside 3D composites; these include basic geometric constraints pertaining to the diameter and curvature of each channel, in addition to more advanced features such as interconnection of channels. The ability to fabricate microchannels over a range of size scales is critical to microvascular design as it dictates the pressure and volume of fluid as it flows through the network. Microchannels ranging in size from 20-500 μm have been created in epoxy matrices following fiber evacuation. Empty channels and openings were observed using optical and scanning electron microscopy (Figure 32a). Fibers of an increasing diameter require longer periods of catalyst infusion, up to 24 h, in order to achieve sufficient evacuation.

The effect of fiber curvature on evacuation was also examined by removing fiber samples wrapped around an internal 800 μm epoxy post to create a 180° bend in the microchannel. Fiber curvature appears to have minimal effect on the evacuation of the microchannel with both the straight and curved channels evacuating completely under identical conditions (Figure 32b).

Interconnects between microchannels are required to construct three dimensional microvascular networks out of sacrificial fibers. To create interconnects, overlapping fibers were cast in epoxy and evacuated under standard conditions. Analysis using microscale x-ray computed
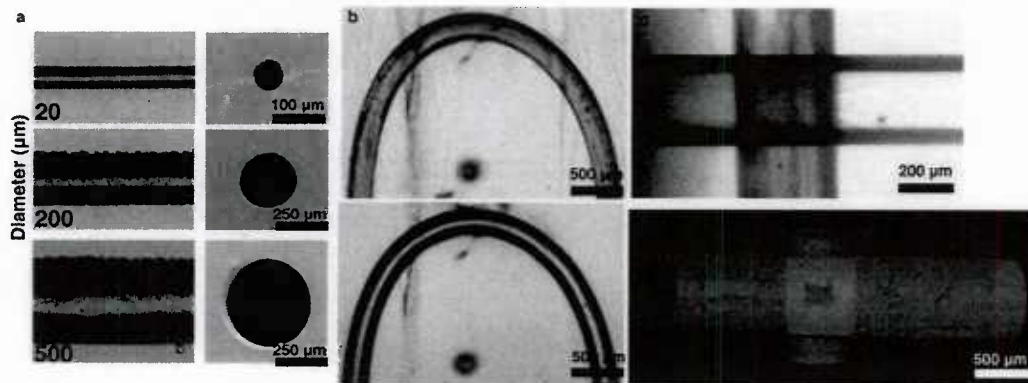
Figure 32. Functional capabilities of sacrificial fibers: a) Empty channels created from sacrificed fibers and open entry/exit ports ranging in size from 20-500 μm (b) Curved microchannel created by the evacuation of sacrificial PLA fiber, top image is before evacuation; c) Optical microscopy and X-ray tomography images of interconnections created by overlapping fibers.

tomography (μCT) reveal that an interconnection between channels is achieved at the point of contact between fibers (Figure 32c). For a 500 μm sacrificial fiber this interconnection was measured by μCT to be 180 μm in diameter.

Using a pre-existing 3D weaving machine (Bogdanovich et al. 2007), sacrificial and glass fibers were woven into a patented 3WEAVE (Bogdanovich et al. 2009), non-crimp orthogonal pattern. The 3D woven fiber preform consisted of 2 warp and 3 fill layers in which 4 central Z-tows were replaced with 500 μm diameter sacrificial fibers. These samples were infiltrated with epoxy using VARTM and cured. The sacrificial Z-fibers were then evacuated. The resulting, empty micro-channels were filled with functional liquids as a demonstration for the potential use of microvascular composites (Esser-Kahn et al. 2011).

The creation of three-dimensional microvascular fiber reinforced composites enables material systems with unparalleled complexity. The method outlined, uses commercially available materials and is readily adapted to construct microvascular networks within existing fiber-reinforced composite layups. Using this technique, materials can be synthesized to contain a spectrum of microvascular network types from simple, hand-made patterns to computer-controlled 3D weaving structures. 3D microvascular composite materials could have potential for autonomous self-healing and active-cooling. Large-scale, 3D microvascular networks are an enabling, platform technology for a wide array of future technological applications beyond composite materials

ranging from tissue patterning to gas exchange. Sacrificial fibers provide a vehicle to create biomimetic material systems capable of reproducing many of the functions found in nature.

2.2.5 Embedding pumps and valves in microvascular networks

We have investigated methods for integrating both pumping and valving structures within microvascular networks created by direct ink writing. Of the many pumping approaches reported to date, our approach focuses on pumps activated by externally rotating magnetic fields (Atencia et al. 2006, Rye et al. 2004). This approach is considered optimal as it overcomes limitations with fluid composition associated with electro-osmotic (Harrison et al. 1993) and electro-kinetic (Bousse et al. 2000) flow, and device failure associated with mechanically-intensive pumps.

Specifically, we integrated a micropump consisting of a magnetic stir bar (8 mm x 1.5 mm x 1.5 mm) within a circular fugitive ink cavity connected to a simple microvascular network (Figure 33). This micropump is capable of moving fluid volumes under magnetic field rotation rates of 60 to 1200 rpm. It is expected that the fluid flow rate will increase linearly with rotation speed.

(a)   (b)
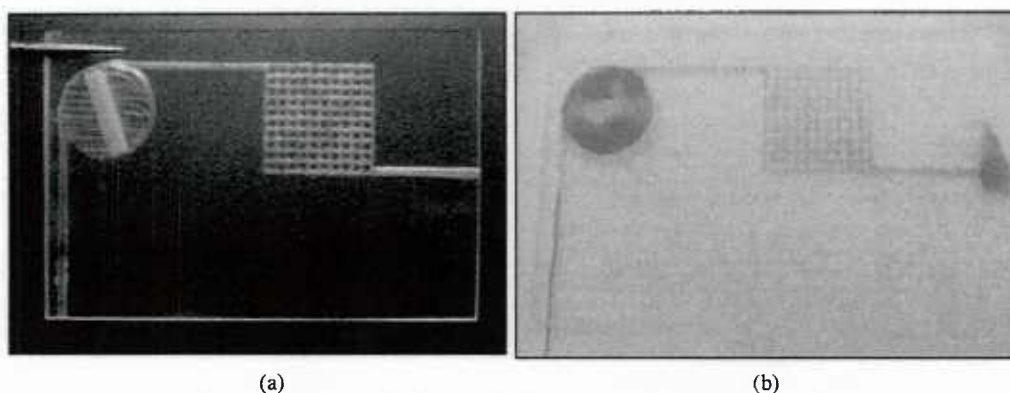
Figure 33. (a) Integrated pump connected to 10mm x 10mm x 4 layer network, and (b) operating pump, flowing dyed green liquid through the network.

Autonomous hydrogel valves are under investigated for integration into self-cooling microvascular systems. N-(isopropylacrylamide) (NIPAam) is a temperature-sensitive hydrogel with a transition temperature of 32°C in its pure form (Singh et al. 2006). Increasing the hydrogel temperature above 32°C induces significant shrinkage in sample dimensions. This has been previously exploited as a means to create temperature-sensitive valves in microfluidic devices (Beebe et al. 2000). The primary benefit of NIPAam is the combination of both its sensing and actuating functionality.

We created a hydrogel-based ink capable of being patterned by direct-write assembly. Polymerization proceeds by UV light, allowing experimental control
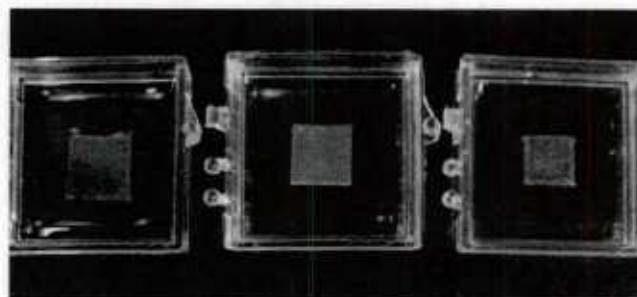
Figure 34. Temperature response of NIPAam hydrogel network fabricated by direct ink writing after immersion in water at 5°C and heating above its transition temperature.

over cure times. Preliminary hydrogel scaffolds were constructed (5 mm x 5 mm, 4-layers) that swell when immersed in water and deswell at elevated temperatures (see Figure 34). Ultimately, the valves will be deposited and cured in-situ, bypassing the extensive post-processing work associated with previous efforts related to hydrogel valves.

2.3 Theme III: Biomimetic and bioinspired designs

2.3.1 Simulation and characterization of self-healing hydrodynamics

Experimental observations suggest that the ring opening metathesis polymerization process used in the autonomic self-healing system is sensitive to parameters such as the amount and reactivity of the catalyst, the pressure of the healing agent, and the crack dimensions. In order to better understand the mechanisms at play and assist the design of better systems, a computational tool has been developed to simulation the hydrodynamics of the healing process. This simulation tool is capable of modeling the flow and solidification of healing agent in realistic crack geometries. Using this tool for a model crack, we have developed and demonstrated a procedure to construct "phase diagrams", which identify the regimes in which healing occurs for various ranges of system parameters.

Simulation Tool: There are three main phenomena that must be represented: flow of healing agent, its solidification, and advection-diffusion of the curing agent that drives the solidification. For the low flow Reynolds numbers expected in the self-healing system, the flow of healing agent is viscous, governed by the incompressible Stokes flow equations:

$$\nabla \cdot \mathbf{u} = 0, \quad (1) \qquad\qquad -\nabla p + \nabla \cdot (\mu \nabla \mathbf{u}) = 0 \quad (2)$$

where $\mathbf{u}(\mathbf{x},t)$ is the velocity, $p(\mathbf{x},t)$ is the pressure, and $\mu(\mathbf{x},t)$ is the viscosity, which changes locally in time as a function of the degree of cure. (We assume that the viscosity is changing slow enough not to violate the conditions for steady Stokes flow equations. This not a restrictive assumption.) For now, the model we have chosen for the change in viscosity

$$\frac{\partial \mu}{\partial t} = \mu_0 c e^{ct} \quad (3)$$

is based on the solidification of a general polymer melt (Roller 1975), but this can be easily refined as necessary for different materials based upon experimental observation of their behavior. Since the viscosity depends on history of a material element, the overall system we must solve is a partial differential equation whose coefficients are determined by solving an ordinary differential equation along fluid particle paths.

The Stokes equation is discretized and solved using standard Q2-Q1 finite elements (Silvester et al. 2005). To solve for the viscosity coefficient, we introduce Lagrangian particles that simply track material elements in the flow. For a given fluid particle with initial position $\mathbf{x}_i(0) = \mathbf{x}_i$, the viscosity is given by

$$\mu(\mathbf{x}_i(t),t) = F\left(\int_0^t \max(\phi(\mathbf{x}_i(\tau),\tau) - \phi_{\min}, 0) d\tau \right), \quad (4) \qquad\qquad F(t) = \mu_0 e^{ct} \quad (5)$$

The viscosity is then mapped onto the Q1 finite element mesh through a local average about each node.

The advection and diffusion of the catalyst $\phi(\mathbf{x},t)$ is governed by

$$\left(\frac{\partial\phi}{\partial t}\right) = -(\mathbf{u}\cdot\nabla)\phi + \nabla\cdot(D\nabla\phi) \qquad (6)$$

where the diffusion coefficient $D(\mathbf{x},t)$ is related to the viscosity through the Stokes-Einstein relation

$$D = \frac{kT}{6\pi\mu R} \qquad (7)$$

This equation is discretized and solved using Q2 finite elements in space and Crank-Nicolson time integration.

Results – Flow characteristics: Figures 35 and 36 show the flow patterns that develop when a channel is initialized with a 2D Gaussian distribution of catalyst and then subjected to a driving pressure force on the left inlet. This is a model configuration for a crack spanning between a microvascular network at some set pressure and the exterior of the material. At the outlet, the pressure field must match the normal derivative of the velocity field, thus giving a natural stress-free outflow boundary condition. A similar pressure driven flow in a more complex bend is shown in Figure 37 and 38.
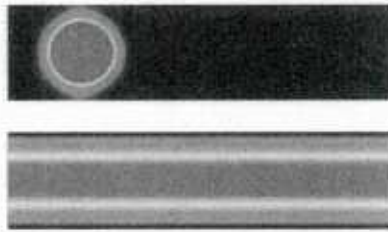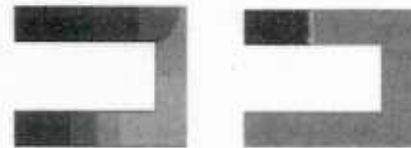

Figure 35. *The catalyst concentration (top) and total velocity (bottom) at t=0. The top and bottom boundaries are no-slip walls.*
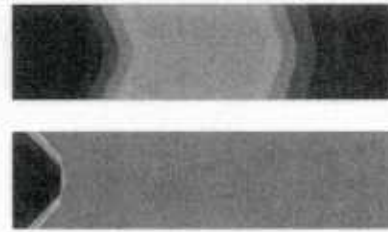
Figure 36. *The catalyst concentration (top) and viscosity (bottom) at 80% cure.*


Figure 37. *The catalyst concentration (left) and total velocity (right) at t=0.*

Figure 38. *The catalyst concentration (left) and viscosity (right) at 80% cure*

To assess the effect of a range of system parameters, the simulation code was driven with DAKOTA, a parallel optimization toolkit that enables a minimally invasive parameter search. The parameters investigated for the channel depicted above (Figures 35-36) include the driving pressure, the aspect ratio of the channel, the parameter c that controls the growth rate of the viscosity, and the Schmidt number that relates the viscosity and the diffusivity. We see in Figure 39 that a range of behaviors can be found. For higher Schmidt numbers (less diffusive relative to viscous), there are two regions with low healing: at low pressures the catalyst diffuses away before significant solidification can occur and at higher pressures it is advected out of the crack before significant solidification can occur. For the parameters investigated, healing is more successful for lower Schmidt numbers and higher rate constants for solidification. Work is on going to match the specific parameters for the materials currently being used in the healing systems under development.
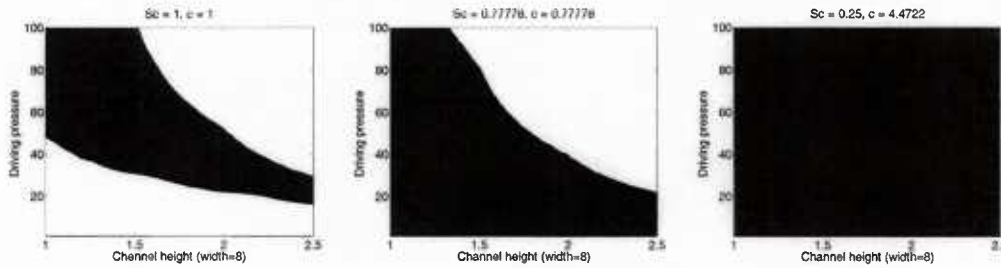
Figure 39. *Three characteristic phase diagrams (black indicates > 80% cure). In the first, the diffusion through the inlet prevents healing in low driving pressure. In the first and the second, high driving pressure washes the curing agent out of the crack before healing can occur. In the third, healing occurs in the entire region.*

2.3.2 Simulation and characterization of self-healing capillary flow

Experimental diagnostics are challenging on the scales of current and proposed microvascular composites. In order to better understand the mechanisms important for self-healing and other functions, we have developed a simulation tool for modeling the capillary action that is thought to draw healing agent from the microvasculature into a crack, its mixing with dissolved catalyst or another fluid in the crack plane, and the subsequent hardening (polymerization) that occurs. The code has models for both the Grubbs catalyst system originally considered, as well as the two-part epoxy systems being studied more recently.

Simulation Tool: The flow in the microvasculature and cracks is low Reynolds number and is thus in the Stokes limit of the flow equations. The polymerization is coupled into the Stokes equations via an increasing viscosity, whose kinetics are modeled as

$$\mu(X, t) = \mu_o e^{c\tau}, \qquad (8)$$

where τ is a measure of the time in contact with catalyst. A Eulerian perspective of this offers a more natural inclusion into the overall flow solver:

$$\frac{D\mu}{Dt} = \tilde{c}\mu \qquad (9)$$

where $\frac{D(\cdot)}{Dt}$ is the material derivative and $\tilde{c}$ is a reaction rate coefficient. We define a minimum catalyst concentration, below which polymerization does not occur. This is incorporated into $\tilde{c}$

as $\tilde{c} = \mu_o c H(\phi - \phi_{\min})$, where H is the Heaviside function and ϕ is the catalyst concentration.

The full system of equations, which includes the equations for Stokes flow, advection-diffusion, and the viscosity equation, are solved using finite elements. The extension of the above model to a two-part epoxy system has been achieved through a modification of the viscosity equation. If we define $\phi = 1$ as fluid 1 (for example, the resin) and $\phi = 0$ as fluid 2 (for example, the hardener), we can solve the advection-diffusion equation in the same manner as with the catalyzed system. The reaction term in the viscosity equation is changed so that when equal parts of fluid 1 and fluid 2 are present ($\phi = 0.5$), the reaction proceeds at maximum speed. Thus we redefine $\tilde{c}$ as $\tilde{c} = 4\phi(1 - \phi)\mu_o c H(\phi - \phi_{\min})H(\phi_{\max} - \phi)$.

A so-called *phase field* model is used to incorporate capillary forces into the simulation model. In this approach, the phase ψ is advected as a passive scalar. In regions of liquid $\psi = 1$ and in regions of gas $\psi = 0$. Where $\nabla\psi \neq 0$, a force is added to the equations to represent the action of surface tension. In standard continuum models, this would be a singular force; in our discrete representation it is a smoothed analog of a δ function. The magnitude of this force is be designed so that its net effect exactly matches that from a singular surface tension of appropriate strength. Figure 40 shows a meniscus drawing liquid into a model crack geometry.

Figure 40. A meniscus drawing fluid into a model crack. The liquid has phase $\psi = 1$ (red) and the gas has phase $\psi=0$ (blue). The interface shown with the black curve is $\psi = 0.5$.

A novel explicit-implicit scheme has been developed for integrating the system in time. Ordinarily, an implicit scheme is used for the diffusive term in advection-diffusion equations because of the severe time-step restriction this term imposes. However, this would be a challenging approach in our situation where the diffusivity is nonlinearly coupled with the flow and kinetics models. To overcome this, and facilitate reasonably long time steps, we split the diffusivity into a base state that is linear plus a nonlinear component that is $O(\Delta x)$. The linear portion is solved with a standard implicit method. The $O(\Delta x)$ of the nonlinear term removes the excessive time-step restriction that would be incurred in solving this part easily and efficiently with an explicit scheme.

Simulation Results: We have demonstrated the simulation tool in a series of model self-healing flows. Figure 41 shows a schematic of a crack with a dot of catalyst and Figure 42 shows the percentage of the fluid reaching its maximum viscosity after a long time. It is clear that the "good heal" region is a fairly narrow "ridge" in this parameter space, which illustrates the type of sensitivities that can exist in self-healing systems of this design. Figure 43 shows a system which models recent experimental designs that employ dual networks with the one component of two-part epoxies in each network. Here a design where the pressure is oscillated in the two networks shows near-perfect healing of the crack plane, but a corresponding case were both microvascular networks are at a common raised pressure washes out the components before they solidify leading to incomplete healing.
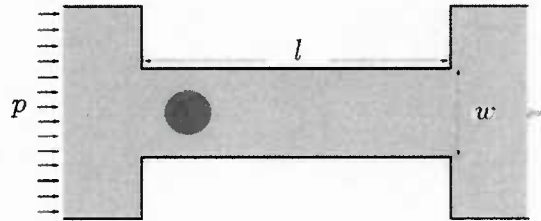
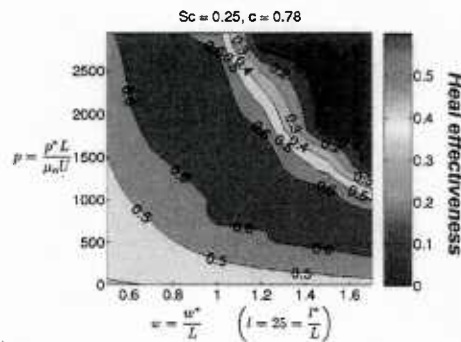***Figure 41.*** *Schematic of model catalyst/channel healing system.*

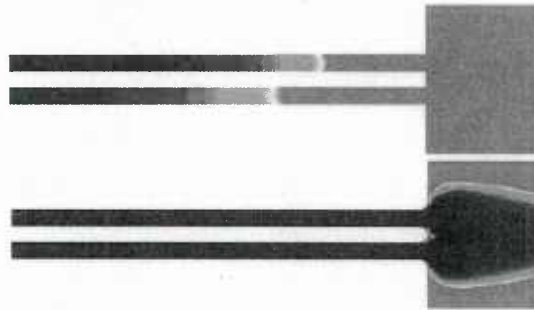***Figure 42.*** *Healing effectiveness versus "crack" width and plenum pressure.*

Figure 43. *Two-component healing system showing long-time solidification (red: max solidification, blue: liquid).* **Top:** *Opposite phase oscillating pressure in networks,* **Bottom:** *Positive pressure in both networks.*

2.3.3 Simulation of mixing in two-component self-healing systems

Efficient mixing is the key to repeated two-part self-healing in microvascular autonomic composites. We have developed a simulation tool based on the phase-field method that is capable of modeling mixing and healing in two and three dimensions. The extension to three dimensions necessitated improvements in the numerical methods to reduce the computational complexity to manageable levels. By taking advantage of the hierarchical structure of the finite element shape functions, we have reduced the runtime of our simulation code by up to

95% in relevant geometries. We conducted several mixing studies in sample geometries which demonstrate the possibility of mixing driven by sinusoidal pumping.

Numerical Advances: Automatically adaptive increases in polynomial order have been implemented to resolve the steep gradients in the flow and phase fields, which is particularly important near free surfaces and liquid-liquid interfaces. Our implementation uses arbitrary polynomial order finite elements based on hierarchical shape functions (Szabó and Babuska, 2001). Phase-field descriptions of multiple phases, such as we use, represent the liquid-gas interface as a continuous change in parameters over a finite distance. This distance must be small enough for the flow to be effectively independent of it. We have implemented so-called sharpening terms to maintain the thinness of this boundary in the continuum phase-field model.

Modeling the different features of this flow presents unique challenges. For small capillary numbers, surface tension causes a steep pressure gradient in the pressure solution. However, pressure only appears in the solution to enforce the divergence-free condition. Even though surface tension has an effect on the flow, the velocity fields are smooth in the case of Stokes flow. Therefore if we solve the system using Taylor-Hood type finite elements, we must increase the numerical resolution to capture the pressure solution even though the velocity solution requires much less resolution. Since the Stokes equation is the most computationally challenging equation to solve, this dominates the cost of modeling self-healing flow.

To reduce the cost associated with small-capillary-number flows, we have developed a numerical method that decomposes the pressure into two parts: one part corresponds to the "steep" part of the surface tension body force, and one part corresponds to the remaining smooth pressure. The body force from the momentum equation is decomposed into a divergence-free part and a steep part:

$$\mathbf{F} = \mathbf{F}' + \nabla\phi \qquad (10)$$

We then re-write the momentum equation as

$$-\nabla(p + \phi) + \nabla \cdot \left[\mu(\nabla\mathbf{u} + \nabla\mathbf{u}^T)\right] = \mathbf{F}', \qquad (11)$$

where the pressure $(p + \phi)$ which results from the divergence-free body force is smooth. We can solve for the steep part of pressure using a Poisson equation:

$$\nabla^2\phi = \nabla \cdot \mathbf{F} \qquad (12)$$

This equation requires higher numerical resolution to capture the steep gradient, but this is acceptable because it is easier to iteratively solve its discrete form than the full Stokes equation with high resolution. The hierarchical structure of the shape functions allows us to easily maintain and interpolate between solutions of different polynomial orders, and so we can solve the full Stokes equation with a lower polynomial order. Since the modified pressure is smooth, solving with less expensive low polynomial order is sufficient to maintain high accuracy.

Another challenge associated with multi-phase modeling using the phase-field method is maintaining a fixed interfacial width in the presence of velocity gradients across the interface, which is a feature of flow fields resulting from surface tension. To counter this unwanted diffusion, we use a correction term in the phase-field advection equation that forces the solution to a hyperbolic tangent profile (Sun et al, 2007). It is based on the kernel function

$$\psi_o = \frac{1 + \tanh\left(\frac{n}{2W}\right)}{2}, \qquad (13)$$

where n is the distance to the interface and W is the interface width. By substituting this kernel into the equation for curvature we get

$$\kappa_o = -\frac{1}{|\nabla\psi|}\left[\nabla^2\psi + \frac{4\psi(2\psi - 1)(\psi - 1)}{4W^2}\right] \qquad (14)$$

We use this to force the phase-field solution to the kernel function by adding a weighted difference of this with the computed curvature to the phase-field advection equation:

$$\frac{D\psi}{Dt} = b(\kappa_o|\nabla\psi| - \kappa|\nabla\psi|)$$
$$= b\left(-\nabla^2\psi - \frac{\psi(2\psi - 1)(\psi - 1)}{W^2} - \kappa|\nabla\psi|\right) \qquad (15)$$

This has the effect of adding a small amount of corrective numerical diffusion (determined by the numerical parameter b) precisely to the parts of the solution which deviate from the desired interfacial profile. Therefore, any field advected by this equation will be forced to a hyperbolic tangent profile. The parameter b determines how quickly the phase-field will reach this profile.

Experiments: Simulations of the advection-diffusion equation governing the mixing can provide a measure of molecular diffusion as it takes place, but this information is of little use without an understanding of what degree of mixing leads to what degree of curing. This motivated experiments that were performed to determine how curing of the Epon 8132/EPIKURE 3046 two-part system depends upon the stoichiometry of the eventual, partially mixed state. The optimal stoichiometry for this system is 2.27:1 (resin:hardener). After four days, specimens with less than 1:1 or greater than 4.5:1 ratios were found to be uncured, which establishes bounds on the range of mixing that must be obtained for healing to occur.

As the systems cure, the viscosity increases significantly and under some circumstances this in turn may affect filling of the crack plane. The model currently used in the simulations has an exponential rise in viscosity with time, $\mu(t) = \mu_o e^{ct}$. Using a TA AR series parallel plate rheometer, the rate parameter c was determined for the optimal stoichiometry to be $c = 2.6 * 10^{-4}$ s^{-1} (Figure 44). This model was shown to hold for about 10 hours, much longer than the time scale of mixing in the crack plane. Additionally, the rate parameter c was found to have a linear relationship to the stoichiometry in the ranges where curing occurs allowing parameterization of the effect curing over the entire range of parameters.

Figure 44. Viscosity as curing occurs for optimal stoichiometry.

Diagnostic Simulations: Diagnostics during healing are challenging, but post-healing examination of the healed crack suggests incomplete solidification in the crack plane. This is suggestive of a mixing limited process. To better understand the mechanisms leading to this we have conducted a set of diagnostic simulations in geometries that model recent experimental efforts by the group. One such model geometry is shown in Figure 45. The first of these simulations is a pre-wet crack (Figure 46). The crack is open and assumed to be initially wet with hardener. Then a pressure drives resin and more hardener into the crack plane. Under the resulting steady laminar flow conditions the mixing is limited entirely by the molecular diffusivity. For the realistically low diffusion shown, curing will only occur at some point in the crack in between the two channels. Three-dimensional simulation will be able to tie these conclusions more closely with experiments.

The next case demonstrates the possibilities that an air bubble might be trapped in the crack (Figure 47). If the resin and hardener fill the crack plane at the same rate, surface
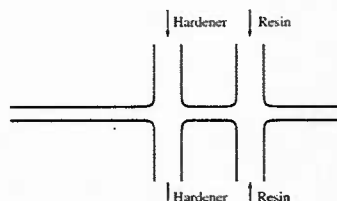
*Figure 45. Resin and hardener are pumped into the crack plane from opposing channels.*
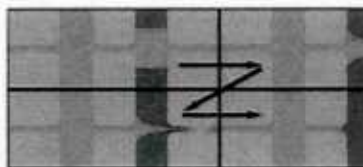
Figure 46. A crack opening between opposing channels. Red indicates hardener, blue indicates resin, and green indicates the target stoichiometric ratio for healing. The crack is pre-wet with hardener. Incomplete mixing will lead to incomplete curing and incomplete healing.
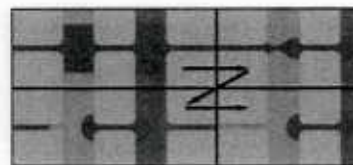
Figure 47: A crack opening between opposing channels. Red indicates hardener, blue indicates resin, and grey indicates air. An air bubble is trapped in the crack plane, preventing the two components from mixing.

tension forces prevent wetting of the crack in between the channels, leaving an air bubble. In this case no healing would occur, as the two components cannot mix. This is, of course, an idealized symmetric configuration. Further simulations will investigate the effect of more realistic (asymmetric) configurations in three space dimensions.

Mixing simulations: The concept of sinusoidal pumping to promote mixing in microchannels was explored by Glasgow et al. in 2003. They compared simulations of mixing water in a T-junction using sinusoidal pumping to experiments using dyed water and found that effective mixing was possible. We verified their mixing result, and extended it to the parameters of the self-healing system. In Figure 48, we compare our result to the simulation result in the Glasgow paper for water. Our simulation is more accurate as a result of using a conservative, higher order method, and so captures the interface deformation more accurately. In Figure 49, we apply the sinusoidal pumping to the fluids used in microvascular self healing, EPON Resin 8132 and EPIKURE Curing Agent 3046. Because we desire a stoichiometric ratio of 2.23:1, we change the amplitude of the pumping wave by multiplying the resin wave by 2.23.
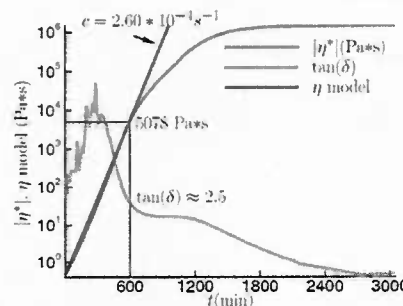
However, this results in a 1:1 ratio on the outflow, which would result in poor healing. In Figure 50, we have modified the flow so that the optimal stoichiometric ratio is obtained on the outflow. Figure 51 compares the result from 2D to the result in 3D.


Figure 48. On the left is the Glasgow result, on the right is our result. Our simulation captures the interfacial deformation more accurately. Geometry differences are due to image scaling in their paper.
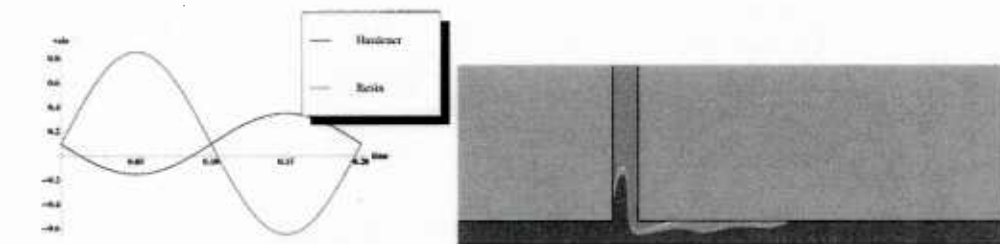
Figure 49. The result for EPON Resin 8132/EPIKURE Curing Agent 3046. The amplitude of the pumping is modified to match ideal stoichiometry. Ideal 2.23:1 resin:hardener stoichiometry is indicated by green.
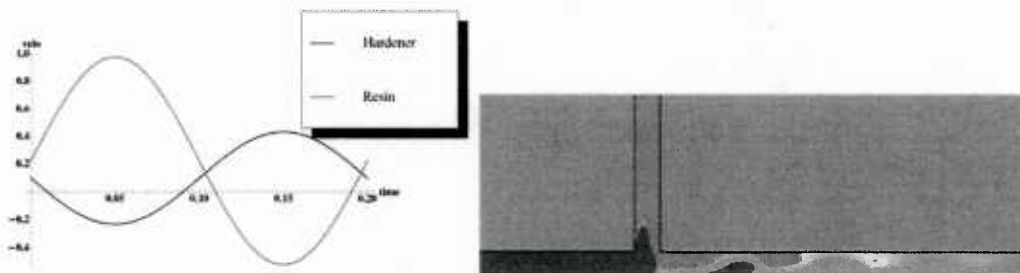
Figure 50. The result for EPON Resin 8132/EPIKURE Curing Agent 3046. The pumping is modified to result in stoichiometric ratio on the outflow. Ideal 2.23:1 resin:hardener stoichiometry is indicated by green.
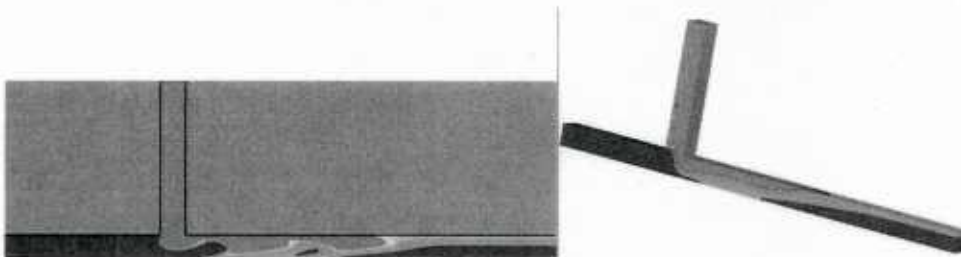

Figure 51. 3D simulation shows similar results to the 2D simulation.

Chaotic Advection Simulations: In the viscous flows of healing components into the crack plane, the primary mechanism for mixing is diffusion only, which is slow. If significant solidification occurs before mixing is complete, we expect incomplete healing. To speed mixing a stirring of sorts must occur. However, the linearity of the viscous flow equations

precludes this unless unsteadiness or nonlinearity is introduced via the boundary conditions. Done the right way, this can lead to stirring which greatly deforms the interface between the two parts of the healing system and promotes mixing at the molecular needed for curing. This is known as chaotic advection and can be described formally in terms of the theory dynamical systems. Chaotic advection was demonstrated in microchannels manufatured via a direct write process by Therriault et al. (2003).

A preliminary simulation designed to induce chaotic mixing is shown in Figure 52. Resin and hardener are pumped onto the surface through separate microchannels. In this case, the geometric nonlinearity of the free surface is hoped to facilitate a switchover to chaotic advection. Initially, the resin and hardener bubbles coalesce into a single drop. The pressures in the two channels are then oscillated. The result of and initial simulations is shown in Figure 53. Chaotic advection has not yet been quantified, but these simulations are ongoing.
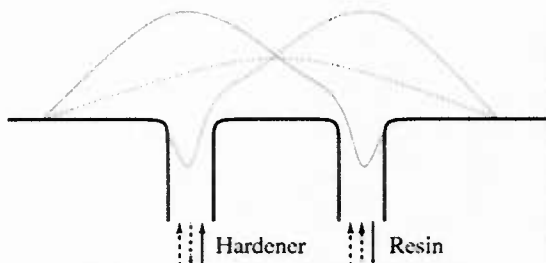
Figure 52. Resin and hardener are pumped onto the surface, followed by pressure oscillations.
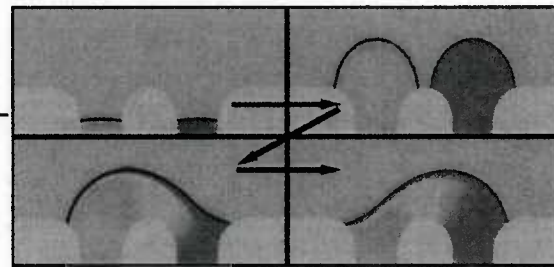
Figure 53. Oscillating pressure deforms the free surface in an attempt to promote chaotic mixing.

## 2.3.4 Computational design of microvascular networks

Genetic Algorithm Based Design: We have developed, implemented and applied optimization schemes based on genetic algorithms (GA) to optimize the design of embedded microvascular networks. This problem is quite complex both in terms of the number and diversity of objective functions (void volume fraction, impact on material stiffness and strength, network coverage, flow efficiency,...), constraints (manufacturability, domain shape and dimensions, ...) and design variables (network shape, micro-channel diameters, ...). Since gradient-based optimization schemes are unable to tackle such the complex and discrete nature of the design problem, we have adopted a GA-based approach that relies on the fundamental concept of "natural selection" between a large number of randomly chosen possible network configurations.

Two key computational tools have been developed. The first consists of a robust and flexible GA optimization library for multi-objective function problems. The GA optimization scheme adopted in this work is the Nondominated Sorting Genetic Algorithm (NSGA-II) that has shown great success in a variety of multi-objective function problems (Srinivas et al. 1995; Deb et al., 2002). The NSGA-II approach allows for the efficient extraction of the Pareto front, which regroups the optimal designs in the objective function space. The second tool is the general network generation and evaluation scheme that allows for the efficient treatment of a wide variety of microvascular networks ranging from simple rectangular domains to complex convex and non-convex geometries with and without holes, from simple single-diameter networks discretized with uniform grids to multi-diameter networks created by randomly distributed seed points linked by Delaunay triangulation or Dijkstra algorithm.

μVAC a new paradigm in materials design

The computational optimization tool has then been applied to a variety of 2-D network design problems. An example of this study can be found in Figure 54, which presents the initial randomly created cloud of population members and the Pareto optimal front for the problem of a square domain discretized by a uniform grid, with the inflow located at the bottom left corner of the domain and the outflow at the top right corner. Two objective functions have been considered in this study: (i) the void volume fraction introduced by the network in the domain, i.e., the ratio of the projected area of the network by the total area of the domain, and (ii) the "hydraulic efficiency" of the network, i.e., the pressure drop between the inflow and outflow locations. This pressure drop is computed by assuming Poiseuille flow in every network component and solving for a linear system describing the pressure value at every vertex in the network. In the study summarized in Figures 54 and 55, three diameter values were considered for the network: 0 (i.e., absence of the network segment), 100 and 200 microns, and full coverage was assumed (i.e., every vertex defining the network grid was activated). As apparent in Figure 55, which presents four characteristic networks labeled (a) to (d) in Figure 54, the optimization scheme is able to capture the tendency of the network to create a "larger vein" between the inflow and outflow location, resulting in a sharp drop in the computed pressure drop apparent in Figure 54.

More complex domains can also be considered, as illustrated in Figure 56, which presents microvascular networks defined on a non-convex domain shaped as a sugar maple leaf (Figure 56a) and on a rectangular domain containing a hole (Figure 56b). Current emphasis is placed on the design of 3-D network and on the parallel implementation of the optimization code for increased efficiency.
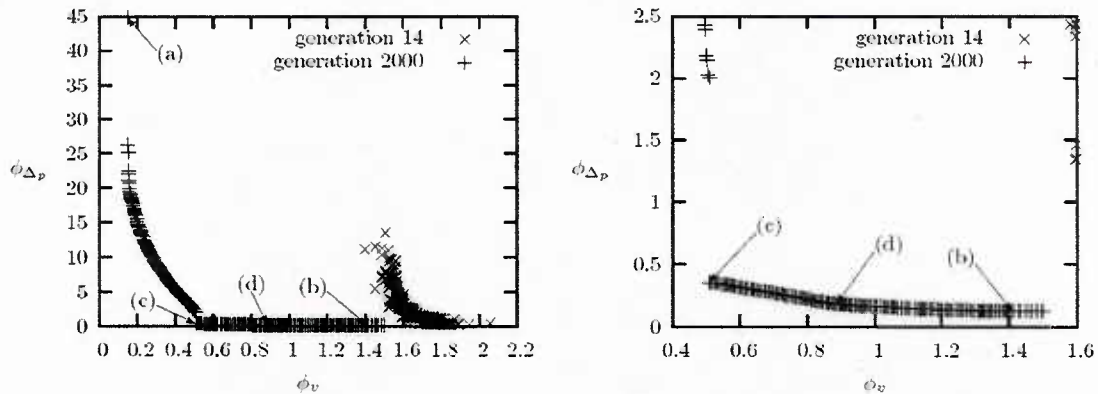

Figure 54. Pareto fronts after 14 and 2000 generations for a square network design problem. The x- and y- axes respectively denote the volume fraction and pressure drop objective functions, both of which need to be minimized.

Figure 55. Four networks sampled among the final Pareto front shown in Figure 1 and labeled (a) to (d). The inflow and outflow locations are at the bottom left and top right corners of the domain, respectively.

Figure 56. Microvascular networks defined on more complex 2-D domains.

Numerical Advances: A detailed survey on the use of the Non-dominated Sorting Genetic Algorithm (NSGA-II) for the optimization of microvascular networks has been published (Aragón A. M. et al. *in press*). The originally developed algorithm (Deb K. et al. 2002) is part of a broader family of algorithms designated Multi-objective Genetic Algorithms (MOGA). The study presented in Aragón et al. focuses on the optimization of microvascular networks subjected to a set of objective functions and constraints that define the embedded microvascular networks. These objective and constraint functions include the void volume fraction associated with the embedded microvascular network, the flow efficiency of the circulating healing/cooling fluid, the network coverage and reliability.

The clear division between objective function and constraint spaces ensures that unfeasible individuals disappear completely after a few generations, as shown in Figure 57 for
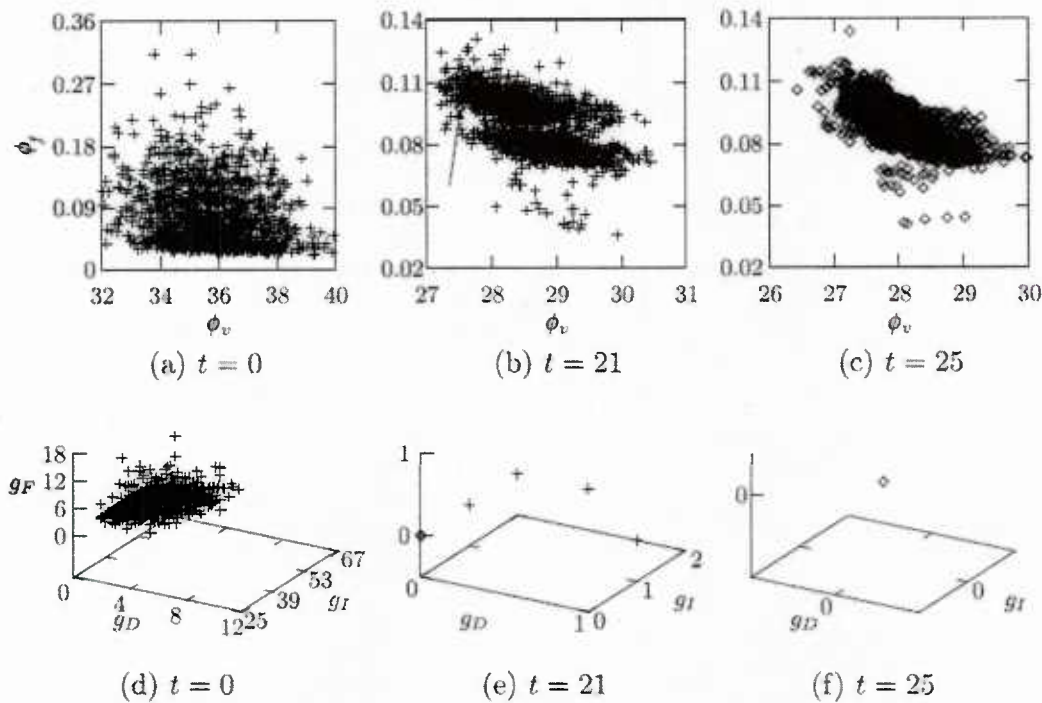
Figure 57. Objective function and constraint spaces at three early optimization steps. Plots on the upper row show the objective function space composed of void volume fraction and flow efficiency. Plots on the lower row show the constraint function space, composed of degree constraint, intersection constraint and flow constraint. Crosses (+) and diamond (◊) symbols indicate unfeasible and feasible individuals, respectively.

a typical optimization. No unfeasible individuals appear after this point so the optimization is carried only on objective function space.

The optimization scheme has proven to work equally well for both 2D and 3D networks, since the underlying Pareto-optimization mechanism is independent of the template structure chosen as a starting point for the process. Furthermore, the objective functions and constraints are mathematically simple and there is no limit on how many can be involved in the optimization process.

Generalized Finite Element Method (GFEM): With this powerful and flexible optimization tool at hand, we decided to investigate the multi-physics network design problem associated with microvascular self-healing materials. For this class of material, a new set of objective functions and constraints need to be introduced to characterize the "thermal efficiency" of the embedded network. Examples include minimizing (or constraining) the maximum temperature in the material, minimizing the thermal gradients (since these generate thermally-induced stresses), … To solve for the temperature field, the Generalized Finite Element Method (GFEM) has been adopted since it allows to separate completely the network topology from the underlying finite element mesh used to obtain the temperature solution, as shown in Figure 58 for a 4th generation branching structure.
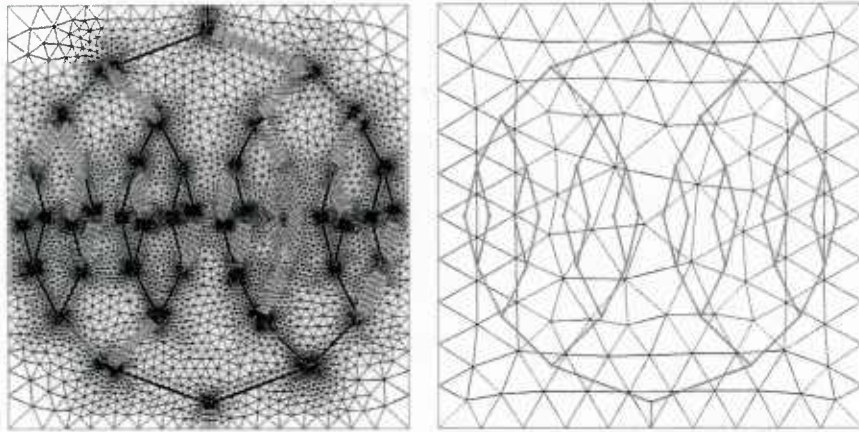

**Figure 58.** *Standard FEM mesh (left) and GFEM mesh (right).*

Thermal optimization was accomplished in the context of the Generalized Finite Element Method (GFEM) by developing a formulation that takes into account the discontinuous gradient nature of the temperature field along microchannels. The GFEM enrichment functions were integrated into an efficient finite element code. Figure 59 shows the resulting temperature field corresponding to the microvascular network depicted in Figure 58 without (left) and with the cooling fluid (right), with a finite element mesh for which the element edges do not follow the microchannels. A manuscript summarizing the proposed enrichment functions, together with a detailed convergence study and some related application problems, has been published as well (Aragon et al. 2010].

The GFEM solution of the heat equation is then considered as one of the objective functions to create a truly multi-physics optimization tool. The example shown below illustrates a three-objective optimization that starts with a network template configuration consisting only of horizontal and vertical microchannels. The three objective functions considered during the optimization are: *a)* minimizing the void volume fraction of the network; *b)* maximizing the flow efficiency by minimizing the maximum pressure drop between inflow and outflow locations; and *c)* minimizing the maximum temperature due to the presence of two localized heat sources. A total mass inflow rate of 5 g/min of water is used, with inlet temperature $T_I = 283.15$ K. For the temperature boundary value problem, all four edges of the domain are considered as convective boundaries, with ambient temperature $T_\infty =$
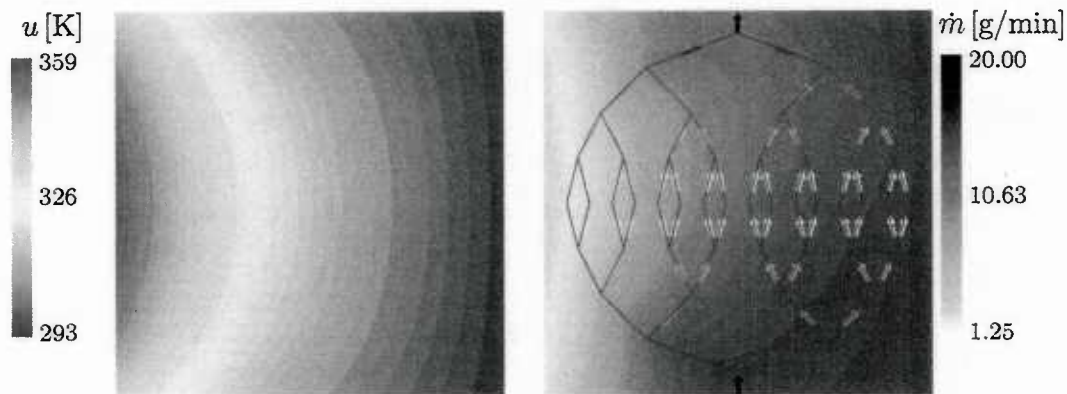
Figure 59. Temperature solution in the absence of flow (left) and considering a mass flow rate of 20.0 g/min (right).

293.15 K. The optimization then assi gns diameters to each one of the 1241 microchannels from the diameter set D [mm] = {0, 100} in order to minimize the three objective functions simultaneously. Figure 60 s hows the template microvascular network used (in black), superimposed to the solution of the heat equation in the absence of flow.
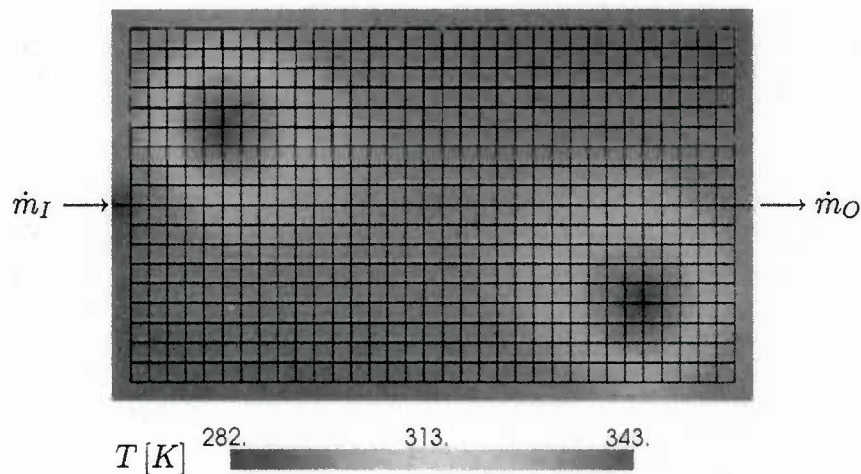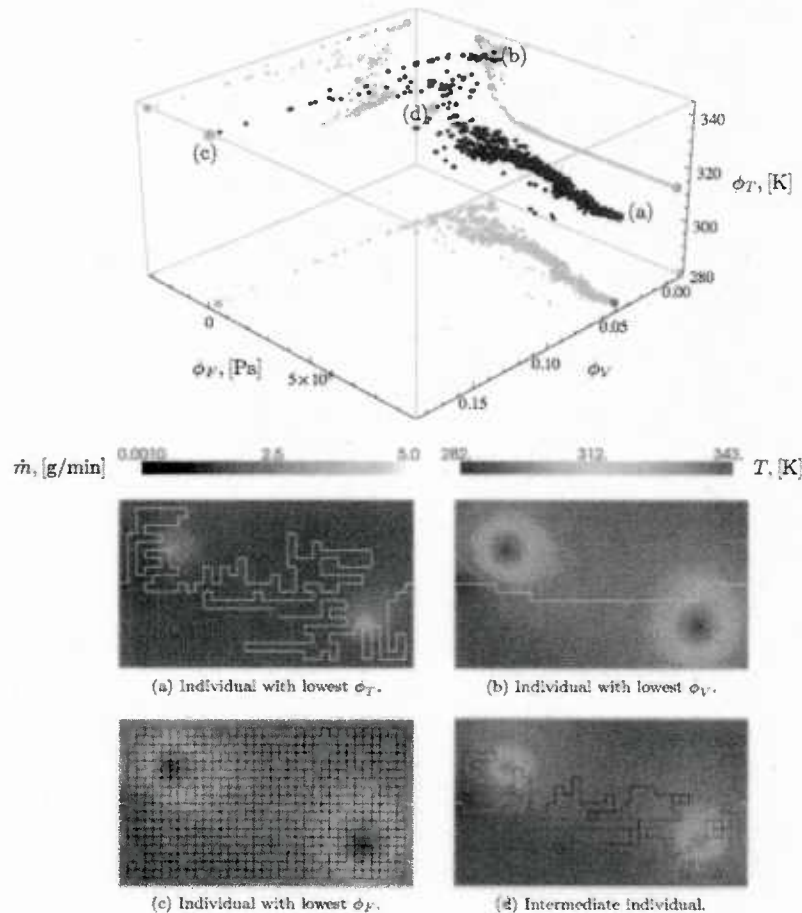

Figure 60. Microvascular network template (in black) with 1241 microchannels, showing inflow and outflow locations. The network is superimposed to the temperature field in the absence of flow.

Figure 61 illustrates the Pareto-optimal front resulting from the optimization after 40,000 generations and shows that the projection of the front on the $\{f_F, f_T\}$ plane is very well defined with a large range of individuals for which the minimum temperature remains almost constant. Some individuals, denoted (a) through (d) in the figure, are selected from this plot for visualization and are identified in the Pareto front and its orthogonal projections using different colors. Figure 61a shows one of the individuals with the lowest value of f_T, reducing the maximum temperature by approximately 30 K. It can be seen from the figure that the

(45)

algorithm converged to an individual that communicates the inflow and outflow locations with a single path of interconnected microchannels, passing through the two hot spots. This solution has a poor performance for the flow efficiency objective function. The individual in Figure 61b minimizes the void volume fraction, as it connects the inflow and outflow locations with an almost straight path of microchannels. The individual shown in 61c maximizes the flow efficiency, as it divides the flow in as many channels as possible to the cost of increasing the void volume fraction. Finally, an individual with intermediate values was chosen for visualization. This individual, shown in Figure 61d, reduces the temperature by approximately 18 K and it also has low values for the flow efficiency and void volume objective functions. With the entire Pareto-optimal front, the analyst is given enormous flexibility at the time of choosing the final design of the microvascular network.

Optimal network configurations in 2D and 3D microvascular systems: The computational tools developed were used to optimize a variety of 2D microvascular materials for void volume fraction, flow efficiency, maximum temperature, and surface convection objective functions   The computational framework was then extended to optimize 3D


(a) Individual with lowest ϕ_T.

(b) Individual with lowest ϕ_V.

(c) Individual with lowest ϕ_F.

(d) Intermediate individual.

Figure 61. Pareto-optimal surface after 40,000 generations (top) and selected individuals with distinct trade-off values between objective functions, (a) through (d).

embedded networks for active cooling applications.

Figure 62 shows one of these problems, where a uniform heat source is applied to the central strip between the two holes of the 2D domain. The figure shows the temperature in the absence of flow, the microvascular network template used for the optimization (i.e., the set of micro channels on which the network is to be defined) and the flow boundary conditions. The optimized network geometries are illustrated in Figure 63 for constant power and constant mass inflow rate. For constant power, the mass inflow rate is scaled so that the power, defined as the product of the pressure and mass flow rates at the inlets, remains constant for all the candidate solutions. The selected network topologies minimize the maximum value of the temperature over the 2D domain, and it can be seen that the flow is entirely collected through the central strip where the localized heat source is applied.
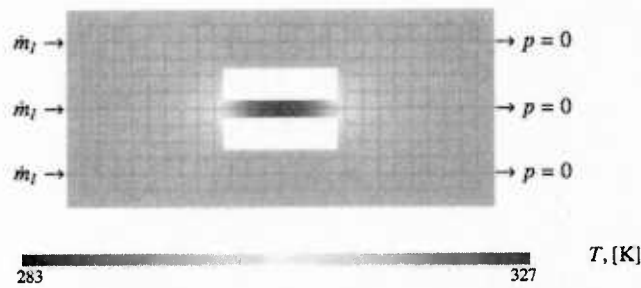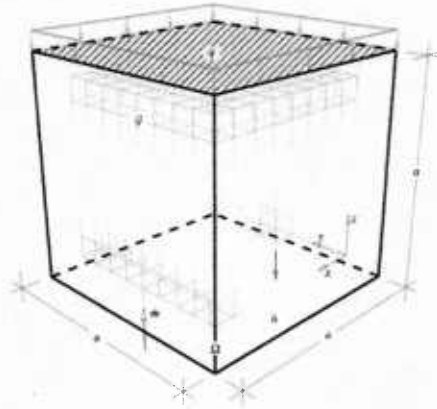

Figure 62. Microvascular network template with 446 microchannels showing the flow boundary conditions with three inflow and three outflow locations and the temperature solution in the absence of flow for the uniform heat trap example.
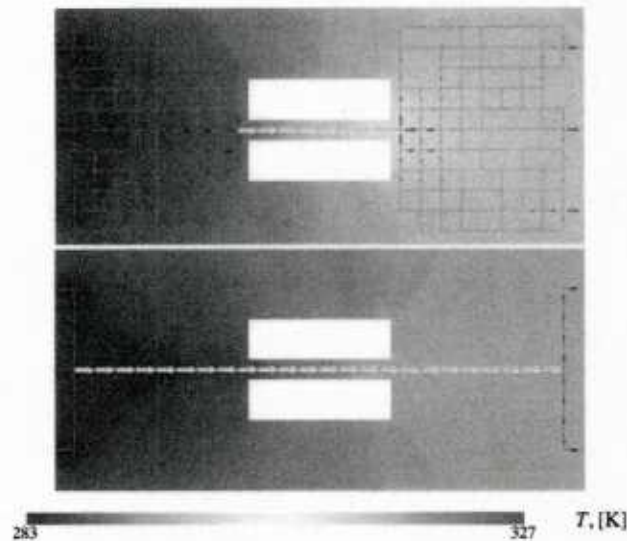

Figure 63. Optimized network topologies for constant power (top) and constant inflow (bottom). The GA converges to networks that collect the flow entirely through microchannels passing through the central strip where the heat source is applied.

μVAC a new paradigm in materials design

(47)

Figure 64. *Cubic domain and part of the microvascular network template. A single inflow and a single outflow are displayed with arrows. A uniform heat flux q is applied at the top surface, and prescribed temperature u is prescribed at the bottom surface. The remaining surfaces have periodic boundary conditions, thus defining a unit cell periodic in the x and y directions.*

| 273 | | 373 | T, [K] |
| 0 | | 1 | $\dot{m}$, [g/min] |
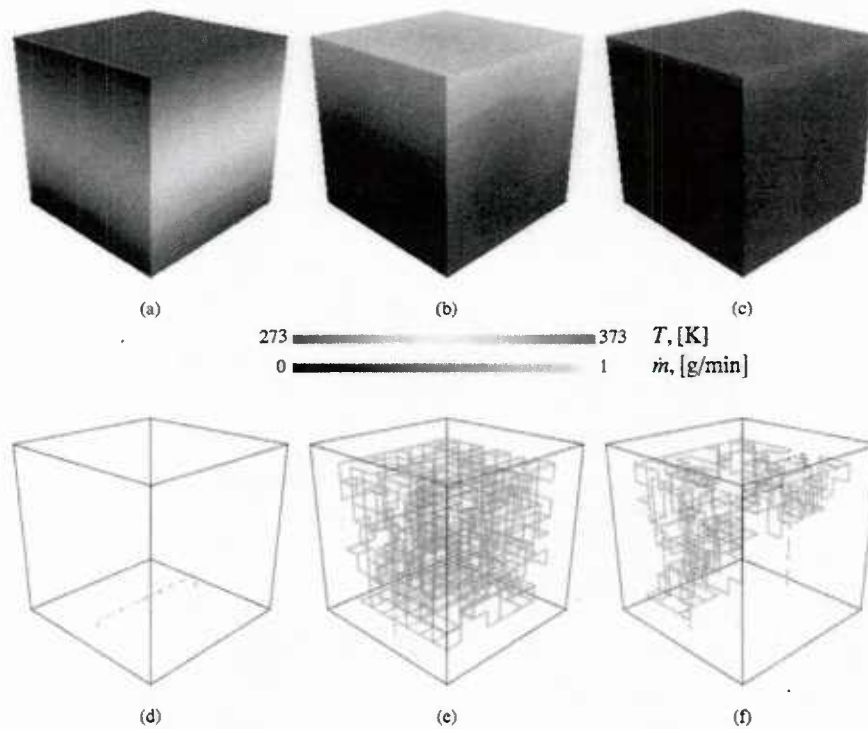
Figure 65. *Selected candidate solutions at generation t = 10000. Upper and lower rows show the temperature and flow fields, respectively. Figures (a) and (d) minimize the void volume fraction, figures (b) and (e) maximize the flow efficiency and figures (c) and (f) minimize the maximum temperature.*

(48)

This multi-physics optimization framework has then been extended to accommodate the design of 3D polymeric components. Figure 64 shows the schematic of a polymeric cell that has periodic boundary conditions in two directions for the thermal boundary value problem, prescribed temperature at the bottom surface and prescribed heat flux at the top surface. Selected individuals resulting from the optimization are illustrated in Figure 65 after 10000 generations. The individual that minimizes the void volume fraction connects inflow and outflow with a straight path of channels, (a-d). The flow efficiency is maximized by having a dense network such that the pressure drop is minimized (b,e). Finally, the individual that minimizes the maximum temperature (c,f) pushes the flow to the top surface where the heat flux is applied and eliminates the unnecessary network at the center of the domain.

μVAC   a new paradigm in materials design

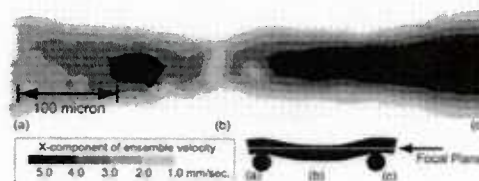## 2.4 Theme IV: Experimental Assessment & Analysis

2.4.1 Optical Diagnostics for Complex Microfluidic Systems

Particle-image velocimetry (PIV) is a well-established technique for measuring instantaneous velocity fields in macroscopic flows. In standard PIV, a flow of interest is seeded with tracer particles and a field of view is illuminated with two time-delayed, pulsed laser sheets. The scattered light from the particles for each laser pulse is imaged onto separate frames and correlation analysis is used to estimate the instantaneous fluid velocity from the particle motion. Microscopic PIV employs the same basic principles, though volumetric illumination is used instead and the depth of focus of the measurement is defined by the imaging system. At present, we are tailoring the micro-PIV technique to the measurement of flow fields within microvascular networks in order to document the complex flow paths encountered in these systems. The technical challenges include optimizing the illumination intensity, particle size and particle concentration so as to minimize out-of-focus image noise due to volume illumination. Overcoming these challenges allows us to study the instantaneous flow physics within microvascular networks.

Figure 66a presents an image of a microvascular network constructed using the direct-write assembly of Prof. Lewis. This network consists of five layers, with the channels in each layer perpendicular to those in the next, and the layers are connected at each crossing point (see idealized schematic in Figure 66b). All layers and channels are connected to a single large reservoir that surrounds the perimeter of the system. These characteristics of the network can generate extremely complex flow paths in the system.
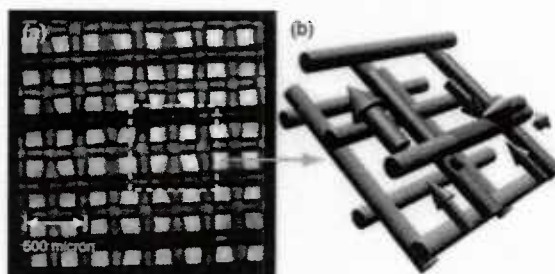

Figure 66. *(a) Image of multi-layer microfluidic device. (b) Schematic of the detected flow path.*

The flow path through each layer was successfully measured by micro-PIV. Measurements were made for each depth layer separately by tailoring the illumination energy to minimize out-of-focus noise from the other layers. Figure 67 presents an ensemble-averaged velocity

Figure 67. *Velocity field measured in a top-layer channel for the network shown in Figure 66.*

field through a top-layer channel along its center. The flow curiously slows down in the middle of the measurement field (labeled b) which should not occur for a constant-diameter channel. Careful examination of the channel geometry reveals that its center, coincident with label (b) in Figure 67, bows downward slightly, meaning the PIV measurement occurs closer to the channel wall at (b) than at (a) or (c). This particular example highlights the strong capabilities of micro-PIV in resolving the detailed flow characteristics within these complex networks. The composite flow path documented by the multi-layer micro-PIV measurements is shown schematically with arrows in Figure 66b.

Flow Mapping in Microvascular Networks: Microvascular networks designed for self-healing and/or self-cooling purposes must efficiently distribute flow through all available branches of the network. Efficiencies less than 100% in this regard could severely degrade the overall effectiveness of these autonomic systems. To this end, microPIV is employed to study the distribution of flow in various network configurations designed and manufactured by the µVAC team. Figure 68 presents a model two-dimensional network manufactured using the direct ink writing technique for which the distribution of fluid flow has been mapped. The diameters of the branches of this network were designed using Murray's law, with the inlet and outlet branches having diameters of ~520 µm and the smallest segments having diameters of ~200 µm. Using ensembles of 50 velocity realizations acquired in each branch of this network, the fraction of inlet flow rate within each segment was assessed. Figures 68a and 68b present the results of this flow-mapping analysis for flow rates of 0.5 ml/min and 5 ml/min, respectively, with blue denoting segments where flow is observed and red indicating segments that exhibit no flow. Only 16 of 36 segments (44%) display flow at 0.5 ml/min, indicating significant blockage in the model network. However, increasing the flow rate (and hence the inlet pressure) eliminates most of this blockage, as 31 of the 36 segments (86%) exhibit flow. This result indicates that high inlet pressures may serve as an effective "activation" mechanism by opening branches of a network that are inaccessible at lower pressures.
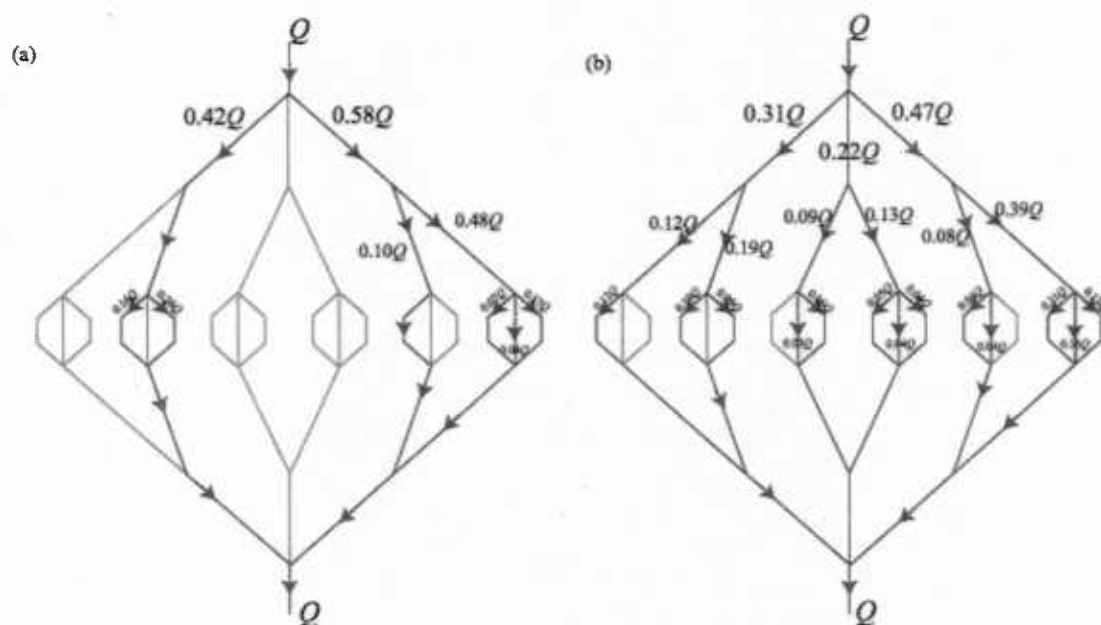

Figure 68. Flow mapping by microPIV within a model two-dimensional network for flow rates of a) 0.5 ml/min and b) 5 ml/min. Blue denotes segments where flow is detected while red indicates segments that exhibit no flow. The fraction of inlet flow rate, Q, measured in each segment is also noted.

Microscopic particle-image velocimetry (micro-PIV) experiments were performed as a means of documenting the momentum-transport characteristics of fluid flow through various microvascular network designs fabricated as a part of this effort. In particular, flow-mapping measurements are conducted for flow through various epoxy fin specimens devised by the

(51)

White Research Group for enhanced surface cooling and manufactured with the direct-write technique. These flow-mapping measurements are intended to complement IR-thermography measurements conducted by the White group by providing crucial information about transport within the individual channels of the networks. Since these networks inherently contain minor
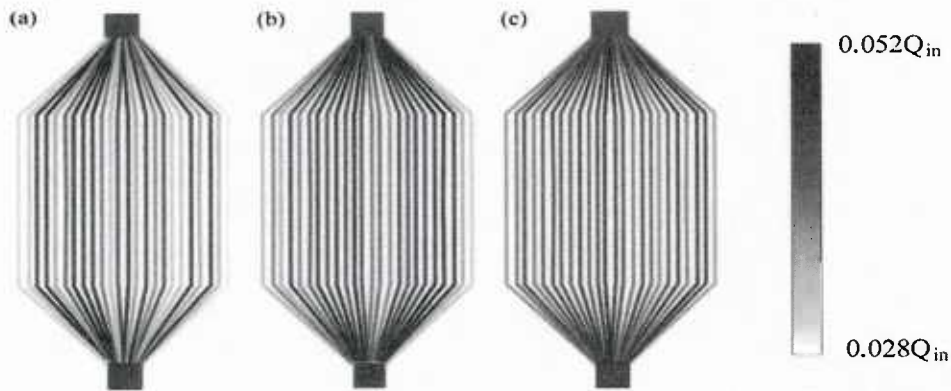
Figure 69. Flow maps for a single-layer, 24-channel network at input flow rates of (a) 1 ml/min, (b) 5 ml/min and (c) 10 ml/min, respectively.

defects at and near their surfaces, faithful imaging of tracer particles through these defects is challenging since they inevitably scatter a significant portion of the fluorescent emission from the tracer particles, reducing the measurable fluorescence. This difficulty was met with two remedies whose combined advantages allowed accurate evaluation of the fluid flow within these samples. First, 2 µm fluorescent tracer particles, which provide enhanced fluorescence in the presence of these defects, were employed instead of the 1 µm tracer particles typically used for micro-PIV measurements with a 10X objective lens. In addition, the seeding density was reduced to a volume fraction of 0.012% which provided additional improvement of the signal-to-noise ratio of the particle images. As a consequence, ensemble averaging of correlation functions was utilized in order to obtain well-resolved velocity fields within these specimens.

Figures 69a-c present flow maps (as contour plots) obtained for an epoxy fin specimen containing 24 microchannels (nominal diameter: 200 µm) for input flow rates of 1 ml/min, 5 ml/min and 10 ml/min, respectively. Examination of these flow maps suggests that the flow distribution through all 24 microchannels tends toward uniformity with increasing flow rate. A similar trend is noted in the flow maps obtained for the second epoxy fin sample (results not shown) containing 12 microchannels (nominal diameter: 400 µm). In addition to the above measurements, pressure-drop and flow-mapping measurements were performed as a means of characterizing the flow through
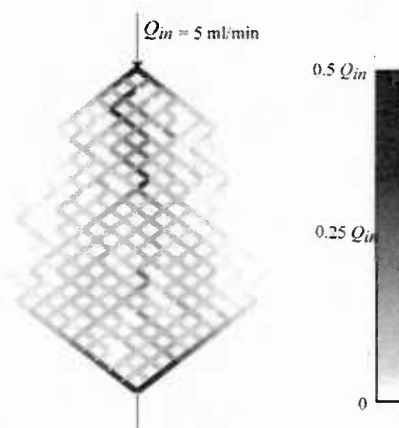
Figure 70. Flow map for the 45° network at an input flow-rate of 5 ml/min.

the "regular" and "45°" networks manufactured using the direct-write technique by the Lewis Research Group. The flow map for the 45° network at an input flow rate of 5 ml/min (Figure 70) indicates that the central portion of the network is much more active compared to its extremities. A similar observation is also noted for flow through the regular network (result not shown), though the pressure drop across the 45° network is roughly twice that of the regular network.

Microscopic particle-image velocimetry (micro-PIV) experiments are performed as a means of documenting the momentum-transport characteristics of fluid flow through various microvascular network designs fabricated as a part of this effort. Our focus last year was on mapping the flow within various single-layer microvascular systems. More recently, we have applied the micro-PIV technique to the challenging case of flow mapping within multilayer specimens wherein fluorescence from tracer particles residing in microchannels in the depth can introduce significant noise in the velocity measurements. Figure 71a presents a photo of the multi-layer specimen in which 24 microchannels reside at each layer with the microchannels in layers 1 (top) and 3 (bottom) parallel to one-another and the microchannels in layer 2 perpendicular to those in layers 1 and 3. The microchannels across the layers are interconnected, allowing fluid to move between layers. Figures 71b,c present the flow maps (as contour plots) obtained for layers 1 and 2 in this three-layer network for an input flow rate of 5 ml/min. The flow through layer 1 is relatively uniform due to the applied pressure difference that drives the flow from left to right; however, a region of near-zero flow is noted in the lower right quadrant (white contours). Evidently, there exists a flow blockage at this spatial location that inhibits fluid motion and, based on the flow mapping for layer 2 [Figure 71c], this fluid is bypassed upward into layer 2 and quickly back to layer 1 downstream of the obstruction where uniform flow is quickly recovered. This result highlights a key advantage of the microvascular networks under study: Even though flow blockages may occur intermittently in these systems, the significant interconnection of the flow passages provides a robust means of locally bypassing any obstructions and quickly recovering relatively uniform flow.
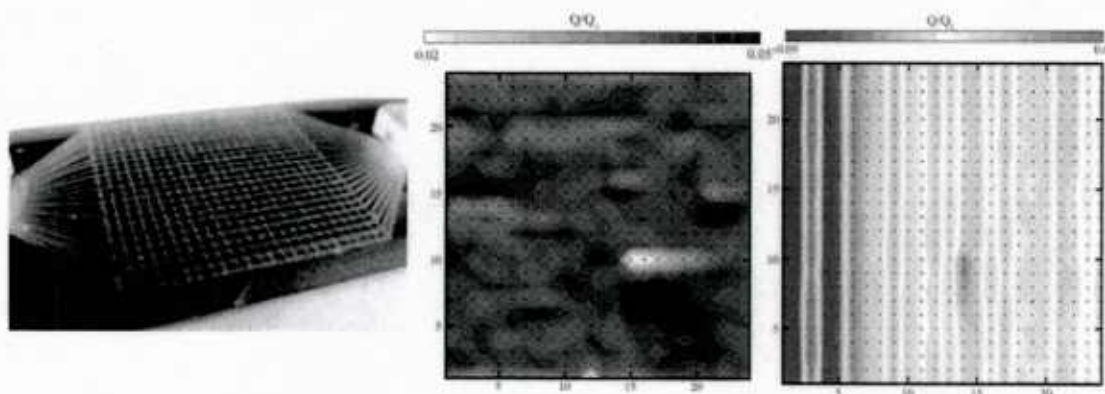
Figure 71. (a) Photo of three-layer network containing 24 microchannels per layer. (b,c) Flow maps in layers 1 (top) and 2 (middle), respectively, for an input flow rate of 5 ml/min.

2.4.2 Fluorescent thermometry diagnostics

The use of complex microvascular networks for self-cooling applications as well as the effective monitoring of temperature-sensitive processes requires the accurate measurement of fluid temperature fields at the microscale. The two-color LIF (Laser Induced Fluorescence) method, which utilizes a mixture of temperature sensitive and insensitive fluorescent dyes to improve the accuracy of the measurement through the elimination of variations in illuminating intensity, is being adapted for temperature measurement in complex microfluidic devices. Figure 72 presents a schematic of the optical setup developed for our two-color micro-LIF measurements. The dye mixture is illuminated with a pulsed, Nd:YAG laser and the fluorescence emission

Figure 72. Schematic of two-color LIF setup.

from the dyes passes through an objective lens followed by a long-pass filter that removes any remaining illumination light. The fluorescence of each dye is then separated using a dichroic filter cube which directs wavelengths of $l < 600$ nm toward camera a and transmits larger wavelengths toward camera b. A short-pass filter just upstream of camera a provides an additional filtering step before the fluoresced light is imaged. Similarly, an additional long-pass filter is positioned just upstream of camera b to further purify this fluoresced light prior to imaging.
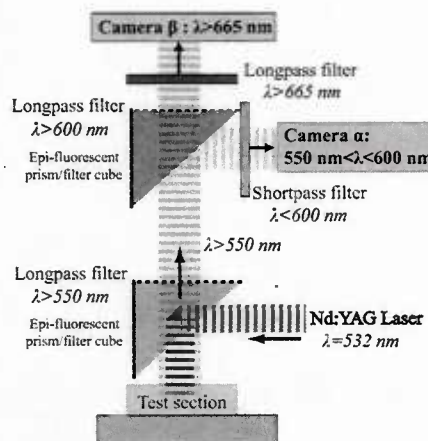
Our first microscale implementation of LIF utilized Rhodamine B (RhB) and Nile Red (NR) as the temperature sensitive and insensitive dyes, respectively, with ethanol as the solvent. Rhodamine B was chosen because of its strong temperature sensitivity and successful use in macroscale LIF (Sakakibara et al. 1999) while NR was selected because of its low sensitivity to temperature as well as its absorption and emission characteristics. Recall that two-dye LIF relies upon the temperature dependence of the ratio of the fluorescence intensities of the dyes, I_{RhB}/I_{NR}, to infer the temperature of the fluid. Calibration of the temperature dependence of I_{RhB}/I_{NR} yielded a temperature sensitivity of -0.37%/K and a measured temperature uncertainty of ~±2°C (an order of magnitude larger than the uncertainty achieved in macroscale two-dye LIF). This high uncertainty was traced to two difficulties: extremely low levels of fluorescence generated by the dye combination and weak temperature sensitivity of the dye combination. The former difficulty is inherent to two-dye LIF as the dye concentrations must be held extremely low to capture spatial variations in temperature at the microscale. We have addressed this issue by purchasing two new cooled, 12-bit CCD cameras that have extremely low noise levels and over an order of magnitude improvement in sensitivity compared to our current imaging capabilities (These cameras have yet to arrive; however, we have performed preliminary experiments using a single demo camera). The issue of weak temperature sensitivity of the RhB-NR combination is addressed by selecting Sulforhodamine-101 (SR101) as a replacement for NR. Its absorption spectrum is amenable to excitation with an Nd:YAG laser (λ_{abs} = 558 nm) and its emission spectrum (λ_{em} = 610 nm) can be separated from both the illuminating wavelength and the emission wavelength of RhB when dissolved in ethanol. Calibration of the RhB-SR101 combination gives a temperature sensitivity of approximately -1.83%/K, a factor of five enhancement over the RhB-NR combination.

The effectiveness of the RhB-SR101 dye combination was recently validated in an LIF measurement of a one-dimensional steady-state temperature gradient at the microscale. The microfluidic device constructed for this experiment consists of seven parallel microchannels (width = depth = 100 µm) fabricated between two large reservoirs (width = depth = 3.2 mm) spaced 2 mm apart (Figure 73a). These reservoirs were held at constant, but different, temperatures (independently monitored by thermocouples inserted into the reservoirs), generating a linear temperature profile across the microchannels which were filled with the RhB-SR101 mixture. Figure 73b presents the variation of the steady-state temperature distribution across the microfluidic device measured by two-dye LIF compared with the linear profile predicted from the thermocouple measurements. Unfortunately, only one demo camera was available for this experiment so the emissions from RhB and SR101 were not acquired simultaneously. Despite these limitations, the fluid temperatures measured by LIF agree well with the predicted linear profile, with a maximum deviation of 1 °C and an RMS deviation of approximately 0.2 °C observed.

(a)   (b)
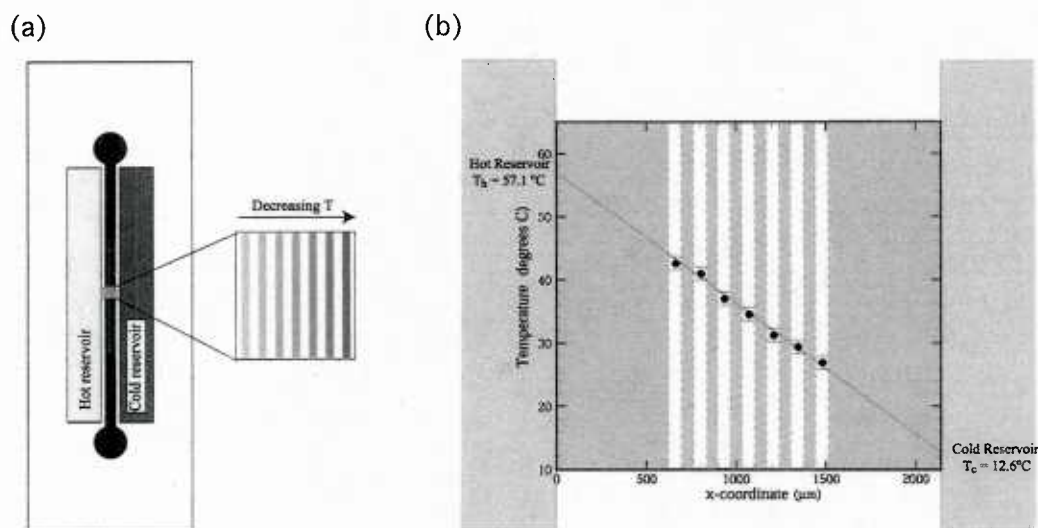
Figure 73. a) Schematic of the microfluidic device used to achieve a one-dimensional steady-state temperature gradient. b) Variation of temperature across the device shown in a). The solid circles represent the two-color LIF measurements while the solid line indicates the linear temperature profile across the microchannel array predicted from the reservoir temperatures measured with thermocouples. The error bars are ±1°C.

Thermal Assessment of Cooling Networks: In order to document the thermal characteristics of flow through complex networks embedded within a material or a device, extension of the two-dye, laser-induced fluorescence (LIF) technique (Sakakibara et al. 1999) for performing instantaneous measurements of temperature to the microscale was undertaken. In such a system, the first dye (Sulforhodamine-101) is insensitive to temperature and imaging its emission yields a direct measure of variations in image intensity due to variability in the incident laser light. The second dye (Rhodamine B) is temperature sensitive and its fluorescence intensity, relative to the first dye, yields an unbiased measure of the fluid temperature with high spatial resolution. On illuminating the dye mixture in the test section with an appropriate illumination source, the fluorescence emissions from both dyes are separated into their temperature-sensitive and -insensitive counterparts using optical filters. The separated emissions are then imaged using two identical CCD cameras and the ratio of

their emission intensities is converted into temperature using an a priori calibration of the intensity ratio as a function of temperature (See Natrajan et al. (2008a,b) for further details).

The principal modification of our earlier implementation of the two-dye LIF methodology at the microscale is the use of water as a solvent. Calibration of the temperature dependence of the intensity ratio of both dyes, I_{RhB}/I_{SR101}, with water as the solvent, illustrates a temperature sensitivity of 2.7%/K. This result represents an enhancement over our earlier implementation in ethanol by a factor of approximately 1.5. Feasibility of this methodology for conducting temperature measurements is explored by assessing the steady-state, linear temperature profile generated across a microfluidic channel array with two large hot and cold reservoirs (Mao et al. 2002). These measurements reveal mean steady-state temperatures in the microchannels within ±0.4°C of the predicted temperatures with experimental uncertainties (based on standard deviation) of ±0.48–0.59°C (relative uncertainties of 1.2–1.9%). We have also explored the feasibility of a single dye, two-color system (see Natrajan et al. 2008b) for details).

We have also validated this methodology via measurement of fluid temperature for laminar flow through a heated rectangular copper microchannel (length=265mm, width=900μm, depth=450μm). LIF measurements are conducted at an axial location that is 190mm downstream of the channel inlet where, for the present case of laminar flow at Re=500, the flow is both hydrodynamically- and thermally-developed. The mean temperature profile obtained by ensemble averaging several instantaneous LIF measurements followed by line averaging in the axial direction (Figure 74) illustrates a parabolic character, consistent with that predicted by the analytical solution of the energy equation for thermally-developed laminar flow. In this regard, the temperature profile is symmetric about the channel centerline with a temperature difference between the centerline fluid and the microchannel wall of approximately 48°C.

Finally, two-color LIF is employed to measure fluid temperature for flow through an epoxy fin containing three embedded microfluidic channels (nominal diameter: 500 μm) with a common inlet [Figure 75(a) includes a schematic of the specimen]. This device was designed as a baseline cooling system for which results of IR thermography (White group), LIF thermometry (Christensen group) and numerical simulations of thermal transport (Geubelle group) could be directly compared. The specimen is heated at the surface that is formed

Figure 74. Mean temperature profile for laminar flow at Re = 500 through a heated rectangular copper microchannel (schematic shown as inset).

by its length and thickness, meaning channel 3 is closest to the heat source while channel 1 is furthest away. Fluid temperature measurements are conducted at two streamwise locations downstream of the network inlet in each of the three channels. These locations are coincident with the upstream and downstream boundaries of the IR measurements of the White group. Figures 75(a-c) present the measured temperature profiles within the top-most, middle and bottom-most channels at the upstream and downstream locations (blue and red lines, respectively). These results indicate that, at a fixed axial location, the fluid temperature
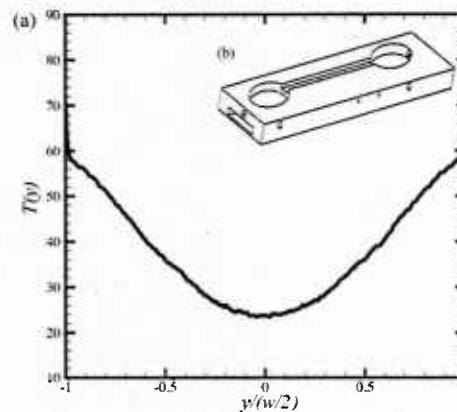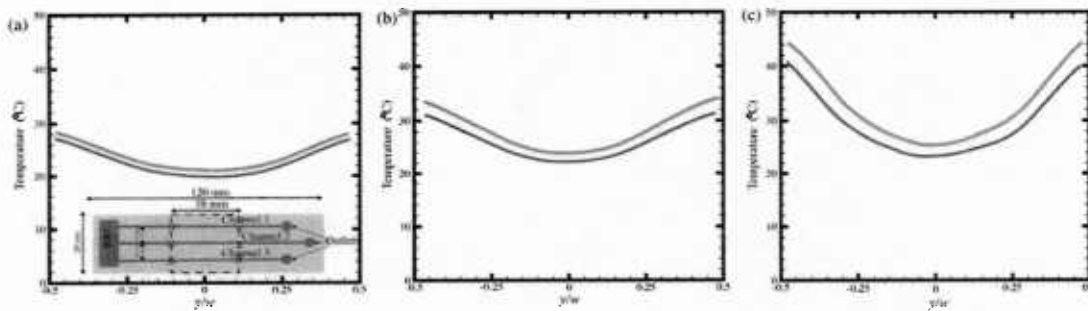
Figure 75. Temperature profiles garnered from two-color LIF for flow through the (a) top-most, (b) middle and (c) bottom-most channels of a heated three-fin specimen [schematic of the device shown as an inset in part (a)]. The blue and the red lines show the temperature profiles measured at the upstream and downstream locations in each channel, respectively.

decreases as one moves from the bottom-most channel to the top-most channel. Additionally, the rise in the fluid temperature between the upstream and downstream locations in each of the three channels decreases as one moves away from the heat source. These trends are consistent with the IR measurements within the solid surface of the fin by the White group.

2.4.3 Heat-transfer enhancement in microvascular networks

Multiple methods for enhancing heat transfer in microvascular networks meant for self-cooling applications have been investigated. Of keen interest is identifying methods for achieving such enhancement with little or no additional penalty in the pumping-power requirements. Two approaches have shown particular promise for heat-transfer enhancement either using surface roughness within the interior of the microvascular flow passages or altering the layout of the flow passages (adding curvature).

Internal Surface Roughness: All flow passages, whether macro- or micro-scale contain interior surface defects either due to imperfect fabrication or through the use of internal coatings required to satisfy other operating restraints. In this latter regard, interior coatings are under investigation by others on the micro-VAC team to reinforce the structural integrity of the microchannels within microvascular systems and these coatings actually leave behind surface roughness that might be further leveraged for enhanced convective heat transfer. To explore this possibility, a carefully-designed microchannel test rig was constructed from copper to assess the impact of weak, yet irregular, surface roughness on convective heat transfer in microchannels of similar size (hundreds of microns) and at similar flow rates (tens of ml/min) germane to micro-VAC applications. The surface roughness considered was generated using a sand blaster to roughen the interior surfaces of the copper microchannel test rig. Local heat transfer coefficients were then measured with water as the coolant using a two-color fluorescent thermometry technique (Natrajan et al. 2009) for both smooth- and rough-wall conditions. Figure 76(a) presents normalized pressure drop across the microchannel as a function of Reynolds number (analogous to flow rate) illustrating that the roughness considered does not induce an additional drag penalty at flow rates germane to micro-VAC applications (shaded region). In contrast, roughness does indeed provide enhanced heat transfer as illustrated in Figure 76(b) which presents local Nusselt number versus normalized axial distance. Of particular importance to micro-VAC systems, roughness provides

(57)
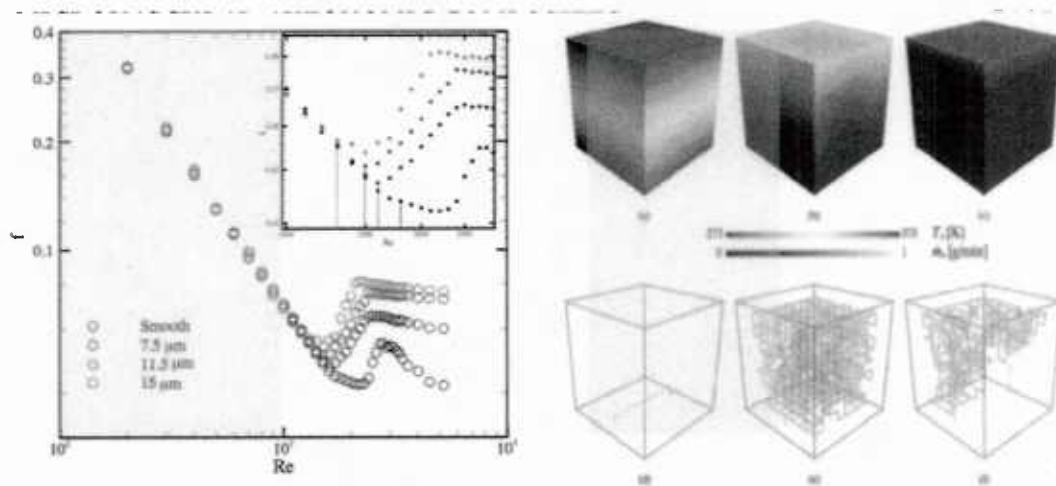
Figure 76. *(a) Normalized pressure drop as a function of flow rate for smooth and rough microchannels. (b) Local Nusselt number versus normalized axial distance. Shaded regions in both indicate no increased pressure-drop penalty but enhanced convective heat transfer for rough, short microchannels.*

significant heat-transfer enhancement at lower flow rates through shorter flow passages [thermally-developing flow; shaded region]. Since most microvascular networks consist of microchannels that are highly-interconnected and will therefore typically operate in a thermally-developing regime, these results indicate that heat-transfer enhancement compared to perfectly smooth flow passages should be expected so long as interior surface roughness (a few percent of the microchannel diameter) is present within these flow passages.

Optimizing Flow-Passage Geometry and Layout: The layout of the circular cross-section flow passages within microvascular systems was also investigated to induce flow motions that lead to enhanced convective heart transfer at flow rates germane to micro-VAC applications. Two configurations have been assessed computationally: varying cross-sectional diameter (varicose) and serpentine (sinuous) microchannels (Figure 77). As noted above, of primary interest is identifying variations from standard straight microchannels that lead to heat-transfer enhancement with as little additional penalty in pumping power as possible compared to a straight microchannel.
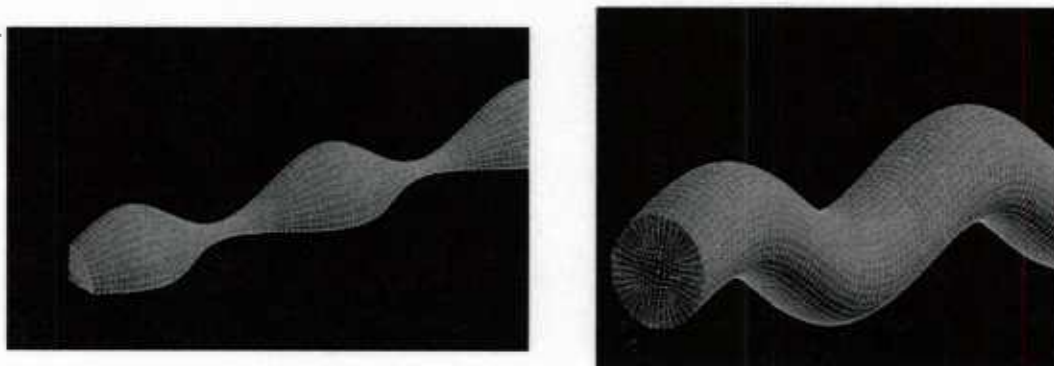
Figure 77. *Grid structure illustrating varicose (left) and serpentine (right) microchannel configuration under consideration.*
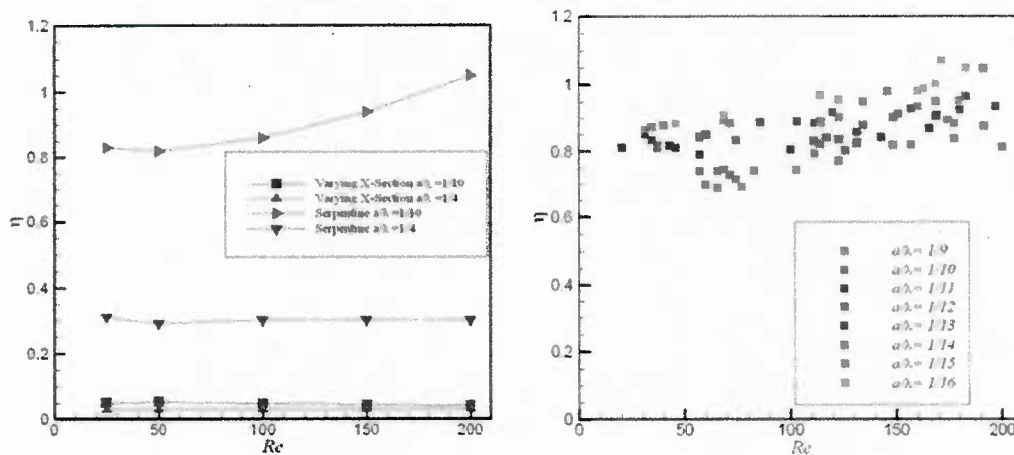

(58)

Figure 78. (a) Efficiency versus Re for varying cross-section and serpentine microchannels of equivalent waviness. (b) Efficiency versus Re for serpentine microchannels over a range of waviness.

Figure 78 presents efficiency versus Re for several different a/λ cases for varicose and serpentine microchannels and efficiencies greater than unity are found for higher flow rates and $a/\lambda < 1/15$. Thus, the use of serpentine microchannels in conjunction with internal surface roughness holds significant promise in greatly enhancing convective heat-transfer at the relatively low flow rates utilized in self-cooling micro-VAC applications.

2.4.4 Microvascular coating healing

Repeated healing with singular microvascular networks: Three-dimensional, interconnected microvascular networks were used as a delivery system for healing agent in a coating-substrate system to heal damage to a polymer coating (Figure 79). The protocol for coated networks entails testing virgin samples in four-point bending until cracks initiate in the coating (Toohey et al. 2005). Damage in the coating, draws healing agent (DCPD monomer) from the channels into the crack where it reacts with Grubbs' catalyst embedded in the coating to heal the crack. After a healing period, the coating integrity is restored and if the crack reopens the healing process can be repeated. Concentrations of 2%, 5% and 10% by weight of unprotected catalyst were added to the epoxy coating to determine the effect on the healing ability of the system.

The coated microvascular beams were loaded to initiate a single crack in the coating without damaging the microvascular network. An acoustic emissions (AE) sensor was used to detect the crack opening events during testing. After testing each specimen, the AE data was
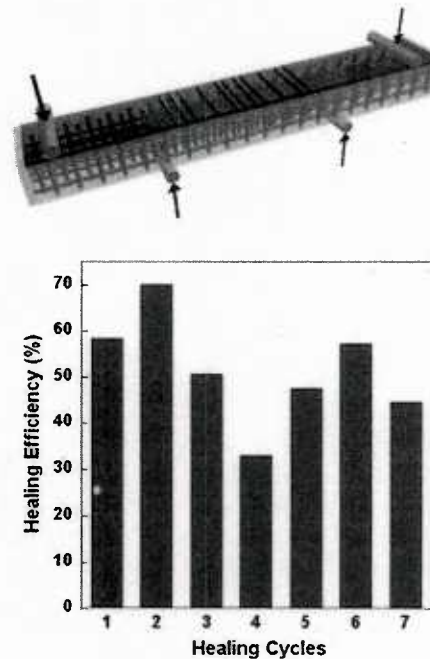

Figure 79. Self-healing coating on a mVAC substrate and the healing efficiency measured for seven consecutive tests.

examined to determine which load event corresponded to the critical crack-reopening event and to calculate healing efficiency ($\eta = P_{heal}/P_{virgin}$) for each healing cycle.

The number of healing cycles and the healing efficiency for each heal varied for different concentrations of catalyst. The coatings with the highest concentration of catalyst, 10% by weight, healed for the most number of cycles. Figure 79 displays the healing efficiency for the 1st through 7th heal tests of the best specimen containing 10% catalyst. There was significant scatter in the healing efficiencies between the different healing tests for and the peak healing occurred in the second test. The 8th heal test for this specimen indicated no healing. The average number of healing cycles for each set was 2, 2 and 4 cycles for coatings with 2%, 5% and 10% catalyst, respectively.

Repeated healing with dual microvascular networks: Three-dimensional, interconnected microvascular networks are used as a delivery system for healing agent in a coating-substrate system to heal damage to a polymer coating. The protocol for coated networks entails testing virgin samples in four-point bending until cracks initiate in the coating (Toohey et al., 2005, 2007). The self-healing process requires a suitable chemistry to polymerize the healing agent in the fracture plane. Repeated healing of the coating (7 consecutive cycles) was achieved via ring-opening metathesis polymerization (ROMP) of dicyclopentadiene (DCPD) monomer by Grubbs' catalyst, the same healing chemistry that was used successfully in prior microencapsulated composites (White et al. 2001). The DCPD monomer was delivered by the microvascular network and solid particles of Grubbs' catalyst were dispersed in the matrix. A maximum of 7 consecutive healing cycles was achieved. The number of healing cycles was limited by availability of catalyst.

We have found that the maximum number of healing cycles can be increased through use of a new two-part epoxy healing chemistry and dual microvascular networks. A dual network substrate was fabricated (Figure 80) to keep the two components separate prior to crack initiation in the film. After introducing EPON 813 Resin and Ancamide 503 curing agent in the microvascular networks, we were able to achieve 11 consecutive healing cycles of a single crack in a brittle epoxy resin (Figure 81). The number of healing cycles for the
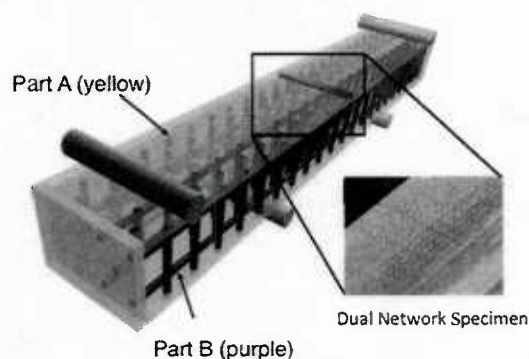

Figure 80. Dual microvascular network specimen for two-part healing chemistry.
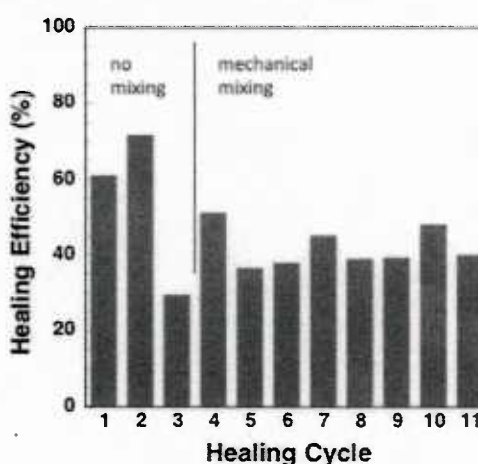

Figure 81. Healing efficiency as a function of loading cycles. Eleven consecutive healing cycles were obtained with the new two-part epoxy chemistry.

two part chemistry is limited by the efficiency of mixing within the crack plane.

Repeated healing with interpenetrating networks: We successfully developed a new interpenetrating network design to overcome mixing limitations in dual network specimens and significantly enhanced the number of possible repeated healing events with a two part epoxy based chemistry.

Self-healing specimens consisted of a brittle epoxy coating on a substrate with two independent, interpenetrating networks containing either EPON 813 resin or Ancamide 503 curing agent. The two components remained separate and stable prior to crack initiation in the film. After crack formation, the resin and hardener flowed to the crack plane and polymerized. Between testing periods, specimens were permitted to heal for 48 hours at 30°C. Over 30 continuous heal cycles were achieved (Figure 82), far more than possible with the previous DCPD/Grubbs' system (Toohey et al., 2007) and the two part chemistry without the new interpenetrating network design (Toohey et al., 2009a). The average healing efficiency of the new system decreased slightly with increasing cycles, but remained around 50% even up to 30 heal cycles.

2.4.5   Microvascular   volumetric healing

Microvascular self-healing was also achieved in a bulk material, as opposed to the previous substrate/coating approach, using a double cleavage drilled compression (DCDC) fracture sample (Figure 83). When loaded in compression, regions of high tensile stress developed at the top and bottom the hole, inducing a pre-crack to propagate parallel to the loading direction. Due to the confined regions of tensile stress, crack propagation was stable and controlled by the loading rate. The applied compressive stress necessary to propagate the cracks in a DCDC sample was crack length dependent, reaching a critical plateau with increasing crack length, as shown in

Figure 82. *Average healing efficiency for eight specimens over 30 continuous heal cycles.*

Figure 84. The critical stress intensity factor was determined from the value of this stress plateau (Plaisted et al. 2006).

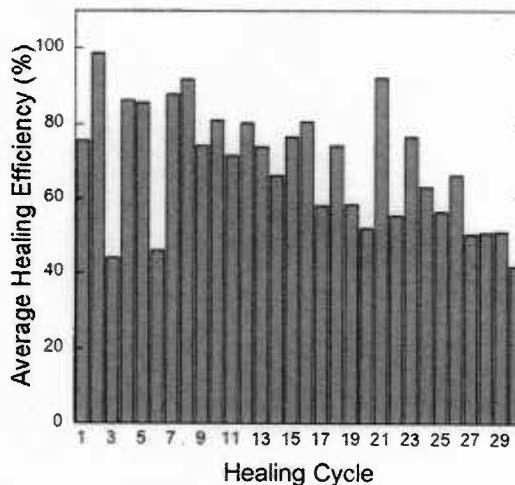The healing chemistry selected was the same two-part epoxy system (Epikure 3046 hardener and Epon 8132 epoxy resin) used by Toohey for the healing of a brittle coating on a microvascular substrate. The use of dual-ink robotically controlled deposition enabled fabrication of microvascular networks consisting of alternating, individually sequestered layers to prevent premature mixing of the two part healing. After crack propagation, the two components polymerized in the crack plane, effectively healing the crack.

Healing efficiency was evaluated as the ratio of the virgin material's fracture toughness to that of the healed sample (White et al. 2001). The epoxy healing system was allowed to cure for 48 hours at 30°C before evaluating the healed fracture toughness. Typical healing efficiencies on the first heal cycle ranged from 70% to 80% without disturbing the samples. As shown in Figure 85, repeated healing of cracks in the network was achieved for up to 10 healing cycles. First cycle healing efficiencies at or above 100% were achieved by inducing mixing of the healing components in the crack plane via cyclic transverse loading.

Figure 83. *DCDC microvascular sample geometry and images with each healing component fluorescently dyed.*

2.4.6 Structural response of microvascular networks

Mechanical assessment of networks under tensile load: The mechanical testing of microvascular networks utilizes a powerful full-field technique known as fluorescence-based digital image correlation (FDIC), which is capable of measuring nanoscale deformation using fluorescent nanoparticles (Berfield et al. 2006). Digital Image Correlation (DIC) is a data analysis method, which applies a mathematical correlation algorithm to obtain kinematic information from images acquired during deformation. For conventional DIC, samples are prepared for testing by the application of a random speckle pattern to their surface. In FDIC this random speckle pattern is produced by spin casting fluorescent nanoparticles onto the sample surface. Comparison of successive images reveals a deformed speckle pattern relative to the initial, undeformed pattern. The correlation works by matching small square subsets of the undeformed image to locations in the deformed image.
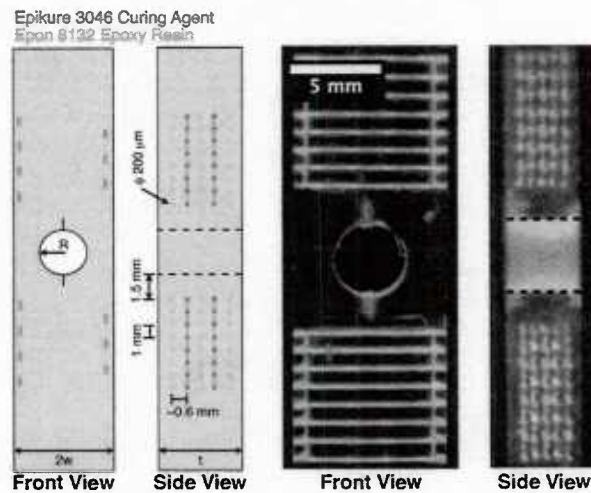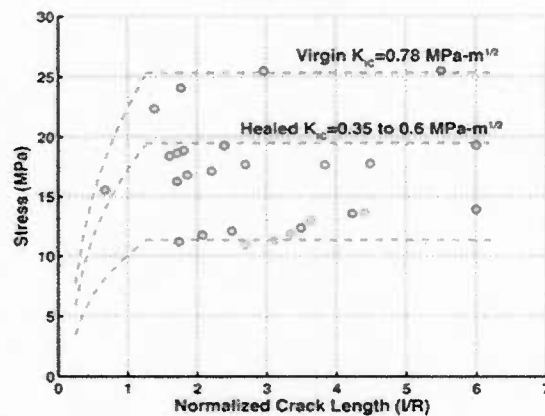

Figure 84. *Stress verses crack length for a DCDC sample during virgin fracture testing, and the first four healing cycles.*
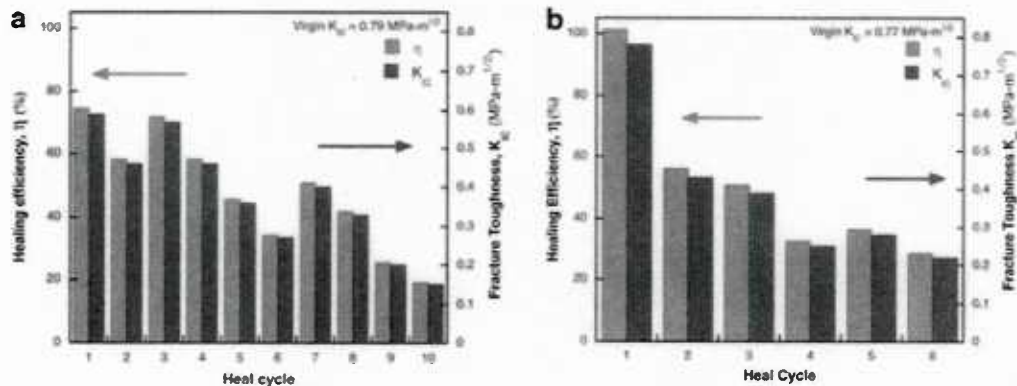
Figure 85. Healing efficiency and fracture toughness over repeated healing cycles for: (a) an undisturbed sample and (b) a sample that was cyclically loaded to induce mixing.

The FDIC technique was first applied to a model system for a microvascular network. The model sample consists of a single cylindrical hole 280 μm in diameter through a thin rectangular epoxy strip (30 x 2.8 x 1 mm). This geometry, loaded in uniaxial tension, has a full-field analytical solution with which to compare and verify experimental results. Correlating the images from this experimental setup resulted in the deformation field shown in Figure 86, which is inlaid with the analytically determined deformation field in the lower left quarter. The agreement between the analytical and experimentally determined displacements is excellent. Longitudinal strains calculated by differentiation along line scans are also in good agreement with analytically predicted strains. The successful application of this method to the simplified microvascular model confirms the robustness of the method and its usefulness in mechanical investigations of the microvascular networks. Preparations are now being made to extend the method to microvascular network geometries that have been developed for self-healing functionality.

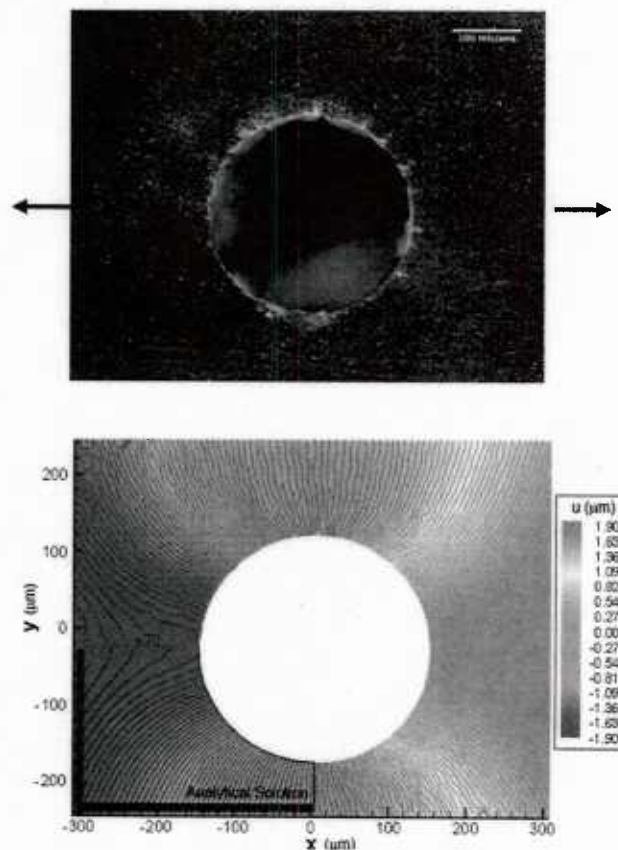**Crack-channel interactions:** We have developed a powerful fluorescence-based digital image

Figure 86. Single channel sample with fluorescent speckle loaded in uniaxial tension and corresponding displacement fields.

correlation (FDIC) method for measuring strain concentrations in microvascular networks (Berfield et al. 2006, 2007). The FDIC technique was successfully applied to measure local strain concentrations in networks loaded under unxiaxial tension. As expected, decreased channels spacing leads to increases in the strain concentration (Figure 87). The FDIC technique was also used to investigate interaction of an approaching crack with fluid-filled channels. Cracks are drawn to the lower stiffness region created by the channel. As shown in Figure 88, healing agent within the channels is able to wick out and cover the entire crack plane. FDIC measurements hold potential for evaluating localized healing in the networks.
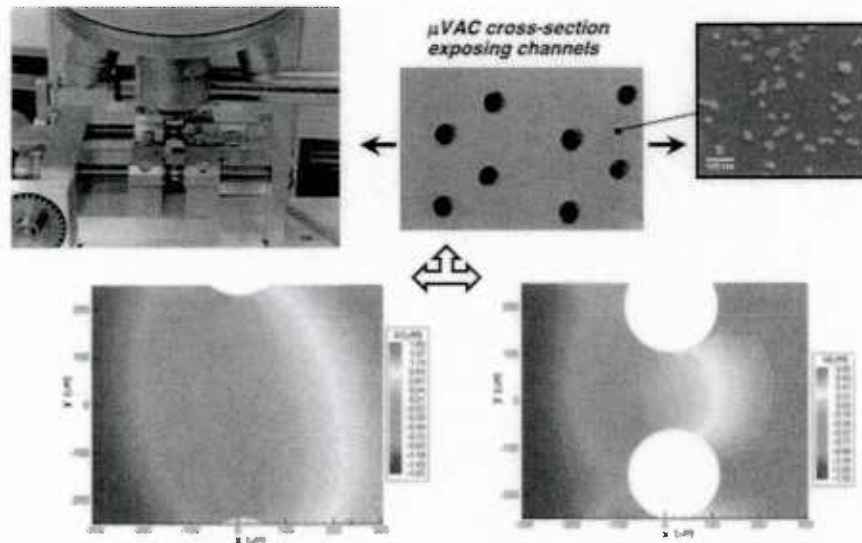

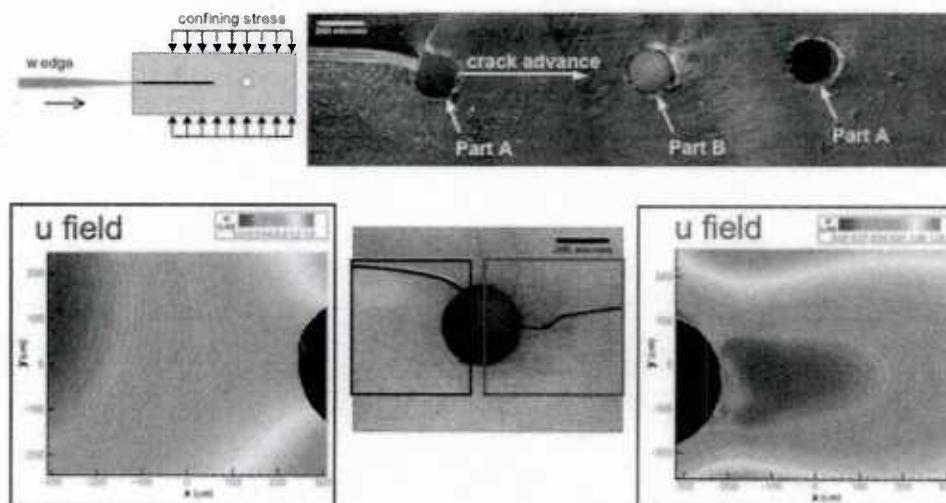*Figure 87. FDIC displacement contours show the effects of channel spacing for a network under uniaxial tension.*

Figure 88. FDIC displacement contours after a crack has intersected a fluid-filled channel.

Nanoscale Reinforcement of Microvascular Channels: We also explored the effects of channel reinforcement on the local strain concentrations in a microvascular self-healing composite. In preliminary experiments, single channels were reinforced by silane
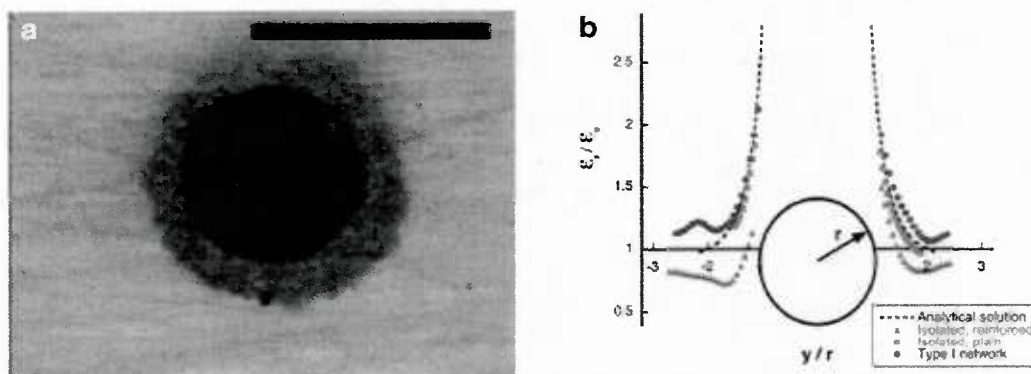
Figure 89. a) Optical micrograph showing alumina particle reinforcement around a microchannel. Scale bar is 250 mm. b) Comparison of normalized strain along a vertical line through the center of a reinforced and unreinforced channel.

functionalized 10 µm alumina particles (Figure 89a). The particle reinforcement was incorporated by deposition onto a wax ink scaffold prior to infiltration of the polymer matrix. Displacement and strain were measured by a fluorescent digital image correlation (FDIC) (Berfield et al. 2006, 2007). The stiffening effect of the particle reinforcement is evident from the normalized strain field in Figure 89b. The strain around a reinforced channel drops to values at or below the far-field strain in a shorter distance from the channel as compared to the case of no reinforcement. Because the reinforced material surrounding the channel is stiffer than the matrix, there is a decrease in strain when approaching this region.

We are examining deposition of nanoscale reinforcing particles through layer-by-layer assembly. The technique uses sequential immersion in aqueous solutions of oppositely charged particles to build uniform thin films with controlled thickness onto charged surfaces. This technique has been previously applied to make nanometer thickness halloysite aluminosilicate/polycation films on glass (Lvov et al. 2002). We have modified the standard hydrocarbon wax ink with small amounts of stearic acid to create charged scaffolds, leading to successful deposition of halloysite/polycation films as seen in Figure 90.
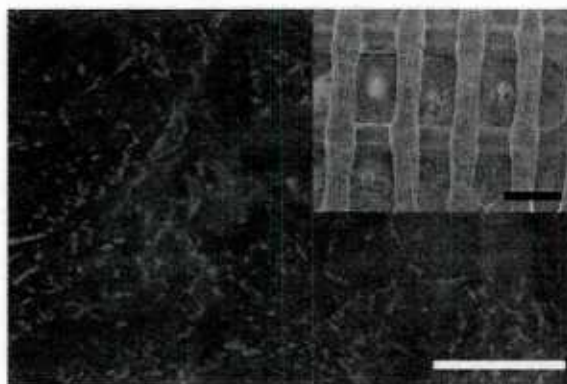

Figure 90. Scanning electron micrograph of wax scaffold (inset) and backscatter electron micrograph of scaffold surface with six-layer halloysite /poly(diallyldimethylammonium chloride) film deposited. Scale bars 500 µm and 5 µm, respectively.

μVAC a new paradigm in materials design

We have assembled multilayers of anionic halloysite aluminosilicate nanotubes and poly(diallyldimethyl ammonium chloride) (PDADMAC), a strongly charged polycation, onto direct-written wax scaffolds (Figure 91) which were transferred over to the interior surface of microvascular channels after epoxy infiltration (Figure 92). Strain in surface-coated channels under uniaxial load were measured using fluorescent digital image correlation (FDIC) microscopy (Berfield et al. 2006, 2007). These specimens demonstrated reduced strain concentrations near the channel, as shown by strain field maps (Figure 93a) and strain profiles through the center of the channel (Figure 93b). We are examining the effect of film thickness on the degree of reinforcement, as well as exploring additional particulate systems as candidates for multilayer assembly, such as silica nanoparticles (Figure 94) and alumina microparticles.
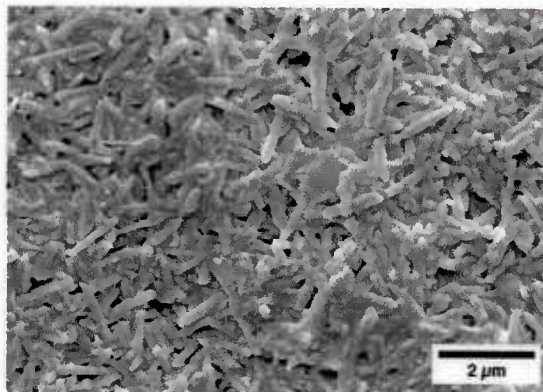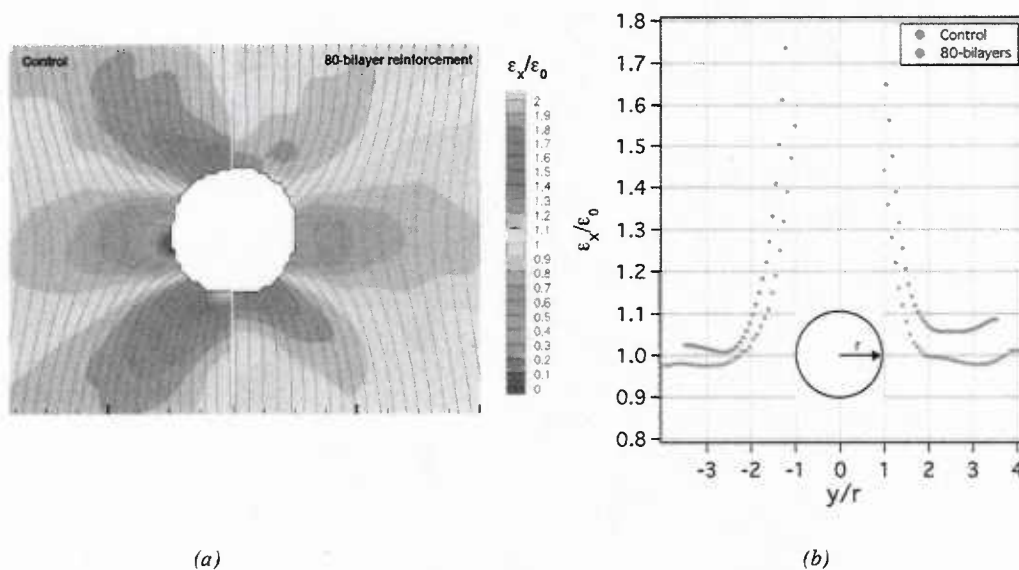

Figure 91. Scanning electron microscopy (SEM) image of (halloysite/PDADMAC) multilayer built onto wax substrate.
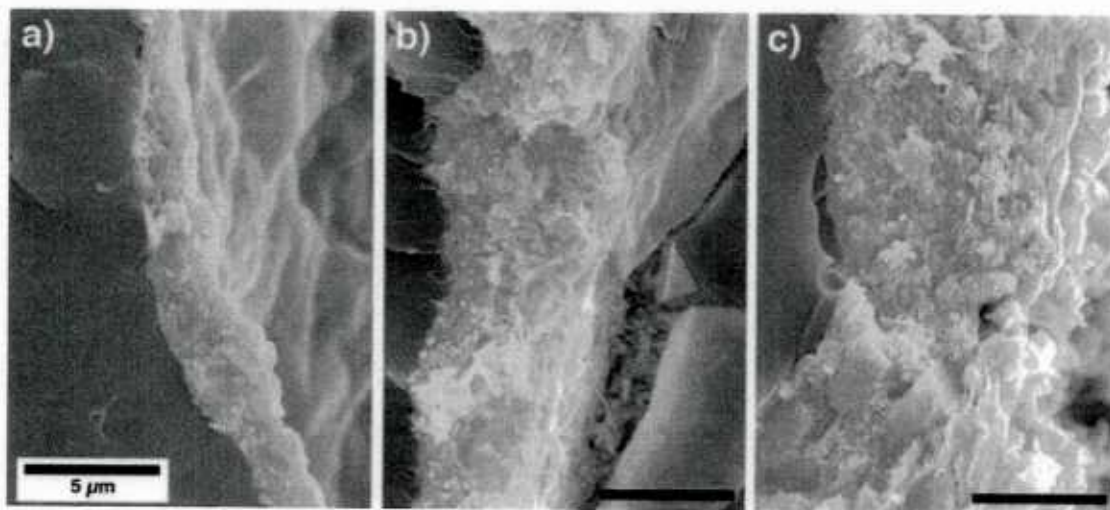
Figure 92. SEM image of microvascular channel cross-sections with deposited (halloysite/PDADMAC) multilayers. a)10-bilayers b)20-bilayers c)40-bilayers. Multilayer film edges are false-colored for clarity.

μVAC a new paradigm in materials design

(66)

(a)   (b)

Figure 93. (a) FDIC image showing strain relative to far-field strain around microvascular channels uniaxially loaded in the x-direction with; no multilayers, and 80-bilayers of (halloysite/PDADMAC) deposited. (b) Strain profile through the center of microvascular channels normal to the loading direction, with; no multilayers and 80-bilayers of (halloysite/PDADMAC) deposited.
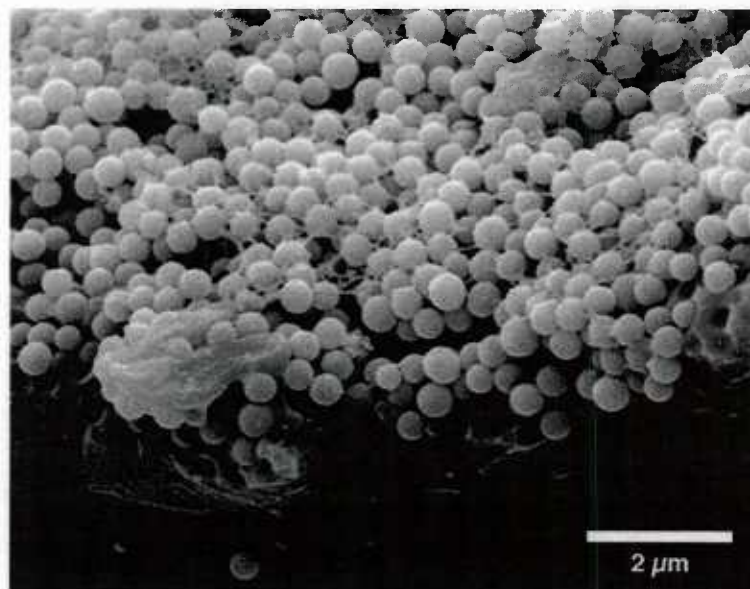
Figure 94. Microchannel cross-section with (silica nanoparticles/PDADMAC) multilayers.

2.4.7 Microvascular Cooling

Microvascular materials with interconnected three-dimensional networks offer an efficient method for active thermal control. The microscale of these networks offers advantages in convective cooling since the heat transfer coefficient scales inversely with channel diameter (Tuckerman et al. 1981). First, the effectiveness of active cooling using microvascular networks was examined using thin fin polymer structures with embedded microvascular networks. The effects of channel diameter, single versus multiple layer networks, and varying flow rates from 0.5 to 10 ml/min were examined. In addition, the cooling fluid was also studied by using both water and also a MIL-PRF-87252 coolant based on a hydrocarbon oil.

Thin fin polymer specimens were created in bulk polymer material using direct-write assembly (Therriault 2003). This process consists of writing the microvascular network with fugitive wax ink using robotic deposition. This wax structure is embedded in the bulk polymer matrix, and after the matrix is cured, the wax ink is removed using heat and vacuum. The final fin specimen dimensions were 19.5 mm high by 150 mm long by 3.5 mm thick, and four different microvascular networks were examined, each spanning 39.4 mm along the length of the specimen. First, control specimens were fabricated with no embedded microvascular network. A baseline specimen had 24 parallel channels of 200 μm diameter spaced 0.8 mm between channels. The third specimen had 12 parallel microchannels of 410 μm diameter spaced 1.6 mm between. Finally, an interconnected three layer network was created with three layers of 24 parallel, 200 μm channels with the middle layer perpendicular to the top and bottom layer.

The experimental setup consisted of mounting the fin to a heated copper plate with thermally conductive grease on the interface. The bottom of the specimen was heated to a constant 80° C while the top and sides of the fin were open to the environment at 23° C. The surface temperature was interrogated using a DeltaTherm 1560 infrared camera with a 256 by 320 pixel array of Indium Antimonide infrared detectors. After the heated equilibrium state was reached, the cooling fluid at 20° C was circulated at flow rates of 0.5, 1, 2.5, 5, and 10 ml/min using a syringe pump or diastolic pump depending on the volume of fluid necessary for the tests.

Two types of tests were performed on each specimen. First, the transient response from heated steady state to actively cooled steady state was examined by taking images at a rate of one frame per second. Then, the steady state cooled condition was examined averaging 20 seconds of data every five minutes for one hour. The results examined included horizontal averages over the height of the specimen and average field temperature of the entire surface over the network.

The control samples of solid polymer with no embedded microvascular network were compared to the thin fin analytical solution and a two-dimensional, steady state finite element model using ANSYS© software. The experimental results for the control samples correlated very well to the analytical and computational models with a maximum error of 2.2%. This verified the experimental procedure and validity of using the infrared camera in this study.

The average field temperature over time for water and oil coolant over time are shown in Figure 95. The average field temperature results for all test cases are shown in Figure 96. For all test cases, higher flow rates produced faster cooling rates and lower steady state temperatures.

First, the effect of channel diameter was studied by comparing the results of the single layer 200 and 410 μm diameter channels networks. The experimental results verified that the smaller channel diameter yielded faster and more efficient cooling. The larger diameter channels took approximately 1.7 to 2.5 times longer to reach equilibrium and the field average of the steady state cooled specimen was 2 to 27% higher in temperature. The largest differences were seen in the higher flow rates.
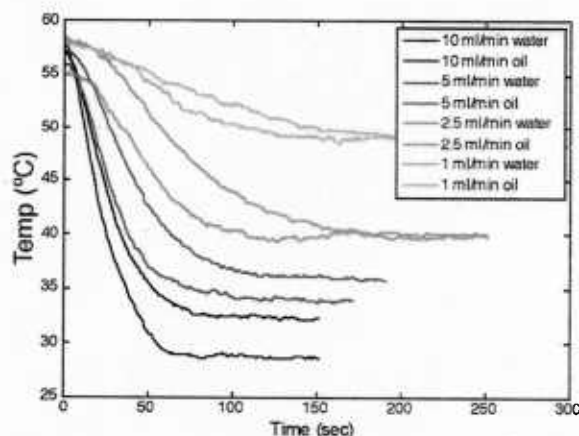

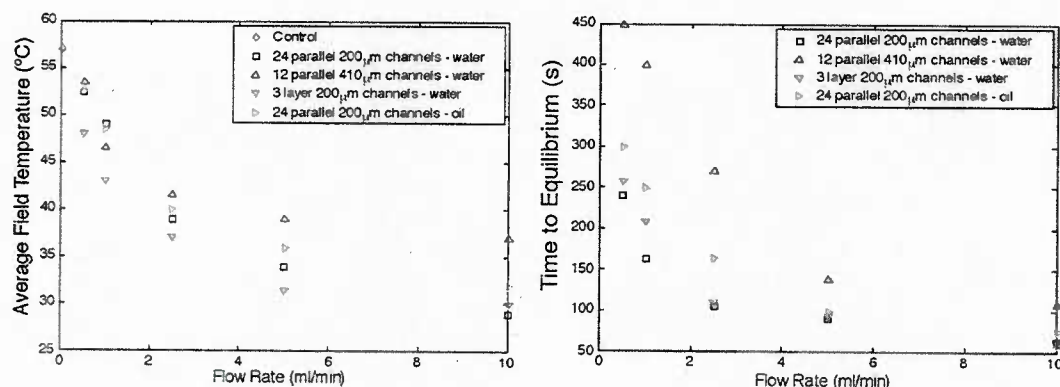*Figure 95. Average field temperature vs. time for water and oil coolant.*

The three layer specimens showed mixed results when compared to the single layer network with the same

Figure 96. Field average temperature and time to steady state.

channel diameter. The transient response of the multiple-layer network was slower than the single layer network taking up to 25% longer to reach equilibrium at low flow rates. However, the multiple layer networks did show more efficient cooling, particularly at lower flow rates, with up to a 13% lower temperature when compared to the single layer network.

Water was the standard working fluid for these tests, but a military certified MIL-PRF-87252 cooling oil was also compared to results in the 24 parallel, 200 μm channel diameter specimen. The cooling trends were qualitatively similar between these two fluids, but water always exhibited a faster cooling response and also a lower steady state temperature at higher flow rates. However, at flow rates of 2.5 ml/min and lower, the military oil coolant is slower to cool but reaches a steady state temperature that is approximately equal to that of water. The military oil is better suited for real applications with a higher flash point and antioxidant additives properties.

Finally, the flow through the microvascular networks was examined using micro-PIV. Dilute quantities of 20 μm fluorescent particles were injected into the system and visually tracked to determine flow rates in all channels. At higher flow rates all channels are activated

(69)

and have steady flow. However, flow rates below 2.5 ml/min exhibited a sharp decrease in cooling efficiency due to channel blockages preventing access to portions of the network. Incomplete network perfusion was accentuated in 3-D networks and with larger diameter channels.

Autonomic cooling: Our autonomic cooling concept is shown in Figure 97 and consists of a microvascular system incorporating thermally activated internal valves and surface pores, and utilizes convective cooling in microchannels as well as evaporative cooling from surface pores. This system operates in three different stages depending on the localized temperature in an individual "cell" in the network.
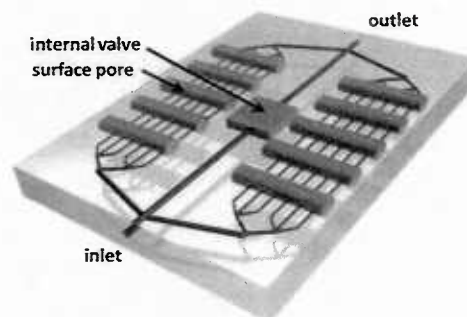
Figure 97. Schematic of one cell in the autonomic cooling concept.

Stage 1 is the low temperature default condition when cooling is not required and low pressure drop is achieved by routing flow through a large diameter central channel. Internal, heat activated valves are spaced along these arteries, and at high local temperature they will activate and block flow in the main artery. This activates the second cooling stage which forces the flow into smaller capillary networks surrounding the valve. The pressure will increase in the network, and the disperse capillary network utilizes the advantages of microvascular cooling to locally cool the immediate "cell" area.

The final stage is activated when stage 3 is activated and the temperature rises even higher. This localized hot spot will activate surface pores which will open to enable capillary fluid flow to the surface and allow evaporative cooling on the surface.

This cellular and staged cooling system is designed to effectively handle local hot spots in the network and maximize efficiency by providing low pressure drop in relatively cool areas and two cooling mechanisms in hot areas. It also has a strong biological inspiration and reacts much in the same way as the human body to heated conditions, and will provide a type of synthetic skin for future high performance cooling applications.

The system design relies on thermally activated internal valves and surface pores, and working prototypes have been fabricated for both types of valves. First, the internal valve must stop artery flow at high temperature and be effectively incorporated into networks fabricated via the direct write assembly process. A simple valve has been developed which utilized a PDMS (Sylgard 184) elastomer block which is incompressible ($\nu = 0.5$) and possesses a very high coefficient off thermal expansion (CTE) ($\alpha = 325$ $\mu\varepsilon/°C$) compared to the bulk matrix material (Epon 282 / Epikure 3300, $\alpha = 55$ $\mu\varepsilon/°C$). The elastomer block is 10 mm long, 20 mm wide, and 1.75 mm tall and has a groove down the center ($D_h = 550$ μm) which is placed in direct contact with the artery channel. The valve utilizes the CTE mismatch such that as the system heats up, the elastomer block expands more than the surrounding matrix material, but is also physically constrained by the surrounding matrix. Thus as the elastomer block expands, it fills the gap forming the artery channel and obstructs the flow. This then forces the flow into the capillary networks for stage 2 cooling.

μVAC a new paradigm in materials design

Figure 98 shows the prototype internal valve in a microcascular network following Murray's Law with a main artery diameter of 510 μm, secondary branches which are 400 μm in diameter, and third level channels that are 330 μm in diameter. Figure 98 also shows valve activation and the transition from stage 1 to stage 2 flow which is triggered at a temperature of 120 °C. Note that this type of valve does not operate in a binary on/off fashion, but rather responds linearly to increased temperature and gradually routes more flow to the side networks.

(a)   (b)   (c)
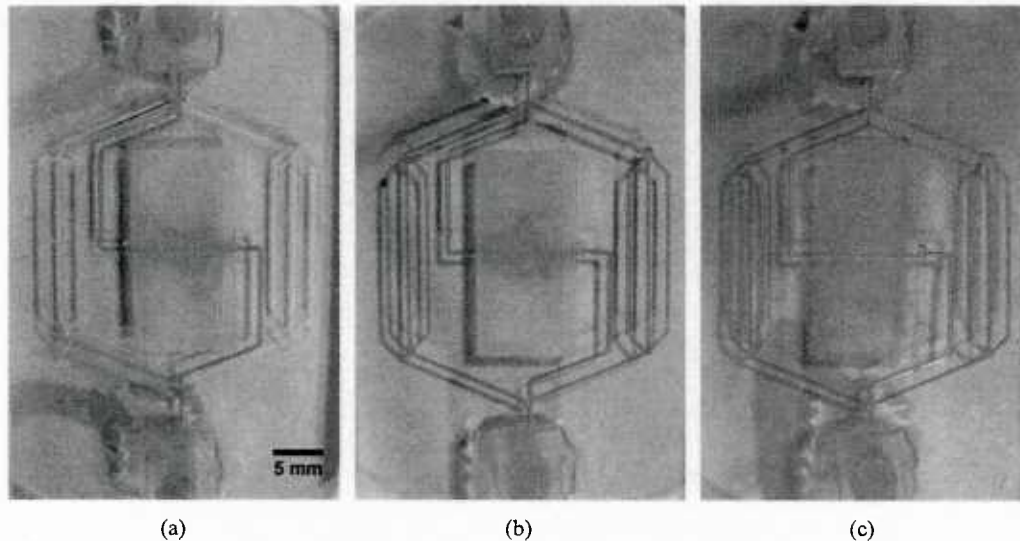
Figure 98. Elastomer valve function. (a) room temperature at flow rates below 5 ml/min. (b) room temperature at flow rates above 5 ml/min. (c) high temperature (120 °C) with flow rates below 10 ml/min.

The second type of valve is a thermally activated surface pore which again utilizes differences in thermal expansion. In this case, the pore plug consists of a low CTE circular rod which lies across, and is partially embedded into, the top portion of the microvascular network. The specimen is then sanded and polished down to reveal the top portion of the valve rod (Figure 99b), and the interface between the matrix and the rod become the surface pores. The activation mechanism is that the matrix compresses the rod at low temperature thus sealing the pore, but at high temperature, the matrix expands more than the valve plug due to its higher CTE, and this creates a small, capillary sized gap between the matrix and valve. The gap is approximately 1-3 μm wide at elevated temperature, depending on the valve material and diameter, and is ideal for allowing capillary flow to the surface for evaporative cooling.

Prototype surface pores were created in a microvascular network (shown in Figure 99) consisting of 24 parallel channels, 250 μm in diameter spaced 800 μm center to center. Three types of valve material were examined in varying diameters: 0.9 mm diameter graphite rods ($\alpha = 50$ με/°C), 1.6 mm diameter brass rods ($\alpha = 19$ με/°C) and 1 and 2 mm diameter fused quarts rods ($\alpha = 0.55$ με/°C). The valve rods were rested on 170 μm vertical spacers such that they were embedded exactly 80 μm down into the channel. This provided uniform activation across the specimen and insured minimal increase in pressure drop due to the valve rods.

The prototypes were tested under low and high temperature conditions and were found to close securely at low temperatures and effectively open and allow flow to the surface at

approximately 130 °C, regardless of the valve material used. The low pressure flow conditions allow capillary action alone to wick coolant to the surface. To better visualize the pore opening, high pressure conditions were also examined where the flow output was blocked, and larger, visible droplets formed on the surface. Typical results are shown in Figure 99c,d.

Finally, the surface pore was modeled analytically including temperature dependent material properties in the matrix. This allowed a detailed analysis of the effect of changing the valve material and dimensions. This model reveals that the activation temperature is dependent on the glass transition temperature (and thus final cure temperature) of the matrix alone and is not affected by the valve material or the valve diameter. The material and diameter do affect the rate of opening, however, with lower CTE materials and larger diameter valves opening at a faster rate and resulting in larger pore openings.

(a)

(b)

(c)

(d)
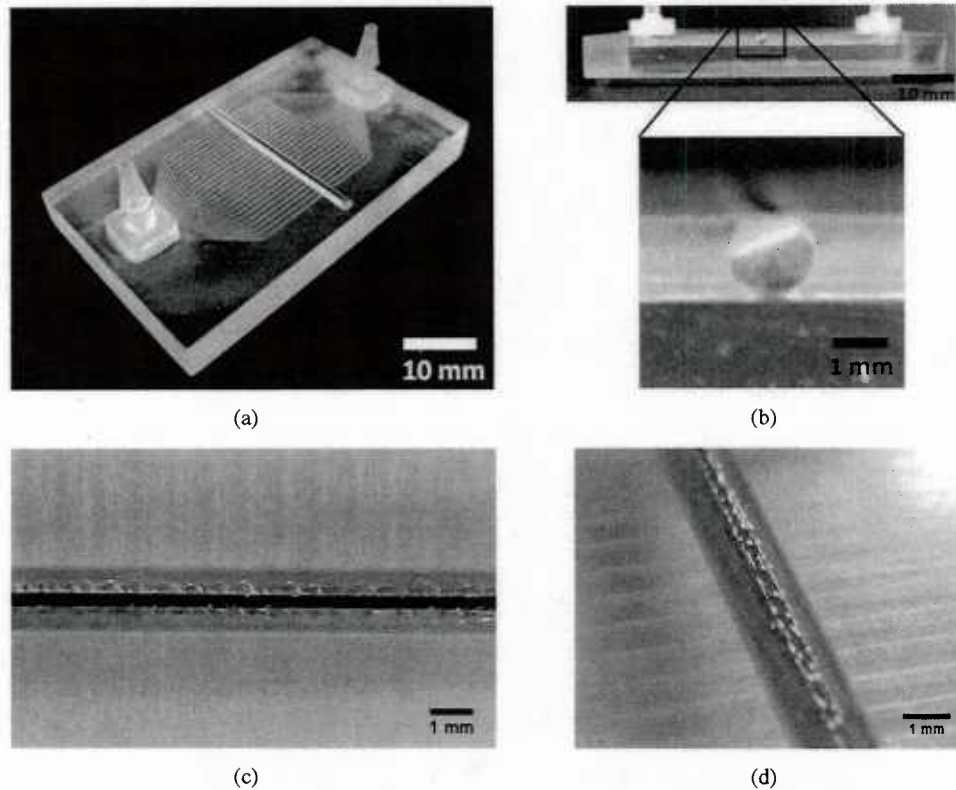
Figure 99. Prototype surface pores. (a) overview of specimen with pores, (b) side of specimen showing the pore rod intersection the specimen surface, (c-d) water droplets forming on surface under high temperature and high pressure flow.

While the prototype internal valves showed some promise, they were rather large and could not reliably stop high pressure flow. Improving the performance required either increasing the CTE of the elastomer or increasing the constraint of the matrix. The elastomer CTE was initially increased by using a silicone gel with a CTE of 720 $\mu\varepsilon$/C and by incorporating paraffin microspheres into the valve material, but these methods failed to
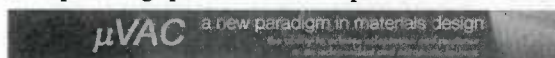
improve increase performance. Ultimately, the limitation of this design was relying on epoxy for constraint due to its viscoelastic properties and the high temperature cure cycle.

The internal valve was significantly refined and improved by increasing the constraint on the elastomer material. Instead of relying on the epoxy matrix for constraint, the elastomer


(a)   *(b)*   *(c)*
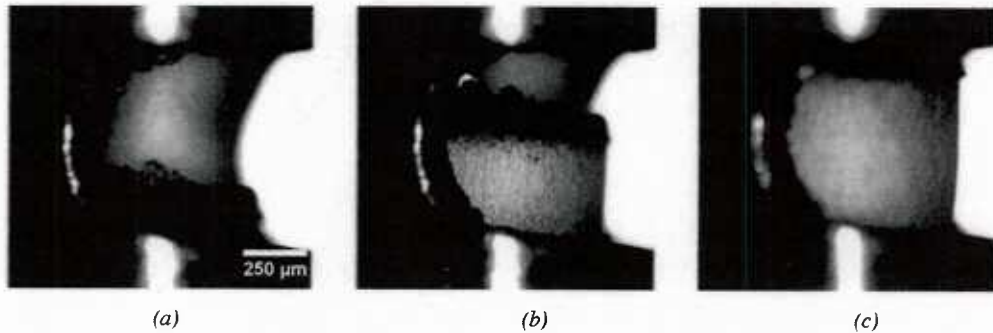
Figure 100. The stages of closing the valve exit for the steel and Sylgard 184 (PDMS) valve. a) The valve exit is fully open at room temperature. b) The valve exit is partially closed by PDMS at 70 °C. c) The valve exit is completely closed off by the PDMS plug at 85 °C.

was formed inside a stainless steel tube allowing the valve to be fabricated at room temperature and significantly increasing the constraint. The new valve dimensions are 20 mm long cylinder which is 1.2 mm in diameter which is a 17 fold reduction in volume compared to the initial prototype.

The new steel and elastomer valve proved to have much more reliable performance and actuates at lower temperatures. The valves have been tested independently to show 20+ complete closing and opening cycles and the activation temperature has been lowered from

(a)   (b)   (c)
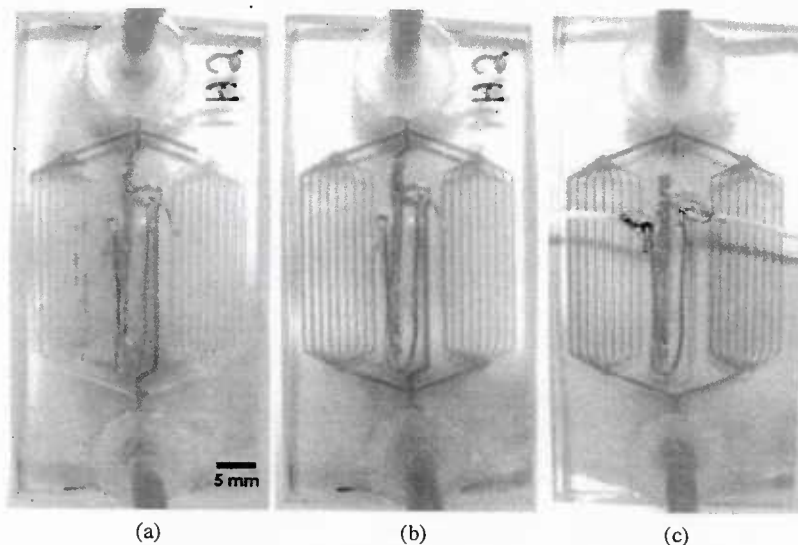
Figure 101. Internal steel and PDMS valve embedded in vascular network. a) Arterial flow at room temperature and flow rate of ≤ 1 ml/min. b) Full network filled at room temperature and flow rate of ≥ 20 ml/min. c) Main artery completely closed at 85 °C and flow rates up to 80 ml/min.

(73)
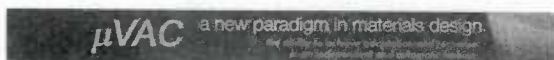
120 °C down to 70-90 °C depending on the valve length and the type of elastomer used. The current design is 20 mm long, uses Sylgard 184 (PDMS) as the elastomer, and activates at approximately 80-90 °C. Figure 100 shows the stages of ativation of this new valve. The image shows the valve outlet which is completely open in Figure 100a and completely closed in Figure 100c.

In addition, the new internal valve configuration has shown repeatable, high pressure activation inside vascular specimens. Figure 101 highlights the updated network geometry configuration with the new steel/PDMS internal valve embedded. (Note: A nickel chromium resistive heating wire was embedded in the sample to aid in preliminary testing.) The network geometry has been optimized to take advantage of the substantially smaller footprint of the new valve design and to increase the number of "capillary channels" from 6 to 18. The three stages of system flow are shown in Figure 101. Figure 101a shows the low temperature (room temperature) and low flow rate (1 ml/min) condition where the flow prefers the large diameter center channel with low pressure drop. Figure 101b is low temperature, high flow rate (10+ ml/min) where the central artery is the preferred flow path, but the coolant also fills the capillary channels. Finally, Figure 101c shows the high temperature (85 °C) and high flow rate (up to 80 ml/min) condition where the valve is activated and completely closes off the central artery. This last configuration slightly increases the system pressure drop, but also invokes convective microvascular cooling from the 18 capillary channels which is much more effective for cooling and heat transferm (Tuckerman et al. 1981).

The surface pores have also been studied and refined. The previous surface pores were thermally activated based on a CTE mismatch principle using 1.6 mm diameter brass rods embedded in the vascular specimen. While these valves showed reliable and repeatable activation at approximately 110 °C, the geometrical configuration is cumbersome and does not

(a)   (b)   (c)

(d)   (e)   (f)
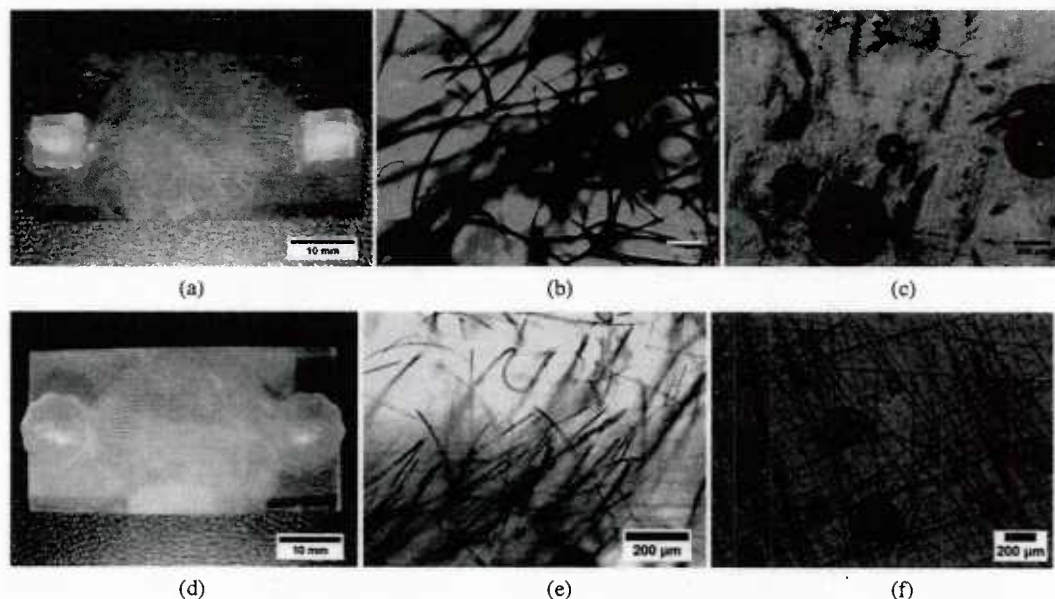
Figure 102. Samples and pores created via sacrificial fibers. a) Sample fabricated with PLA fibers. d) Sample fabricated with melt-spun sugar fibers. b and e) Micrograph showing internal pore channels. c and f) Micrograph showing pores and water droplets on surface.

easily scale to larger size specimens. Thus, several new concepts have been developed and tested to create surface pores using methods that are scalable to larger specimen sizes. These methods include using sacrificial fiber mats or using a 2-D, woven wire mesh in place of individual rods.

First, random mats of sacrificial fibers were used to create pores from the internal vascular network to the surface. The two types of sacrificial fibers included 20 μm diameter poly(lactic acid) (PLA) fibers and melt-spun sugar fibers (Bellan et al. 2009) with an average diameter of 6 μm and a range of 2 to 18 μm. The fibers were formed in a random mat arrangement and then partially embedded into the fugitive wax ink during the fabrication process. After the specimen was fully cured and the wax ink was removed, the sacrificial fibers were removed to create channels to the surface. The PLA fibers were removed by heating the sample to 210 °C in a vacuum oven for approximately 24 hours, while the melt-spun sugar fibers were removed by sonicating the samples in a 50 °C warm water bath for 18 hours. The end result is a fine network of 6 or 20 mm diameter channels linking the internal microchannels to pores in the surface. The samples and pores are shown in Figure 102.

The surface pores created with sacrificial fibers are currently not active, however testing does show a slight increase in pore activity at elevated temperatures as shown in Figure 103. These pores are easily fabricated, scalable, and provide a basic functionality if incorporated into the network architecture described above, but further work is needed to turn these types of pores into viable autonomic valves.
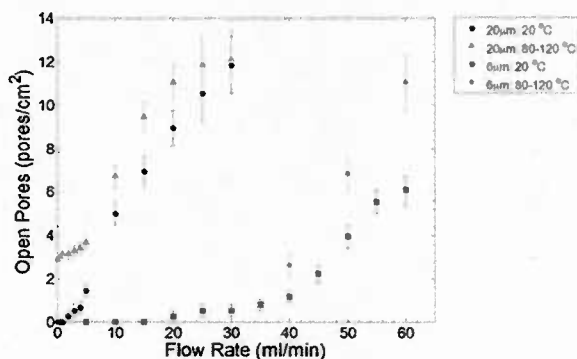

Figure 103. Temperature and flow rate effect on pores created via sacrificial fibers. Note: "Open Pores" are counted by observing droplets formed on 20x20 mm surface during 2 min period.

The final method of fabricating thermally activated surface pores operates via the same CTE mismatch principle as the initial valves, but uses a 2-D mesh of woven copper wire instead of individually placed metallic rods. The copper mesh is 1 mm thick and consists of 432 μm diameter wires spaced at 18 wires per inch. This has the advantage of being easily scalable due to the surface pores being one additional layer in the fabrication process, and also may have additional utility in the aerospace area as a lightning strike protection system. The wire mesh is embedded into the fugitive wax ink during the fabrication process, and after the sample is fully cured, the top of the sample is sanded down to reveal the top of the copper mesh and create the surface pores. Initial samples have been created and the release agent for the copper mesh and vertical spacing in the microvascular channels are being examined. Figure 104 shows the copper mesh and preliminary samples created using this technique.
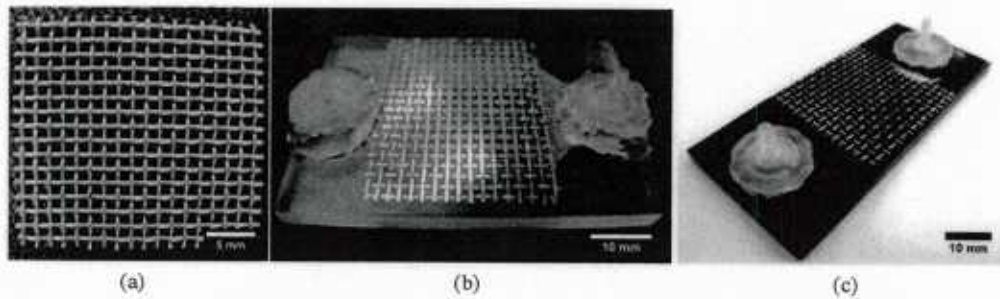
Figure 104. Images of the surface pores created via embedded copper mesh. a) Copper mesh. b) Copper mesh embedded into microvascular sample. c) Copper mesh embedded in black epoxy sample to highlight surface pore areas.

3. References

Aragón AM, Duarte CA and Geubelle PH. **2010**. Generalized finite element enrichment functions for discontinuous gradient fields. *International Journal for Numerical Methods in Engineering* 82(2): 242-268.

Aragón AM, Geubelle PH, White SR. **2011**. Multi-physics optimization of microvascular materials. *International Journal of Heat and Mass Transfer*. Submitted.

Atencia J, Beebe DJ. **2006**. Steady flow generation in microcirculatory systems. *Lab Chip* 6: 567-574.

Beebe DJ, Moore J, Bauer J, Qing Y, Liu R, Devadoss C, Jo B. **2000**. Functional hydrogel structures for autonomous flow control inside microfluidic channels. *Nature* 404: 588-590.

Bellan LM, Singh SP, Henderson PW, Porri TJ, Craighead HG and Spector JA. **2009**. Fabrication of an artificial 3-dimensional vascular network using sacrificial sugar structures. *Soft Matter* 5(7): 1354-1357.

Berfield TA, Patel JK, Shimmin RG, Braun PV, Lambros J and Sottos NR. **2006**. Fluorescent image correlation for nanoscale deformation measurements, *Small* 2(5): 631-635.

Berfield TA, Patel JK, Shimmin RG, Braun PV, Lambros J and Sottos NR. **2007**. Micro- and nanoscale deformation measurement of surface and internal planes via digital Image correlation, *Experimental Mechanics* 47:51-62.

Bielawski CW, Grubbs RH, Angew. **2000**. *Chem. Int. Ed.* 39: 2903-2906.

Bieniek M, Bujok R, Cabaj M, Lugan N, Lavigne G, Arit D, Grela K. **2006**. *J. Am. Chem. Soc.* 128: 13652-13653.

Bogdanovich A, Bradford P, Mungalov D, Fang S, Zhang M, Bousse L RH, Cohen C, Nikiforov T, Chow A, Kopf-Sill A, Dubrow R, Parce J. **2000**. Electrokinetically Controlled Microfluidic Analysis Systems. *Annu. Rev. Biophys. Biomol. Struct.* 29:155-181.

Bogdanovich A. Bradford P, Mungalov D, Fang S, Zhang M, Baughman RH and Hudson S. **2007**. Fabrication and mechanical characterization of carbon nanotube yarns, 3-D braids, and their composites. *SAMPE Journal* 43: 6-19.

Bogdanovich A and Mohamed MH. **2009**. Three-Dimensional Reinforcements for Composites. *Sampe Journal* 45(6): 8-28.

Brown EN, White SR, Sottos NR. **2002**. *Exp. Mech.* 42: 372-379.

Brown EN, Kessler MR, Sottos NR, White SR. **2003**. *J. Microencapsulation*, 20: 719-730.

Brown EN, White SR, Sottos NR. **2005a**. *Comp. Sci. Tech.* 65: 2466-2473.

Brown EN, White SR, Sottos NR. **2005b**. *Compos. Sci. Tech.* 65: 2474-2480.

Brown EN, White SR, Sottos NR. **2006.** *J. Mater. Chem.* 41: 6266-6273.

Caruso MM, Delafuente DA, Ho V, Sottos NR, Moore JS, White SR. **2007.** *Macromolecules* 40: 8830.

Caruso MM, Blaiszik BJ, White SR, Sottos NR, Moore JS. **2008.** *Adv. Funct. Mater.* 18:1898.

Caruso MM, Davis DA, Shen Q, Odom SA, Sottos NR, White SR and Moore JS. **2009.** Mechanically-induced chemical changes in polymeric materials. *Chemical Reviews* 109(11): 5755-5798.

Cho SH, Andersson HM, White SR, Sottos NR, Braun PV. **2006.** *Adv. Mater.* 18:997.

Deb K, Agrawal S, Pratap A, Meyarivan T. **2002.** A fast and elitist multi- objective genetic algorithm: NSGA-II, IEEE Transact. *Evol. Comput.* 6(2): 181–197.

Fan Y, Nishida H, Mori T, Shirai Y and Endo T. **2004.** Thermal degradation of poly(L-lactide): Effect of alkali earth metal oxides for selective L,L-lactide formation. *Polymer* 45(4):1197-1205.

Garber SB, Kingsbury JS, Gray BL, Hoveyda AH. **2000.** *J. Am. Chem. Soc.* 122: 8168-8179.

Glasgow I and Aubry N. **2003.** Enhancement of microfluidic mixing using time pulsing. *Lab on a Chip* (3): 114-120.

Hansen CJ, Wu W, Toohey KS, Sottos NR, White SR and Lewis JA. **2009.** Self-healing materials with interpenetrating microvascular networks. *Adv. Mater.* 21(41): 4143-4147.

Harrison DJ, Fluri K, Seiler K, Fan Z, Effenhauser CS, Manz A. **1993.** Micromachining a miniaturized capillary electrophoresis-based chemical analysis system on a chip. *Science* 261: 895-897.

Huang J, Stevens ED, Nolan SP, Peterson JL. **1999.** *J. Am. Chem. Soc.* 121: 2674-2678.

Jones AS, Rule JD, Moore JS, Sottos NR, White SR. **2007.** *J. R. Soc. Interface* 4(13): 395-403.

Kessler MR, Sottos NR, White SR. **2003.** Composites: Part A 34: 743-753.

Kirkby EL, Rule JD, Michaud VJ, Sottos NR, White SR and Manson J-AE. **2008.** Embedded shape-memory alloy wires for improved performance of self-healing polymers. *Adv. Funct. Mater.* 18(15): 2253-60.

Li G, Feng Y, Gao P, Li X. **2008.** *Polym. Bull.* 60: 725.

Lvov Y, Price R, Gaber B and Ichinose I. **2002.** Thin film nanofabrication via layer-by-layer adsorption of tubule halloysite, spherical silica, proteins and polycations, *Colloids and Surfaces A (Physicochemical and Engineering Aspects)* 198-200, 375-382.

Mao H, Yang T and Cremer PS. **2002.** A microfluidic device with a linear temperature gradient for parallel and combinatorial measurements. *J. Am. Chem. Soc.* 124: 4432-4435.

μVAC a new paradigm in materials design

Mauldin TC, Rule JD, Sottos NR, White SR, Moore JS. **2007.** Self-healing kinetics and the stereoisomers of dicyclopentadiene. *J. Royal Society: Interface*, 4(13): 389-393.

Natrajan VK and Christensen KT. **2008a.** A Two-color fluorescent thermometry technique for microfluidic devices. *46th AIAA Aerospace Sciences Meeting*, AIAA Paper 2008-0689.

Natrajan VK and Christensen KT. **2008b.** Development of fluorescent thermometry methods for microfluidic systems. *14th International Symposium on Applications of Laser Techniques to Fluid Mechanics*, Lisbon, Portugal, Paper No. 1284.

Natrajan VK and Christensen KT. **2009.** Two-color laser-induced fluorescent thermometry for microfluidic systems. *Measurement Science & Technology* 20(1):11.

Pathak T and Waldmann H. **1998.** Enzymes and protecting group chemistry. *Current Opinion in Chemical Biology* 2(1): 112-120.

Plaisted T, Amirkhizi A, Nemat-Nasser S. **2006.** Compression-induced axial crack propagation in DCDC polymer samples: experiments and modeling. *International Journal of Fracture* 141: 447-457.

Quirk RA, Davies MC, Tendler SJB and Shakesheff KM. **2000.** Surface engineering of poly(lactic acid) by entrapment of modifying species. *Macromolecules* 33(2): 258-260.

Roller MB. **1975.** Characterization of the time-temperature-viscosity behavior of curing B-staged epoxy resin. *Polym. Eng. Sci.* 15(6): 406-414.

Rule JD, Brown EN, Sottos NR, White SR, Moore JS. **2005.** *Adv. Mater.* 17: 205-208.

Rule JD, Sottos NR, White SR. **2007.** *Polymer* 48: 3520-3529.

Ryu KS, Shaikh K, Goluch E, Fan Z, Liu C. **2004.** Micro magnetic stir-bar mixer integrated with parylene microfluidic channels. *Lab Chip* 4:608-613.

Sack L, Melcher PJ, Zwieniecki MA, Holbrook NM. **2002.** The hydraulic conductance of the angiosperm leaf lamina: a comparison of three measurement methods. *Journal of Experimental Botany* 53(378): 2177-2184.

Sagi A, Weinstain R, Karton N and Shabat D. **2008.** Self-immolative polymers. *J. Am. Chem. Soc.* 130(16): 5434-5435.

Sakakibara J and Adrian RJ. **1999.** Whole field measurements of temperature in water using two-color laser induced fluorescence, *Experiments in Fluids* 26: 7-15.

Skoog DA, Holler FJ, Nieman TA. **1998.** *Principles of Intstrumental Analysis, Philadelphia: Saunders.*

Scholl M, Ding S, Lee CW, Grubbs RH. **1999.** Org. Lett. 1: 953-956.

Silvester D, Elman H, Wathen A. **2005.** Finite elements and fast iterative solvers with applications in incompressible fluid dynamics, Oxford Science Publications.

Singh D, Kuckling D, Choudhary V, Adler HJ, Koul V. **2006.** Synthesis and characterization of poly(N-isopropylacrylamide) films by photopolymerization. *Polym. Adv. Technol.* 17:186-192.

Smirnova NN, Lebedev BV, Kiparisova EG, Makovetskii KL, Ostrovskaya IY. **1997.** Thermodynamics of endo- and exo-dicyclopentadienes, their metathesis and addition polymerizations, and the resulting polymers. *Vysokomolekulyarnye Soedineniya Seriya A & Seriya B* 39(8): 1323-1331.

Srinivas N and Deb K. **1995.** Multi-objective function optimization using nondominated sorting genetic algorithms. *Evolutionary Computation Journal* 2(3): 221–248.

Sun Y and Beckermann C. **2007.** Sharp interface tracking using the phase-field equation. *Journal of Computational Physics* 220:626–653.

Szabó B and Babuska I. **1991.** *Finite element analysis*. Wiley-Interscience.

Szabó B and Babuska I. **2011.** *Introduction to Finite Element Analysis: Formulation, Verification and Validation.* John Wiley & Sons, Ltd.

Tamuzs V, Tarasovs S, Vilks U. **2003.** Delamination properties of translaminar-reinforced composites. *Composites Science and Technology* 63:1423-1431.

Therriault D, White SR and Lewis JA. **2003.** Chaotic mixing in three-dimensional microvascular networks fabricated by direct-write assembly. *Nat. Mater.* 2(4): 265-271.

Toohey K, White SR and Sottos NR. **2005.** Self-Healing Polymer Coatings. *Proceedings of the SEM Annual Meeting on Experimental and Applied Mechanics*, Portland OR, CD-ROM.

Toohey KS, Sottos NR, Lewis JA, Moore JS, White SR. **2007.** Self-healing materials with microvascular networks, *Nat. Mater.* 6:581-585.

Toohey KS, Hansen C, Lewis JA, White SR and Sottos NR. **2009a,** Delivery of two-part self-healing chemistry via microvascular networks. *Adv. Funct. Mater.* 19: 1399-1405.

Toohey KS, Sottos NR and White SR. **2009b.** Characterization of Microvascular-Based Self-healing Coatings. *Experimental Mechanics* 49: 707-717.

Tuckerman DB and Pease RFW. **1981.** High-performance heat sinking for VLSI. *IEEE Electron Device Letters* ED-2(5): 126-9.

Wakamatsu H, Blechert S, **2002.** Angew. *Chem. Int. Ed.* 41: 794-796.

White SR, Sottos NR, Geubelle PH, Moore JS, Kessler MR, Sriram SR, Brown EN and Viswanathan S. **2001,** Autonomic healing of polymer composites, *Nature* 409: 794-797.

Williams KA, Boydston AJ and Bielawski CW. **2007.** Towards electrically conductive, self-healing materials. *Journal of the Royal Society Interface* 4(13): 359-62.

Wuts PGM and Greene TW. **2006.** *Greene's Protective Groups in Organic Synthesis.* Hoboken, NJ, USA: John Wiley & Sons, Inc., 10.

Yang J, Keller MW, Moore JS, White SR and Sottos NR. **2008**. Microencapsulation of isocyanates for self-healing polymers. *Macromolecules* 41(24): 9650-9655.

Zwieniecki MA, Melcher PJ, Boyce CK, Sack L, Holbrook NM. **2002.** Hydraulic architecture of leaf venation in Laurus nobilis L. *Plant, Cell and Environment* 25: 1445-1450.